WARSAW UNIVERSITY OF TECHNOLOGY

DYSCYPLINE OF SCIENCE - MATERIALS ENGINEERING
FIELD OF SCIENCE - ENGINEERING AND TECHNOLOGY

Ph.D. Thesis

Łukasz Kukołowicz, M.Sc.

Degradation Mechanism of High Strength Tensile Wire Induced by Stress Corrosion in CO_2-H_2S Environment

Supervisor
Professor Dariusz Oleszak, Ph. D., D.Sc.

WARSAW 2023

Projekt współfinansowany w ramach programu Ministra Nauki i Szkolnictwa
Wyższego pt. „Doktorat wdrożeniowy”,
umowa nr 0050/DW/2018/02

I would like to thank my manager Garry Kendal, for support necessary to finish this research, and my supervisor Professor Dariusz Oleszak, for encouragement.

Abstract

A 0.65-0.070 % C pearlitic-ferritc cold rolled high strength wire is used in construction of API 17J unbonded flexible pipes. The wire is subject to an accelerated corrosion testing to prove fit for purpose resistance to degradation by CO_2 and H_2S. A high percentage of material batches failing in testing results in an estimated cost to Baker Hughes company of few $ million a year.

Metallographic analysis allowed for a formulation of a research hypothesis that the microstructural features associated with failure can be controlled by the wire chemical composition. The statistical analysis was based on 500 unique steel batches tested in 1164 tests. The assumptions made to reduce the dimensionality of the problem were found valid only for steel manufactured in a continuous casting process.

The wire performance was evaluated as normalized failure probability. It was found that each failure mechanism involves complex interaction of at least five elements C, Mn, Si, S, P. Models of three failure mechanisms were proposed. The hydrogen induced cracking is initiated from inclusions located at ferrite grain boundaries. It is controlled among others by inclusions size, ferrite solution strengthening, microstructural damage accumulation during cold rolling and grain boundary embrittlement by P. The sulphide stress cracking of parent wire initiates at the bottom of pits. The factors controlling the initiation and propagation are among others: damage accumulation within ferrite grains subsurface, ferrite morphology and segregation of P to grain boundaries. The weld sulphide stress cracking is controlled by formation of pits at sulphide type inclusions extruded to the steel surface during upset welding. The controlling factor is the distribution of inclusions within the wire. Non-metallic inclusions constitute a capable hydrogen trap, and their high density decreases the occurrence of sulphide stress cracking of both parent and welded wire.

It was found that fine tuning of chemical composition can mitigate all three failure mechanisms simultaneously. Failure rate in fit for purpose testing can be at least order of magnitude lower at no additional cost.

Keywords: sulphide stress cracking, hydrogen induced cracking, CO_2-H_2S degradation, CO_2-H_2S corrosion, cold rolled wire, unbonded flexible pipe.

Streszczenie

W konstrukcji rur elastycznych zgodnych ze standardem API 17J używany jest zimnowalcowany drut o wysokiej wytrzymałości produkowany ze stali o zawartości 0,65 % - 0,70 % C o strukturze perlityczno-ferrytycznej. Drut poddawany jest przyśpieszonym testom korozyjnym mającym potwierdzić jego odporność na degradację w środowisku zawierającym CO_2 ze śladowymi ilościami H_2S. Skład gazu podczas testu jest zgodny z przewidywanym dla danego projektu. Kilkanaście procent serii produkcyjnych drutu nie przechodzi testów, co powoduje straty rzędu kilku milionów dolarów rocznie.

Analiza zniszczeń drutów ujawniła cechy związane z pęknięciami i pozwoliła na postawienie hipotezy badawczej, że odporność na degradację jest funkcją składu chemicznego. Analiza statystyczna została oparta na 500 seriach drutów, na których wykonano łącznie 1164 testów korozyjnych. Założenia, które pozwoliły na redukcję wymiarowości modelu, okazały się prawidłowe tylko dla drutów produkowanych ze stali z odlewania ciągłego.

Odporność na degradację szacowano jako znormalizowane prawdopodobieństwo pękania. Wykazano, że na każdy mechanizm degradacji wpływa skomplikowana interakcja co najmniej pięciu pierwiastków C, Mn, Si, S i P. Zaproponowano modele trzech mechanizmów degradacji. Pękanie wodorowe inicjuje na wtrąceniach niemetalicznych na granicach ferrytu. Czynniki kontrolujące ten mechanizm to między innymi rozmiar wtrąceń, umocnienie roztworowe ferrytu, akumulacja defektów mikrostruktury podczas odkształcenia i segregacja manganu. Korozja naprężeniowa inicjuje w miejscach lokalizacji korozji pod produktami korozji. Czynnikami kontrolującymi inicjację i propagację są podpowierzchniowa akumulacja defektów mikrostruktury podczas odkształcenia - głównie w ziarnach ferrytu, morfologia ferrytu i segregacja P do granic ziaren. Korozja naprężeniowa spoin inicjuje od wżerów związanych ze wtrąceniami siarczków wyniesionymi na powierzchnię drutu w procesie zgrzewania doczołowego. Dystrybucja wtrąceń kontroluje występowanie tego mechanizmu zniszczenia. Wtrącenia niemetaliczne stanowią pułapkę dla wodoru. Wykazano, że duża gęstość wtrąceń zmniejsza występowanie korozji naprężeniowej drutu rodzimego i spoin.

Wykazano, że zmiany składu chemicznego mogą ograniczyć występowanie wszystkich trzech mechanizmów zniszczenia co najmniej o rząd wielkości bez zmiany ceny.

słowa kluczowe: korozja naprężeniowa, pękanie wodorowe, degradacja w CO_2-H_2S , korozja w CO_2-H_2S, drut zimnowalcowany, rury elastyczne.

Contents

Abbreviation	Definition
AIDE	Absorption-Induced De-cohesion Emission
$\mathrm{N_H}^{\mathrm{I,P}}$	Actual hydrogen amount trapped to inclusions
C_H	Amount of hydrogen trapped within the material
BCC	Body Centered Cubic crystalline structure
ANP	Brazilian National Petroleum Agency
CG HAZ	Coarse Grain Heat Affected Zone
CODAM	Corrosion and Damage Database for Flexible Pipes
N_C and C_K	Critical Hydrogen Concentration at which cracks are induced or assisted
EAC	Environmentally Assisted Cracking
FCC	Face Centered Cubic crystalline structure
FG HAZ	Fine Grain Heat Affected Zone
HDPE	High Density Polyethylene
HLP	High strength Line Pipe committee test solution
HE	Hydrogen Embrittlement
HIC	Hydrogen Induced Cracking
HEDE	Hydrogen-Enhanced De-cohesion
HELP	Hydrogen-Enhanced Localized Plasticity
MLE	Maximum Likelihood Estimation
NFP	Normalized Failure Probability
$\widehat{NFP}$	Estimator of NFP
PSA	Norwegian Petroleum Safety Authority
PA	Polyamide
PVDF	Polyvinylidene fluoride
PWHT	Post Weld Heat Treatment
SCR	Steel Catenary Riser
SSC	Sulphide Stress Cracking
$\mathrm{K_{ISSC}}$	Threshold Stress Intensity Factor for SSC
TTR	Top Tension Riser
UTS	Ultimate Tensile Strength
UKOOA	United Kingdom Offshore Operators Association
YS	Yield Stress

1 Introduction

1.1 Offshore Oil and Gas Market Overview

The global Oil and Gas market was worth $ 6.1 billion in 2021 with the crude oil production of 77 million barrels a day. The natural gas production was 3,929 km^3 in 2019. In the long term, the Oil and Gas market will be affected by the energy transition. Renewable energy and green hydrogen are more likely to substitute natural gas than oil. It is estimated that in its most ambitious 2050 energy transition scenario [1] the oil demand is likely to only half.

The offshore production of oil accounts for nearly 30 % of the world oil production. It can be generalized that the offshore production sites are more expensive to build than onshore, but operate at a lower cost than onshore operations. Producing offshore projects average a break-even price of $ 18.10 per barrel of oil equivalent, compared with $ 28.20 per barrel for onshore [2]. The carbon footprint of oil from offshore projects is lower than from onshore projects. Massive scale allows for application of the new energy efficient technologies. On the other hand, the offshore projects have to mitigate huge environmental risks. Oil fields can affect marine ecosystems. The explosion of the drilling rig Deepwater Horizon and the subsequent oil spill of an estimated 3.19 million barrels was the largest environmental catastrophe in the United States. The current capacities of the offshore drilling industry are water depths of more than 3 km under severe environmental conditions. Ultra-deep wells costing more than $ 50 million are common. High cost and the environment protection are the main industry challenges.

1.2 The Unbonded Flexible Pipe

1.2.1 History of the Market

In the 1960s French Institut Français du Pètrole began to develop an unbonded flexible pipe. That effort resulted in a patent in 1972 and a commercialization by a consortium named Coflexip. Coflexip produced pipes from 2.5-inch to 10-inch with pressure ratings from 2000 to 10,000 psi (140 - 690 bar). The primary applications were in Brazil and the North Sea. The loading hose manufacturers, like Dunlop, Pirelli, Gates, PagoFlex, Manulli, Taurus tried to compete with Coflexip. Eventually, it became apparent that the elastomers in bonded pipe were not sufficiently robust against blistering in high pressure gas applications. In 1983, Wellstream was established as a company and opened their first factory in the Panama City, Florida. Followed by a factory in the UK in 1996. By then, Coflexip had additional factories in Australia and Brazil. In 1996 NKT, a Danish submarine cable manufacturer, modified their cable factory in Denmark to produce flexible pipes [3,4]. In 2007, Wellstream opened a factory in Brazil after closing their US plant. Wellstream was acquired by General Electric in 2011. The part of the business servicing Oil & Gas was merged with Baker Hughes in 2017. General Electric shortly after began selling its shares in the company, which completed in 2022

Currently, there are three manufacturers on the flexible pipe market:

- Technip FMC (previously Coflexip) with three factories in Le Trait, France, Vitória, Brazil and Tanjung Langsat, Malaysia,
- Baker Hughes with two factories in Newcastle Upon Tyne, UK and Niterói, Brazil,
- NOV (NKT untill 2012) with two factories in Superporto do Açu, Brazil and Kalundborg, Denmark.

The estimated global manufacturing capacity of all three suppliers is no larger than 2000 km of normalized 8-inch diameter flexible pipe.

1.2.2 Development of Standards

API Recommended Practice 17B [5] for flexible pipe was issued in 1987. The API 17J [6] 1$^{\text{st}}$ Edition was issued in 1996. In 2013 API 17L1 [7] and API RP 17L2 [8] were issued for Flexible Pipe Ancillary Equipment. The current working standards are API Spec 17J 4th Edition and API RP 17B 5th Edition. The next revision of API 17J standard is scheduled to November 2023.

1.2.3 Serviceable Market Segment

Flexible pipes compete with a more traditional steel tube products like Steel Catenary Risers (SCR) or Top Tension Risers (TTR). There are multiple design considerations which need to be accounted for in the riser system design. In some cases, a flexible pipe is a cost-effective solution. In general, flexible pipes are faster to install, can simplify the system design eliminating equipment like production riser tensioners and are more resistant to fatigue. Corrosion resistant alloys used in the flexible pipe construction simplify the corrosion protection design. A typical flexible pipe is designed for 25 years of operation. Globally, in terms of the riser length, flexible risers make up about 60 - 80 % of installed risers [9]. Brazil is the largest market region for flexibles as it is uncommon to use manifolds there. About 40-50 % of the global flexible pipe production is used in Brazil. The global serviceable market for the flexible pipes was about $ 942 million in 2021.

1.3 Flexible Pipe Construction

The unbonded flexible pipe has a multilayered structure. A typical cross-section shown in Fig. 1.1.

Figure 1.1: Cross-section revealing layers of a typical flexible pipe.

Carcass

Production of a typical pipe begins with a stainless-steel strip formed into an interlocking profile shown in Fig. 1.2. This layer is called a carcass. Its function is to prevent a barrier collapse. The carcass is in direct contact with the bore fluid. A typical carcass strip thickness is between 0.6 mm and 2.0 mm. Steel grade is selected based on the bore fluid corrosiveness. As an example, 316 stainless, lean duplex, 2205 duplex, superduplex or 6-Mo superaustenitic steels have been used.

Barrier

The barrier is the primary pressure retaining component. It is manufactured by extrusion. Typical polymers used are High Density Polyethylene (HDPE), Polyamide

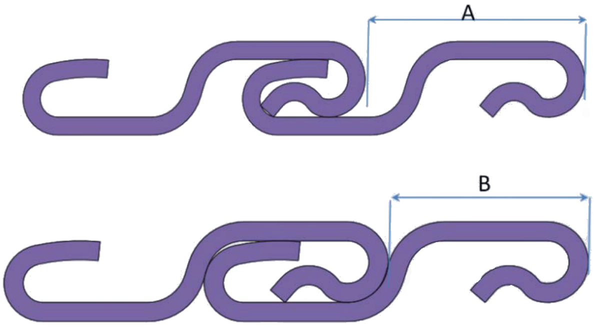

Figure 1.2: Interlocked carcass profile in maximum extended (A) and maximum compressed (B) condition.

(PA) or fluorinated polymers like Polyvinylidene fluoride (PVDF). Often there are additional layers extruded below or above the barrier to facilitate a smooth barrier profile with a lower stress concentration and thus extend the fatigue life of the barrier. The barrier material determines the maximum temperature limit of the pipe.

Flexlok Wire

The role of the flexlok is to support the barrier and provide resistance against hoop stresses. The layer consists of two shaped wires applied as a double helix. The interlocked flexlok profile is shown in Fig. 1.3.

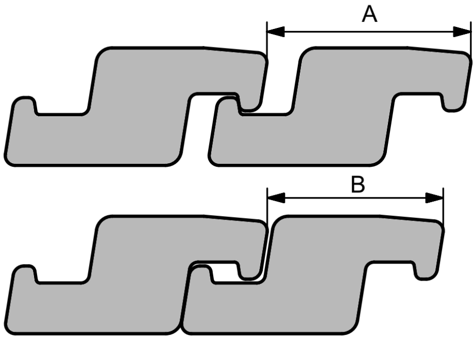

Figure 1.3: Profile of the interlocked flexlok wires in a maximum extended (A) and maximum compressed (B) condition.

Anti-Wear Tapes

Anti-wear tapes are wound in between wire layers to limit friction and allow for relative movement.

Tensile Wire

The tensile armour supports axial stress in the flexible wire and partially hoop stress as well. It consists of two layers of helically wound wires. The angle of application is selected depending on load analysis. The layers are wound in counter direction to prevent pipe twisting under load. Wires are flattened, which allows for tighter packing and reduces pipe thickness.

Anti-Buckling Tape

The function of the tape is preventing 'birdcaging' [10] of wires under a compressive load. Anti-buckling tape is applied over the final tensile wire layer. Those tapes are reinforced with glass or aramid fibres. A birdcage visualization is shown in Fig. 1.4.

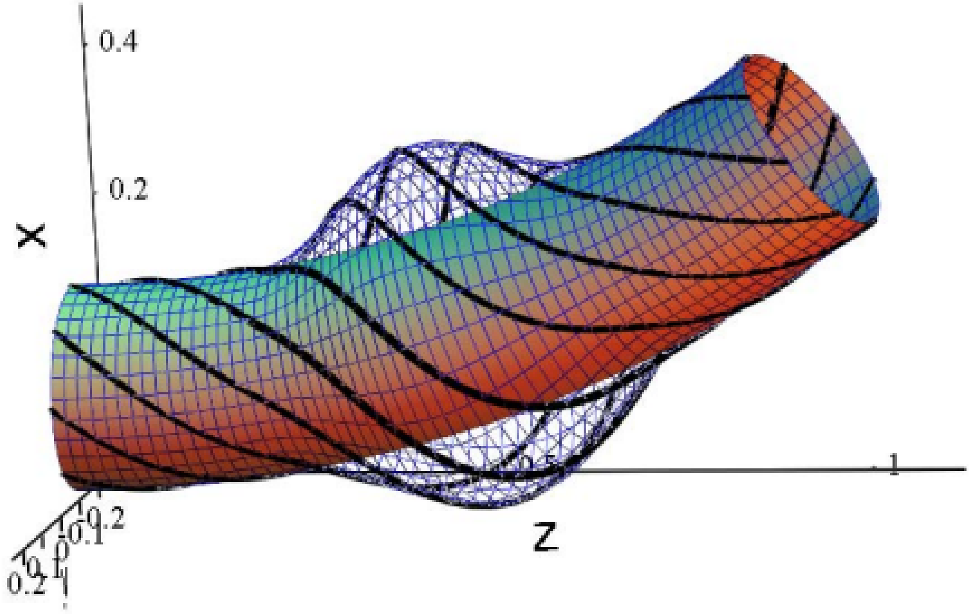

Figure 1.4: Simulation of a buckled tensile wires wires in a radial birdcage mode of failure [10].

External Sheath

The final layer is the outer sheath providing separation of wires from the external environment. It is an extrusion typically made of HDPE.

Termination

The pipe is terminated by end fittings on both ends. The end fittings are assemblies of forged steel components. The internal surface and ring groves are cladded with 625 nickel alloy. The barrier and the outer sheath are pressure tight sealed with a wedge seal rings. All other layers are securely fixed to the end fitting to provide required pull out strength. In particular, the tensile wires are secured with resin pumped into the end fitting. The visualization of the end fitting assembly is shown in Fig. 1.5.

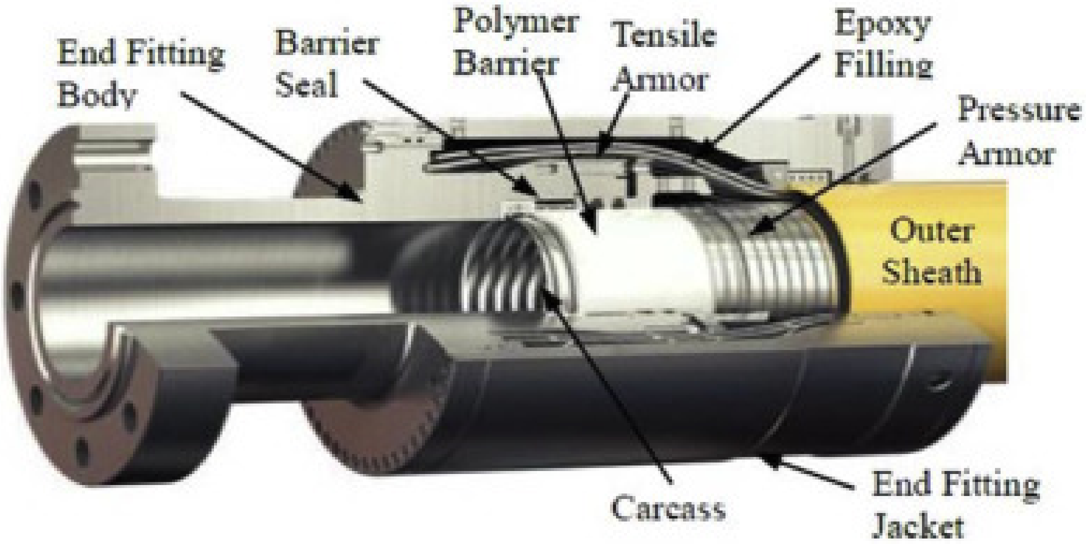

Figure 1.5: Cross-section of a flexible pipe termination [11].

Design Options

Each flexible pipe is designed and made to order to match the required bore fluid, water depth and loading. So far the most typical flexible pipe construction was presented. Depending on the project requirements, the following modifications can be made:

- In some pipe designs the carcass is unnecessary, and the pipe can be produced without it. The technical term for it is a smooth bore pipe,
- To limit the flow disruption from the carcass profile an additional 'T' profile can be inserted into the carcass to limit the apparent roughness,
- There may be additional polymer layers under or over the barrier to limit stress concentrations within the barrier and improve the fatigue performance,

- The number of wire layers can be higher, in particular there may be an additional layer made of flexlok wire, or the number of tensile wire layers can be increased to four,

- A thermal insulation can be added beneath the outer sheath,

- Fibre optic cables for monitoring can be added,

- The Flexlok wire can be replaced by a carbon fibre composite layer,

- In some designs there is an additional protection layer analogous to a carcass profile loosely fitted over the outer sheath and attached to the end fitting to protect the outer sheath from accidental damage.

1.4 Flexible Pipe Challenges and Failure Modes

The polymer barrier is not impermeable to gas. The diffusion of low molecular mass gases necessitates venting of the annular space, located between barrier and outer sheath. The venting system provides internal connection between pipes to the top of the pipe string. Venting occurs through vent valves. Spare vent valves are located on each end fitting. Without venting, the gas accumulation would cause outer sheath burst. Whenever the gases contain water, in an amount significant enough to cause condensation, and corrosive species like CO_2 and H_2S a fairly unique occluded corrosive environment is created. This corrosive environment can potentially be the cause of wire failure.

The flexible pipe failure modes are being monitored by the United Kingdom Offshore Operators Association (UKOOA) and by the Norwegian Petroleum Safety Authority (PSA). The latter manages the Corrosion and Damage Database (CODAM). The failure mode data were collated and analysed in a paper [12]. The summary is presented in a graph show in Fig. 1.6.

The main interest of this work - wire failure is categorized under 'other' category among failure modes which include hydrogen embrittlement of wires after outer sheath puncture, impacts, pigging accidents, ageing, wear, vibrations in gas pipes and sour corrosion caused by H_2S. Sour corrosion is almost non-existent phenomenon in the

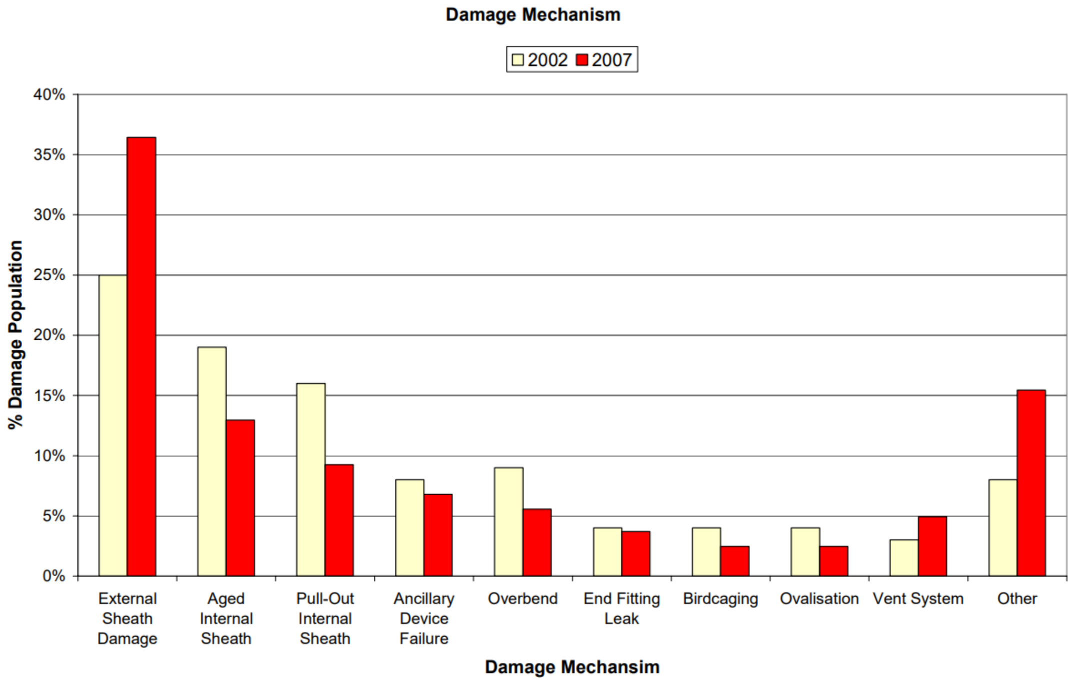

Figure 1.6: The most significant causes of damage to flexible pipes in 2002 and 2007 [12].

field, which suggests that the mitigation strategies are effective. The primary risk mitigation strategy is a wire qualification required by API 17J.

In 2017, the Brazil National Petroleum Agency (ANP) issued a failure mode alert after failure of three flexible pipes. This was found to be a new mode of failure, a stress corrosion cracking (SCC-CO_2) triggered by the presence of very high-pressure CO_2. Those conditions are unique to pre-salt fields and will not be considered in this work.

One of the limitations of the flexible pipe is the water depth and corrosive annulus conditions. The wire materials qualified for higher H_2S partial pressures are more expensive and are lower strength. The use of the lower strength wire increases the volume of steel used. It necessities more expensive ancillary equipment like bigger buoyancy. In general, flexible pipe risers already lag behind rigid risers, either TTR or SCR, in terms of maximum water depth as shown in Fig. 1.7. This becomes more evident when sour conditions are considered [13].

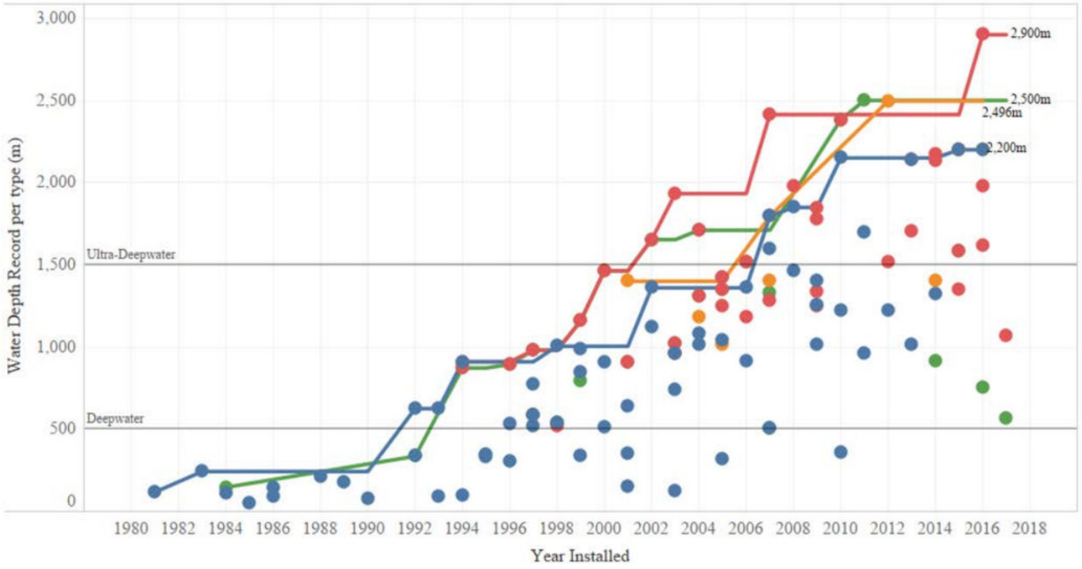

Figure 1.7: Chart showing a trend of increase of water depth of offshore developments. Flexible pipe risers lag behind SCR (Steel Catenary Riser) and TTR (Top Tension Risers) [14].

2 Problem Statement

The cold rolled tensile wire having 1,310 MPa to 1,482 MPa of Ultimate Tensile Strength (UTS) is the least expensive tensile wire grade used by Baker Hughes for the flexible pipe production. The wire was successfully qualified up to 1.5 mbar of H_2S in accordance with the requirements of API 17J. Whenever the bore conditions are sweet, but the well is expected to sour over time or trace amounts of H_2S are already present the high strength wire is the economical choice over sour grades.

A bath testing is a process where wire manufactured out of one steel cast (batch) is sampled and subject to fit for service testing in gas composition expected for the project. The batch testing is a client requirement and may be applicable to all or a certain percentage of wire batches used for manufacture of the flexible pipe. The batch testing may be carried out on samples of parent wire or welded wire.

The observed failure rate in batch testing is unpredictable, despite being carried out below the previously qualified H_2S limit. This unpredictable nature results in project delays, re-tests, overspending on spare material, issues with allocation of wire which failed testing to sweet service pipes. The overall cost to the Baker Hughes company is estimated to be in the order of few $ million per year.

The failures are attributed to two cracking phenomena happening to both parent and welded wire:

- Internal cracking near the wire centreline categorized as Hydrogen Induced Cracking (HIC)
- Surface cracking categorized as Sulphide Stress Cracking (SSC)

The scientific problem to be solved here is to understand the mechanism of failure to SSC in both parent and welded condition. From the business perspective the goal is to predict and mitigate failure to both HIC and SSC without changing the price.

3 Literature Review

3.1 High Strength High Carbon Cold Rolled Wire

3.1.1 Manufacturing

The tensile in focus of this work is controlled by a company purchasing specification MTL-5100. The specified UTS is 1,310 MPa to 1,482 MPa with minimum elongation of 3 %. The chemical composition limits are presented in Table 3.1.

Table 3.1: Chemical composition of the MTL-5100 wire.

Element	[%]
Carbon	0.60 - 0.70
Manganese	0.60 - 0.90
Silicon	0.15 - 0.35
Sulphur	0.02 max
Phosphorus	0.02 max

The wire manufacturing process starts with continuously casting billets or ingot casting. The second step in manufacturing is hot rolling followed by controlled continuous cooling. The wire microstructure shaped by this process consists of fine pearlite with a small amount of allotriomorphic ferrite. The round rod is subsequently descaled and subject to wire rolling. During the process, the wire achieves a flattened shape and about 50 % cross-section reduction. The wire can be manufactured in multiple sizes. Wire thickness varies from 2 mm to 7 mm, while the wire width varies from 8 mm to 12 mm. A typical microstructure is shown in Fig. 3.1.

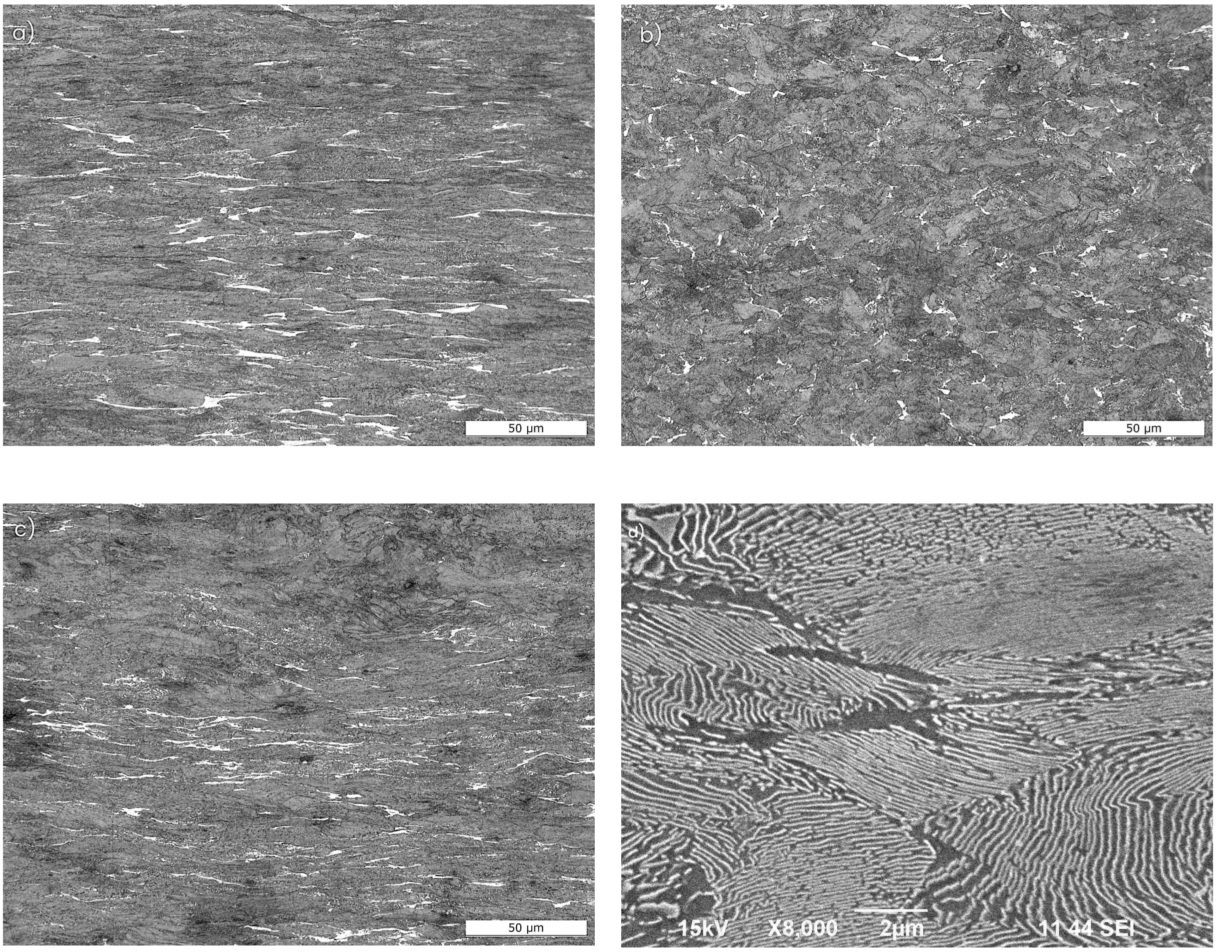

Figure 3.1: Microstructure of MTL-5100 wire a) Longitudinal section near the wire centreline shows axially elongated grains; b) Transverse section $\frac{1}{4}$ thickness above the centreline location showing apparently equiaxed grains; c) Transverse section near the centreline showing lateral deformation of grains. The centreline segregation shown on top of the picture shows much lower deformation; d) SEM image showing axial elongation of pearlite colonies and lamellae spacing near the wire centreline.

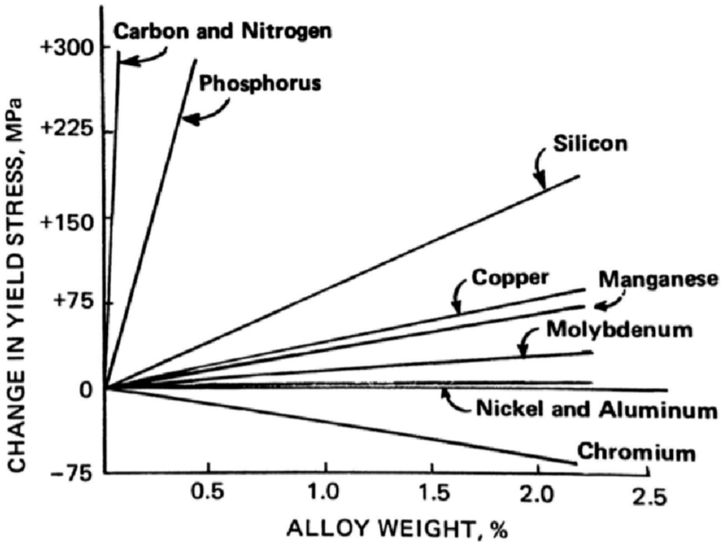

Figure 3.2: Solid solution strengthening effect in α-iron [19].

3.1.2 Strengthening Mechanism

The ferrite grains within the material are strengthened by the solid solution strengthening mechanism [15–17]. Carbon has the strongest strengthening effect, but the overall concentration is negligible [18]. The next potent strengthening element - nitrogen is blinded by aluminium added for degassing, and does not significantly contribute to strengthening. Phosphorus is a potent solid solution strengthener, however it tends to embrittle steel and is an unwanted contamination. The elements present in significant amount in solid solution are silicone and manganese. The strengthening potency is summarized in Fig. 3.2.

The wire microstructure consists mainly of pearlite which is a composite structure of cementite plates within the ferrite matrix. The plates are otherwise called lamellae. The strengthening mechanism, measured as yield stress (YS), of perlite is correlated with inter lamellar spacing λ, pearlite colony size d_c and prior austenite grain size d (3.1). Grain sizes are in mm [20]. This essentially is a Hallâ€“Petch equation, although lamellae are much finer than typical grains.

$$YS[MPa] = 52.3 + 2.18 \cdot \lambda^{-\frac{1}{2}} - 0.4 \cdot d_c^{-\frac{1}{2}} - 2.88 \cdot d^{-\frac{1}{2}} \tag{3.1}$$

Further strengthening is achieved by cold work. There are some parallels between the cold rolled and the cold drawn wires. The difference between the two is the die design and different deformation pattern. Drawing of the shaped wire is not feasible due to complicated die shape. The cold working of pearlitic wires allows for a very high strength of over 3 GPa, which is common for small diameter cold drawn wires. Those products are used for tire reinforcement, springs, piano wire, steel ropes, spokes, saw wire to cut silicon wafer and many other speciality applications. The cold rolled wire will benefit from the same strengthening mechanism, but will be characterized by lower cross-section area reduction. The preferred microstructure of the wire for drawing is fine pearlite with lamellae spacing between 70 and 90 nm [21]. This is typically achieved through patenting. Finer spacing increases the work hardening rate. The pearlite and bainite mixture after patenting is acceptable, but pearlite exhibits a higher work hardening rate. As described by [21] the cold work hardening occurs in two stages:

- Stage I - The deformation is largely confined to the ferrite within pearlite lamellae. Dislocation multiplication is followed by the formation of distinct sub-cell structures. The dislocation density increases to about 10% strain to reach a density of $5{\cdot}10^{15}\mathrm{m}^{-2}$. The density of dislocations is not increased further by cold work, but the number of active dislocations decreases with strain at high strain levels. Hardening rate is about 350 MPa per unit of strain.
- Stage II - Hardening is derived from the deformation of cementite. The hardening rate is typically 950 MPa per unit of strain. Deformation of cementite is easier the thinner the plates or in preferentially oriented grains. Moreover, the apparent lamellae spacing is greatly reduced.

The hardening behaviour is summarized in Fig. 3.3.

Cold work may induce deleterious effects like local dissolution of cementite, fragmentation, cracking, micro-void formation, formation of nano structures [22]. Examples are shown in Fig. 3.4.

The drawn wire has relatively low YS and elongation. The rolling after drawing improves axial elongation of wire and increases YS without sacrificing UTS. Such effect is attributed to Baushinger effect [23].

Wire deformation is non-uniform during the cold rolling operation. Modelling of that process is not in the scope of this work. However, just for illustration purposes a simplified 2D finite element analysis model where the deformation is achieved by

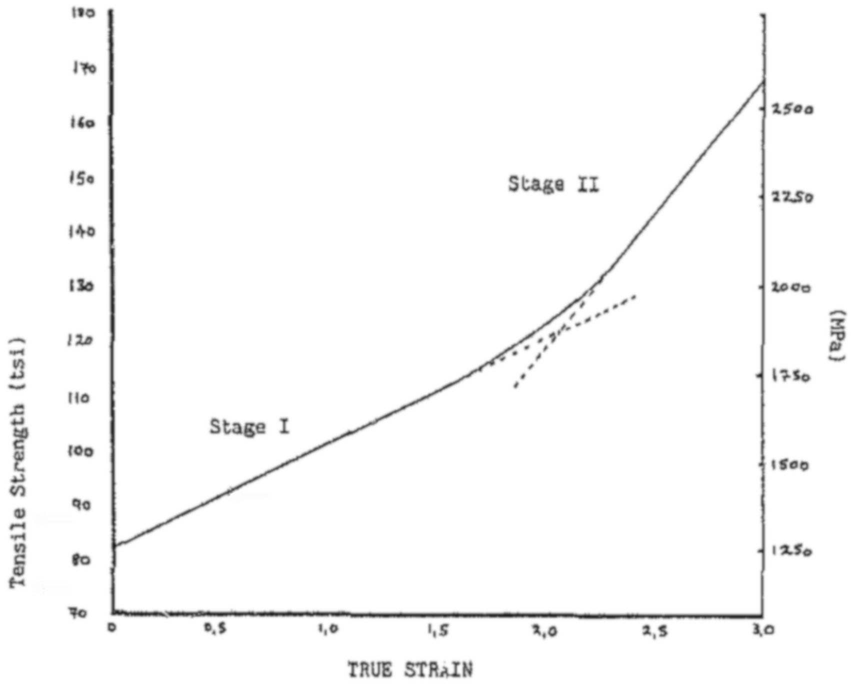

Figure 3.3: Work hardening of 0.80% carbon steel during drawing [21].

flattening of a round rod (no deformation in longitudinal direction) is presented here. A non-linear material model having YS of 800 MPa and a strain hardening coefficient of 0.15 was used. Using double symmetry of the wire profile, one quarter was modelled. The final wire dimensions correspond to 12x6 mm. The results are presented in Fig. 3.5. It can be seen that the deformation localizes at the centreline and diagonals. The rounded edges are subject to relatively low deformation.

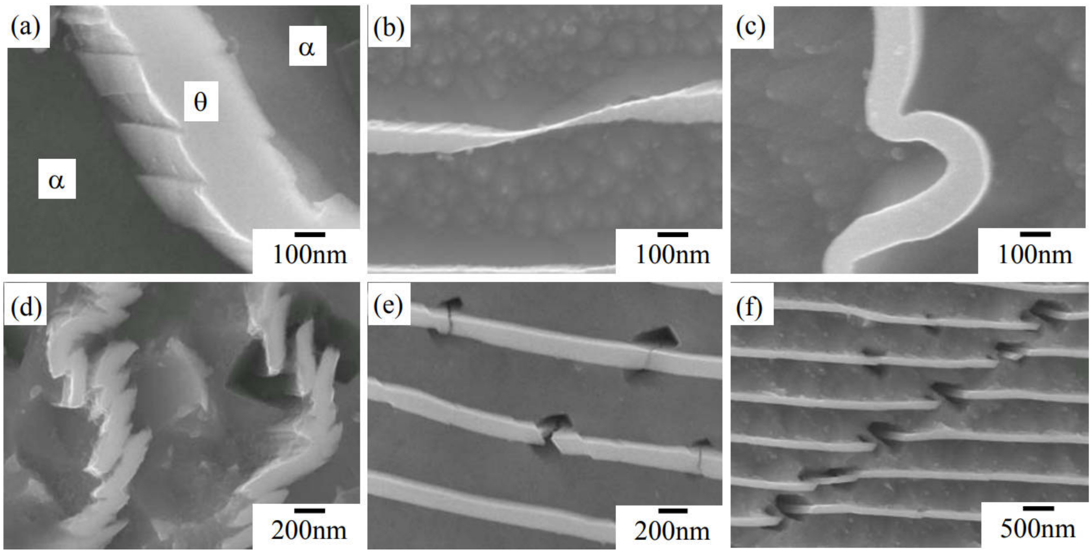

Figure 3.4: SEM micrographs showing various deformed morphologies of cementite in pearlitic Fe-0.76C steel after cold-rolled reduction (a), (b) 30 %, (c), (d) 60 % and (e), (f) 30 %. (a) Slip steps in cementite; (b) Thinning and necking of cementite lamellae; (c) Severely buckled cementite lamellae; (d) Fragmented cementite; (e) Fracturing of cementite lamellae likely due to tensile stress in the cementite plane; (f) Fracture of cementite plates in coarse pearlite by shear bands [22].

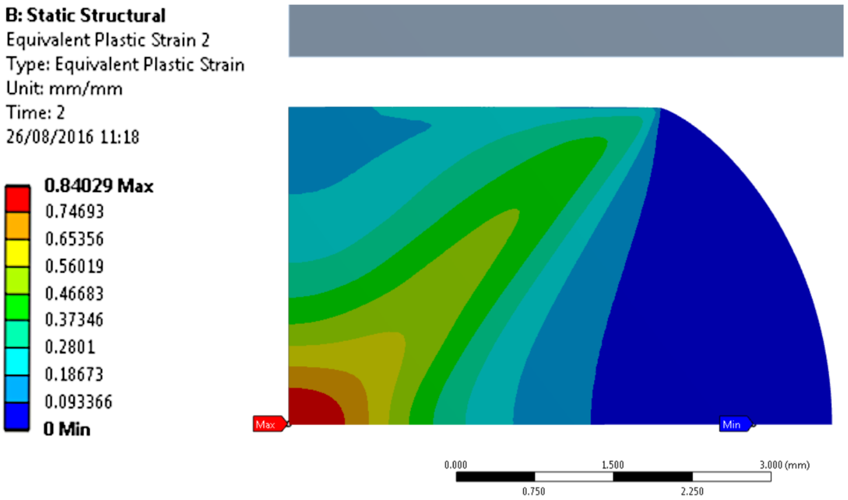

Figure 3.5: Visualization of a total deformation during wire flattening process. 2D model with non-linear material behaviour. Not fully representative of the actual wire rolling. Deformation localized near the wire centreline and diagonals.

3.1.3 Welding

During application of wires to the flexible pipe welded joints are required to join different coils of wire, or to fix unrepairable wire defects. The welding process is a modification of a resistance upset welding method. The process starts with preparation of wire ends to be perfectly flat and perpendicular to each other. Wire ends are clamped. A relatively small initial upset force is applied followed by high current that locally heats up the bond line. The material softens and deforms. After a certain distance travel, the current is stopped and high upset force is applied which pushes out the plasticized material. The modification of the standard method is that the lip formed from the plasticized material is sheared by welding dies, as shown in Fig. 3.6.

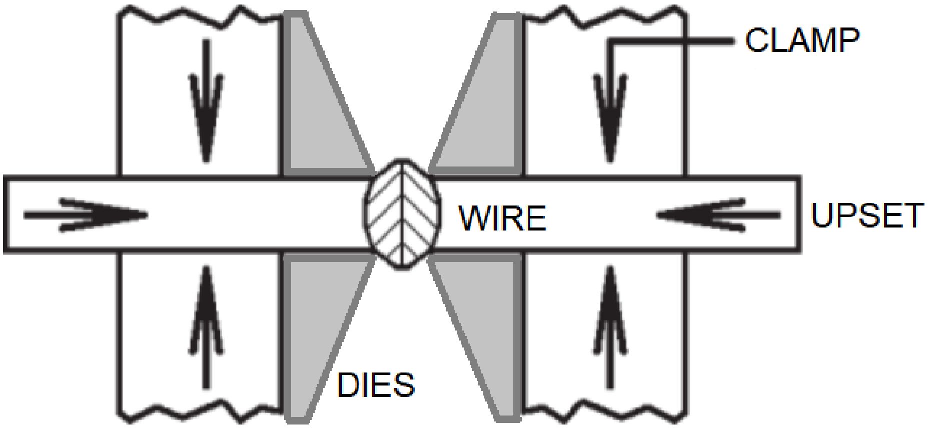

Figure 3.6: Schematic of the upset welding setup.

The weld is inspected for penetration, the extruded material is removed, and the weld area is ground flat. The weld area is subsequently Post Weld Heat Treated (PWHT) by a resistance heating. The tempering temperature is controlled in a feedback loop system based on a pyrometer reading. A typical stress relieving temperature is 500°C to 620°C, maintained over 20 to 50 seconds.

The qualification requirements for a weld are that:

- The all-weld UTS is greater or equal to 80% of the minimum specified UTS of the wire,
- The weld has to pass a bend test to a radius of four thicknesses of the wire profile.

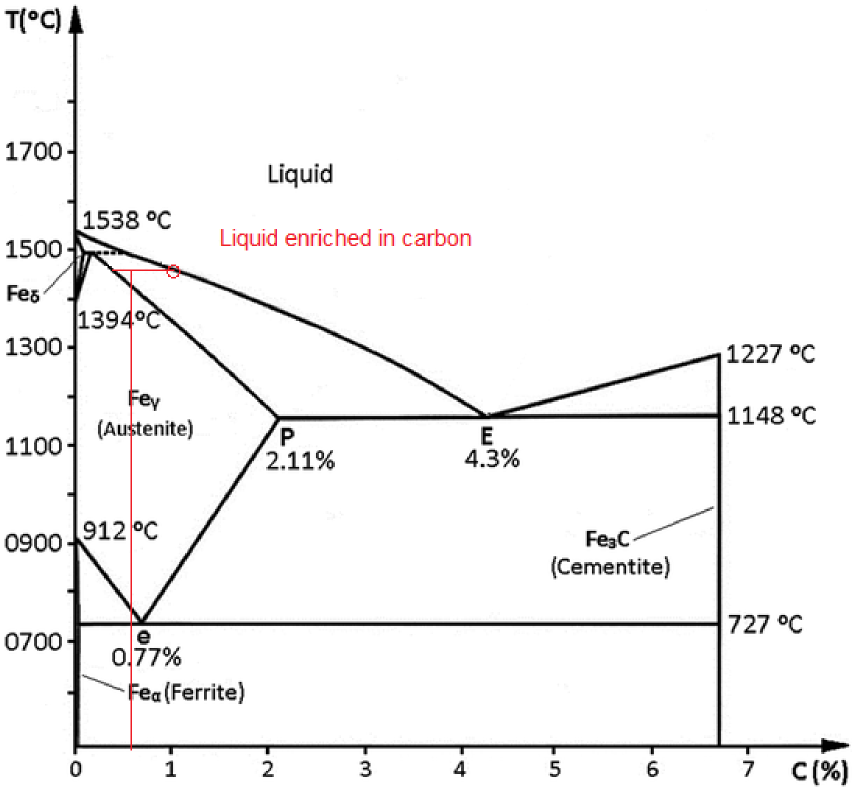

Figure 3.7: Fe-C phase diagram with lines explaining segregation of carbon to liquid during upset welding in the weld bond line. Modified from [24].

The upset pressure welding in practice involves partial melting of steel right on the bond line. The mixture of liquid and solid present in those conditions facilitates chemical segregation. Liquid steel is enriched in carbon. The mechanism is visualized on a phase diagram shown in Fig. 3.7. The liquid is removed during upsetting. The remaining material is depleted in carbon. Carbon depletion is evidenced by a change in the microstructure - formation of larger than expected from the lever rule amount of ferrite of Widmanstätten morphology.

3.2 CO_2 and H_2S Corrosion Mechanism

The corrosion is an electrochemical process which requires a transfer of the electrical charge. The cathodic reaction occurring at the corroding surface can be summarized as (3.2).

$$2H^+_{(aq)} + 2e^- \longrightarrow H_{2(aq)} \tag{3.2}$$

With H_2S present another path for cathodic reaction, called direct reduction, is introduced (3.3 & 3.4). The reaction (3.4) is also described as an autocatalytic process. It should be noted that this reaction is dependent on the pH. The lower the pH the higher the reaction rate.

$$H_2S_{(ads)} + e^- \longrightarrow H_{(ads)} + HS^-_{(ads)} \tag{3.3}$$

$$HS^-_{(ads)} + H^+_{(aq)} \longrightarrow H_2S_{(ads)} \tag{3.4}$$

H_2S is often called a hydrogen poison as it partially prevents production of hydrogen particles, instead it acts as catalyst for production of highly mobile hydrogen atoms. Those are readily adsorbed by the metal surface $H_{(ads)}$. Hydrogen atom is the smallest and most mobile element. The mobility is especially pronounced for metals with loosely packed lattice structures, like Body Cantered Cubic (BCC) of ferritic steels. Hydrogen Diffusion within densely packed crystallographic lattice of Face Centred Cubic (FCC) materials like austenitic steels and nickel alloys is orders of magnitude slower.

It has been argued in the literature whether CO_2 corrosion mechanism can follow a direct reduction route. In a series of relatively recent papers, S. Nesic has proven that the CO_2 direct reduction does not occur [25–27].

The CO_2 in a gaseous form dissolves in water. CO_2 forms carbonic acid by two reactions. At pH<8 direct hydration (3.5 and 3.6) is predominant. At pH>10 direct reaction with OH^- predominates (3.7).

$$CO_2 + H_2O \longrightarrow H_2CO_3 \tag{3.5}$$

$$H_2CO_3 + OH^- \longrightarrow HCO_3^- + H_2O \tag{3.6}$$

$$CO_2 + OH^- \longrightarrow HCO_3^- \tag{3.7}$$

The true ionization of carbonic acid is very small (3.7) and the reaction is sluggish [28].

$$K_1 = (H^+)(HCO_3^-)/(CO_2 + H_2CO_3) = 4.45 \cdot 10^{-7} \tag{3.8}$$

The carbonic acid production supplies H^+ for the cathodic reaction (3.1). This is also called a 'buffer' effect. For reference, distilled water saturated with CO_2 at 1 bar has a pH of about 4.

The uniform carbon dioxide corrosion is one of the most widely studied subjects in corrosion science and engineering. Numerous corrosion rate predictive models have been developed and reported in the literature over the past few decades. These models are grouped in four categories of empirical, semi-empirical, elementary mechanistic and comprehensive mechanistic [29], [30], [31].

Actual testing of the wires and very low H_2S levels is a slightly more complicated case of mixed CO_2/H_2S corrosion. NACE SP0110 [32] describes a rough rule for determining the sweet-sour transition by the CO_2:H_2S ratio based on experimental results. 2 mbar H_2S corresponds with a ratio of 500. Any H_2S partial pressure lower than that is expected to produce predominantly sweet corrosion. The corrosion rates in this environment are generally lower than in pure CO_2. Experiments have shown that CO_2:H_2S ratios from 500 to as high as 10,000 can still see a decrease in corrosion rate by almost an order of magnitude relative to the pure CO_2 condition [33]. A model of this process and experimental measurements are shown in Fig. 3.8. While a decrease in material loss may be favourable, the presence of the protective iron sulphide films can also make the underlying steels more susceptible to pitting [34].

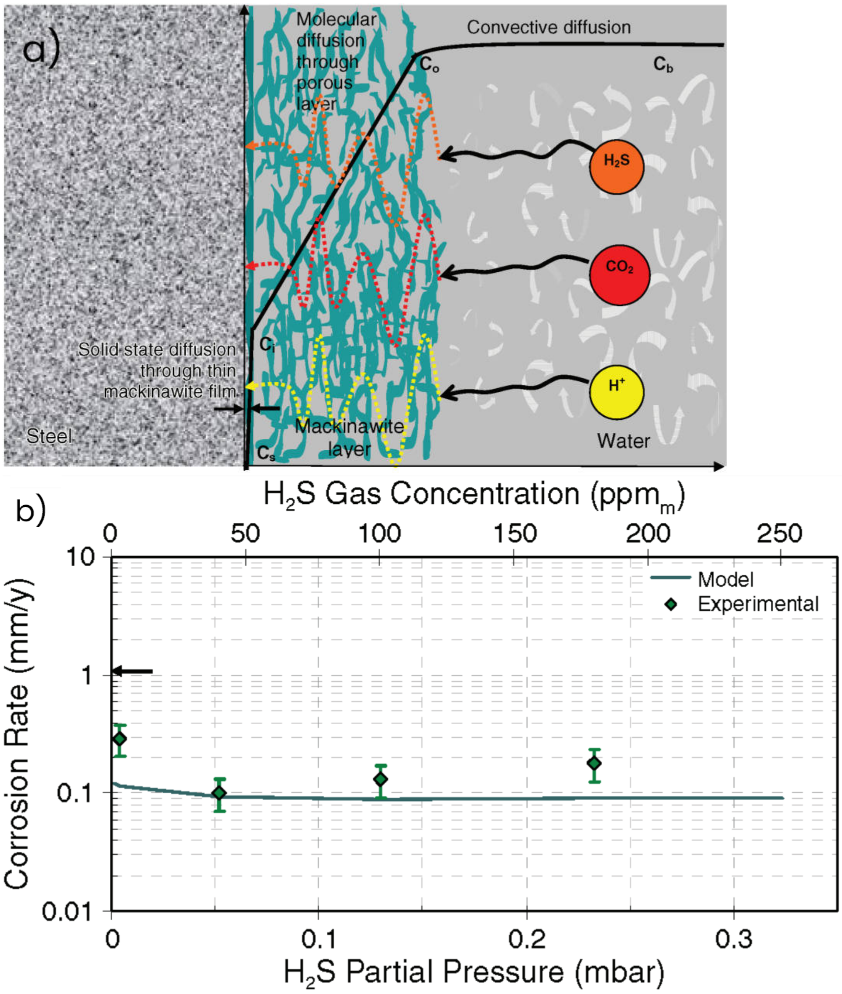

Figure 3.8: Effect of small additions of H_2S on sweet corrosion. a) Model of the protective effect of FeS (macknawite) film; b) Corrosion rate vs. partial pressure of H_2S; points are experimental data; lines are predictions of mechanistic model. 1 bar CO_2, 20°C, pH 5, reaction time 24h. Pure CO_2 corrosion rate is 1 mm/y and is indicated by an arrow [35].

3.3 Degradation Mechanisms

In the literature, there is a lack of consistent terminology regards to environmental degradation phenomena associated with sour service. One can encounter Hydrogen Embrittlement, Hydrogen Enhanced Cracking, Hydrogen Assisted Cracking, Hydrogen Environment Assisted Cracking, Hydrogen Induced Cracking, Stress Corrosion Cracking, Sulphide Stress Cracking, Blister Cracking, Hydrogen Delayed Cracking, Environment Assisted Cracking (EAC), Stress Oriented Hydrogen Induced Cracking and many more. This can be a source of confusion. The API 17J standard is concerned with three degradation mechanisms:

1. Hydrogen Embrittlement (HE)
2. Hydrogen Induced Cracking (HIC)
3. Sulphide Stress Cracking (SSC)

3.3.1 Hydrogen Embrittlement

Hydrogen Embrittlement is traditionally defined as the loss of ductility that many metals exhibit due to the presence of hydrogen atoms within the metal lattice. In the context of API 17J it is a cracking under stress induced by hydrogen ingress into the material from the process of cathodic protection by sacrificial anodes in seawater. In practical terms, those conditions can occur when the outer sheath is damaged near the end fitting where the sacrificial anodes are located. API 17J requires qualification testing of the wires to address this mechanism. Passing this test is not a challenge as the hydrogen concentration within the material from cathodic charging is lower than in sour service test. This mechanism will not be further addressed in this work in this context.

3.3.2 Hydrogen Induced Cracking

In the understanding of API 17J the HIC is used to describe all internal cracks within the wires. HIC occurs due to trapping of mobile atomic hydrogen in internal microstructural defects where the hydrogen recombines to molecules and forms a high pressure gas. This subsequently tears the metal around and causes crack propagation. The peculiar consideration for the researched wire grade is that there may be pre-existing cracks - centre bursts within the wire, which are interpreted as HIC during post-test inspection. The Eddy Current inspection method employed during manufacture of the wire does not detect internal cracks.

By Theory for Hydrogen Concentration [36] hydrogen may either dissolve into the normal interstitial lattice sites or reversible trapping sites like micro-structural voids in the metal. The two are at equilibrium with each other. According to Sievert's law this equilibrium is expressed as (3.9).

$$P_{(H_2)}[atm] = [ppmH]^2/K_{(ferrite)} \tag{3.9}$$

where for pure iron,

$$Log(K_{(ferrite)}) = -1418/(T + 1.628) \tag{3.10}$$

As an example, the equilibrium pressure for hydrogen concentration of 2 ppm at $20\,^{\circ}\mathrm{C}$ yields 482 atm of H_2 gas. Absorption of hydrogen into the material is reversible, however the internal cracking process once it occurs is non-reversible. HIC is an internal phenomenon such that the only effect of the environmental parameters is on the total, equilibrium levels of absorbed hydrogen in the steel.

Hydrogen amasses at microstructural defects such as voids, dislocations, grain boundaries and precipitates, which in turn act as traps. For each individual microstructural defect, there is a critical amount of hydrogen atoms N_C constituting sufficient internal pressure above which HIC will start. The parameters describing the critical amount are shape, size, distribution and density, neighbouring structure and segregation of impurities. In essence it is an inclusions problem. In equilibrium conditions, that critical amount of hydrogen is related to the critical dissolved hydrogen concentration H_C.

When the hydrogen charging time is limited the hydrogen will be diffusing to hydrogen traps, possibly without reaching the critical amount of hydrogen atoms N_C. Such consideration was carried out for MnS inclusions in [37]. The authors compared the model with an actual non-metallic inclusion distributions in pipeline steels. The findings are summarized in Fig. 3.9. Zone 1 is a zone where the critical hydrogen amount N_C is very high due to inclusions being very small and globular. HIC does not propagate in any time frame. Zone 3 is a sulphur range where the critical hydrogen amount N_C is not very high, but due to high density and large trapping capacity of MnS inclusions the steel is temporarily resistant to HIC until N_C is reached. The inclusions in zone 2 have a similar N_C to the zone 2, but the density is much lower, thus the HIC occurs much sooner.

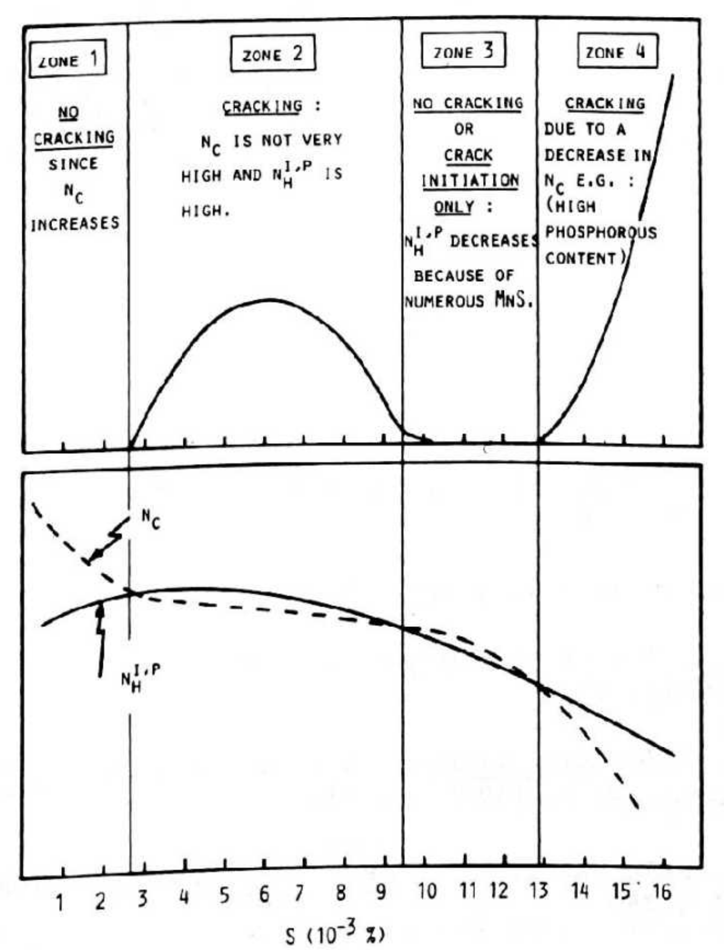

Figure 3.9: Top graph shows intensity of HIC in a function of sulphur in steel after a short time of hydrogen charging. Bottom graph shows critical amount of hydrogen for HIC initiation N_C and an actual hydrogen amount trapped to the inclusion $N_H^{I,P}$ [37].

3.3.3 Sulphide Stress Cracking

SSC is a subset of Environmentally Assisted Cracking (EAC) where the hydrogen ingress into material and crack formation is facilitated by H_2S. The crack propagation is assisted by hydrogen. Historically, there are three conceptual models for what can be called in general terms hydrogen embrittlement, as summarized below.

- Hydrogen-Enhanced De-cohesion (HEDE)

This theoretical conception assumes a truly brittle failure as the root cause of crack nucleation. Dissolved hydrogen is believed to lower the cohesive strength of the metal lattice at molecular level, particularity at grain boundaries. It is traditionally associated with intergranular fractures.

- Hydrogen-Enhanced Localized Plasticity (HELP)

  This theoretical conception is more recent. It describes HE as the result of the enhanced mobility of dislocations in the presence of solute hydrogen, leading to lower stresses required to move the dislocations and reduced ductility. HELP is associated with slip-band fracture types.

- Absorption-Induced De-cohesion Emission (AIDE)

  This theoretical mechanism assumes hydrogen that at crack tip facilitates the emission of dislocations ahead of the crack tip, resulting in the crack advancing through the developing micro voids. This is based on observations that there are considerable similarities in the appearance of fracture faces between hydrogen-embrittled fractures, liquid metal embrittlement, and SCC. AIDE has been connected with cleavage-like and dimpled intergranular fracture types.

A more critical appraisal of the models was presented in [38, 39]. SSC is a surface cracking phenomenon where contrary to HE in pure H_2 gas there are additional factors beyond concentration of mobile atomic hydrogen which affect the process of crack initiation.

Yamane's Model for SSC

As summarized in [40], it was experimentally found that SSC can occur both at cathodic and anodic polarization. Anodic polarization should limit hydrogen ingress, but was found in some experiments to exacerbate cracking. It was found that at cathodic potential, cracking can occur with no localized corrosion. Pitting corrosion is a prerequisite for crack propagation at corrosion potential and under anodic polarization.

Yamane [41] postulated an elegant mechanism explaining the SSC behaviour of low alloy steels. Pitting corrosion occurs as a consequence of formation of FeS protective film. During localized attack the corrosion potential within the pit drops due to Ohmic effects. At a certain depth (potential drop) the hydrogen evolution occurs at the bottom of the pit. At that point, the mechanism switches from Active Path Corrosion to Hydrogen Embrittlement. The SSC crack propagation is controlled by hydrogen flux. This model stipulates that the observed increase in SSC due to anodic polarization was caused by potential exceeding pitting potential and initiating pits. The protectiveness of the corrosion products plays a critical role in SSC resistance. The model is visualized in Fig. 3.10

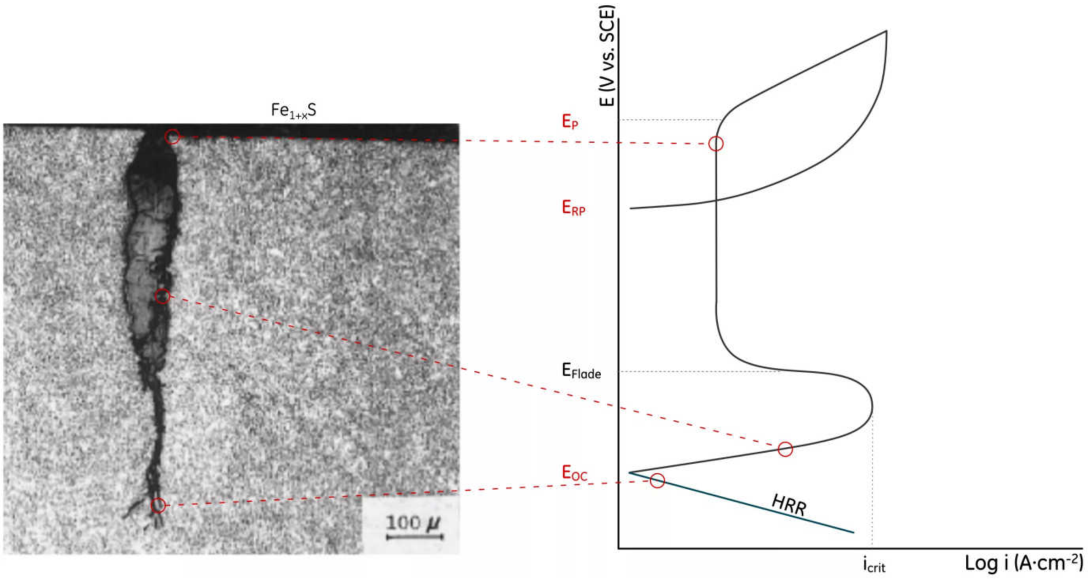

Figure 3.10: Graphical representation of Yamane's SSC model using an idealized anodic polarization curve. The image on the left represents the SSC of ASTM A203 [42] Grade E, quenched and double tempered, stressed to 90% of yield stress, etched with nital. Adapted from [40].

3.4 Accelerated Sour Service Testing

3.4.1 Hydrogen Induced Cracking

An article [43] summarizes the history of HIC testing in the following words: 'Ever since the production of wet sour gas started, problems with stress corrosion cracking, internal cracking and surface blistering have been reported. When some ruptures occurred in gas transition pipelines in the Persian Gulf in 1972 and in Saudi Arabia in 1974, the role of HIC as a damage-relevant phenomenon became more important.

The development of HIC tests started in 1973 with the BP or Cotton test, which was performed in an H_2S containing solution at pH 5 (artificial seawater). Either two or 6 sides of the specimen were exposed to the solution. Starting in 1979 NACE Task Group T-1F-20 began to develop test procedures for pipeline steels concerning HIC. Laboratory tests were performed to investigate the influence of the different parameters. At the beginning, the test solution consisted of artificial seawater saturated with H_2S at a pH of 5. With the improving steel cleanliness, the conditions became more severe. The test solution of pH 3, which is currently used in most of the standard tests, was adopted from NACE TM0177 [44] (...) The standard test duration is 96 h, which was found to be adequate to fully saturate the sample with hydrogen up to the equilibrium level for the test solution. After equidistant sectioning $\frac{1}{3}$ and $\frac{2}{3}$ along the length, the specimens are evaluated by means of metallography.

3.4.2 Sulphide Stress Cracking

There are multiple methods for evaluation of cracking susceptibility: constant stress, constant displacement, slow strain rate testing, fracture mechanics tests, corrosion fatigue tests [45]. The most widely used test methods on the Oil & Gas industry are described by NACE TM0177:

- Method A Standard Tensile Test
- Method B Standard Bent-Beam Test
- Method C Standard C-Ring Test
- Method D Standard Double-Cantilever-Beam Test

In method B a flat sample is bend in three points. Those tests last 720 hours. The drawback of the first three methods is that the result is binary, pass-fail. The method D measures K_{ISSC} (threshold stress intensity factor for SSC), which is a continuous variable.

State of the art methods involve fracture mechanics and measurement of crack growth rate [46, 47]. Those tests require a speciality setup and are not commonly used for SSC.

3.4.3 Wire Testing Procedure

The test method for tensile wires is based on EFC publication 16 [48] and NACE TM0316 [49] which describe a constant displacement four point bend method. The test is outsourced to external laboratories which can safely handle H_2S. The purpose of the test is to simultaneously verify resistance to HIC and SSC.

The test procedure can be summarized in the following steps:

- Sample preparation - the wire is cut into samples approximately 105 mm long. The surface is ground with 400 grit sandpaper and cleaned with acetone. The cut edges are protected with lacquer. A foil extensometer is glued to one side of the sample.

- Sample loading - the samples are placed in a fixture. The fixture is made of corrosion resistant nickel alloy except for the rollers contacting the wire which are made of hard polymer or ceramic. The sample is strained until 0.5 % total deformation is applied to the wire. The extensometer is subsequently removed. Any remains of glue are removed with sandpaper and the sample is de-greased with acetone. Fixtures are placed in a test vessel. A typical setup is shown in Fig. 3.11.

- Test solution is prepared in a separate vessel. The composition of the solution is shown in the Table 3.2. The solution is de-gassed by bubbling neutral gas followed by saturation with the test gas mixture. The vessel with samples is also purged with a neutral gas prior to the solution transfer.

- The samples remain in the vessel for the required duration of the test. There is a constant bubbling of the test gas and the temperature is maintained at 24°C.

- The vessel is purged with a neutral gas. The samples are removed, chemically cleaned and inspected.

- The Inspection consists of visual inspection under microscope at 50x magnification, magnetic particle inspection or penetrant inspection, ultrasound inspection and sectioning.

The test result is a number of failed samples out of samples tested and a failure mechanism. The typical acceptance criteria are three out of three samples passing the test or at least four samples out of five samples passing the test.

Table 3.2: Chemical composition of the modified NACE TM0177 solution B

Chemical	[%]
NaCl	3.0
Acetic Acid	2.5
Sodium Acetate	0.41
NaOH or HCl	adjust pH to target

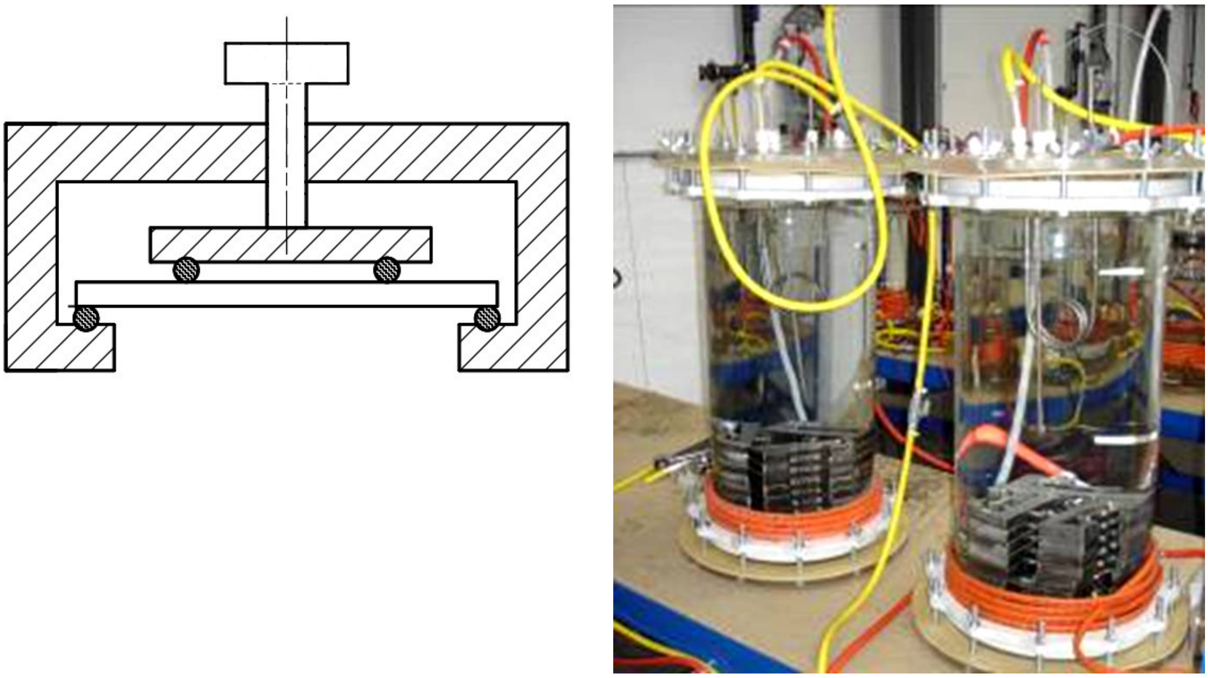

Figure 3.11: A typical test setup for the sour service test. Schematic of a fixture for four point bend stressing of the sample. Test vessels freshly filled with the test solution.

The NACE TM0177 solution B when saturated with H_2S is expected to have pH 3.4 - 3.6. Majority of the sour service tests on wires are performed at pH 5.0 or higher as predicted by the gas permeation analysis. The addition of sodium hydroxide to adjust pH lowers the buffering capacity of the test solution. Acetate buffer looses its buffer effect at pH 5.6. As a general comment Citric acid/citrate buffer may be a more appropriate choice in those conditions. Complexing agent like EDTA or ascorbic acid may be added to further modify the protectiveness of the corrosion products and stabilize the corrosiveness of the test solution. A High-strength Line Pipe (HLP) research committee from the Iron and Steel Institute of Japan postulated recently alterations to the NACE solution B which doubles the concentration of acetic acid and sodium acetate. The corrosion rate and hydrogen permeation were measured comparing those solutions [50]. While the corrosion rate was fairly uniform in time, the hydrogen permeation showed a sharp peak within minutes from the test start. The hydrogen flux stabilized after 3 days to a value about 25 % of the peak, as shown in Fig. 3.12. HLP test solution in those tests performed favourably to the standard NACE test solutions providing a more stable test environment in terms of pH change, corrosion rate change, and hydrogen flux. This result emphasizes the effect of the corrosion product build-up, its protective function and the decrease in protectiveness caused by acetic acid.

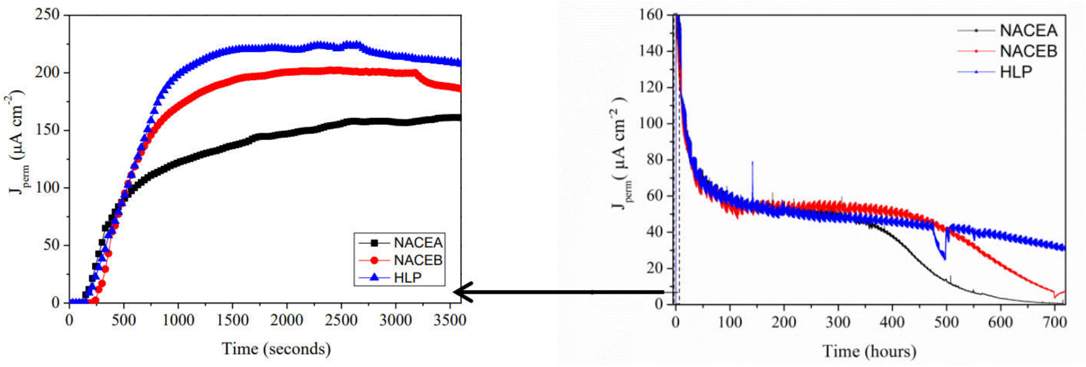

Figure 3.12: Hydrogen permeation in X65 pipeline steel membrane exposed to buffer solutions under 1 bar H_2S [50].

3.5 Microstructure Effects on the SSC Resistance

As summarized by Pressouyre [51] the models for hydrogen embrittlement, listed in section 3.3.3, are not general enough to account for all cases. The most general postulate is that there is a critical hydrogen concentration at which cracks are induced or assisted C_K and an amount of hydrogen trapped within the material C_H. The crack will be initiated when C_H increases to or above C_K. The solutions to hydrogen problems are then categorized as:

1. Solutions based on a decrease of hydrogen C_H, trapped in the material,
    (a) Directly formed barriers - metallic or non-metallic coatings,
    (b) Indirectly formed barriers - whenever the hydrogen is evolved within corrosion products those products can be modified to act as hydrogen recombination sites. The additions of noble metals Cu, Ag, Au, Pt ... were proven effective,
    (c) Decrease of hydrogen activity - corrosion inhibitors,
    (d) Trap additions - deliberate addition of hydrogen traps may delay saturation of sites where cracks nucleate. This strategy is effective when the source of hydrogen activity is temporary. For this solution to work the following should be true:
        i. added traps should have a high C_K,
        ii. the quantity of added traps should be high enough to lower C_H of 'bad' defects,
        iii. traps should be irreversible,
        iv. traps should be homogeneously distributed in the matrix.
2. Solutions based upon an increase of the critical concentration C_K, for crack initiation or assisted propagation,
    (a) Modification of inclusions or particles: size, shape, density and distribution,
    (b) Modification of grains: size, segregation of elements affecting grain boundary cohesive strength, crystallographic orientation of grains and trapping character,

(c) Dislocations - dislocations can be static or dynamic, movement of dynamic dislocations may transport hydrogen to critical sites,

(d) Microstructure - fine and round carbides are generally more resistant to crack initiation than coarse and angular ones,

(e) Avoidance of segregation zones.

From the corrosion perspective, it is acclaimed that pearlite is the preferred steel structure. The corrosion potential of cementite is more cathodic than ferrite's. The corrosion products precipitate between lamellae, producing tight and fine-grained film anchored to the steel via cementite 'scaffolding'. An observation of such scaffolds in ferritic-pearlitic K55 and N80-1 steels [52] is presented in Fig. 3.13.

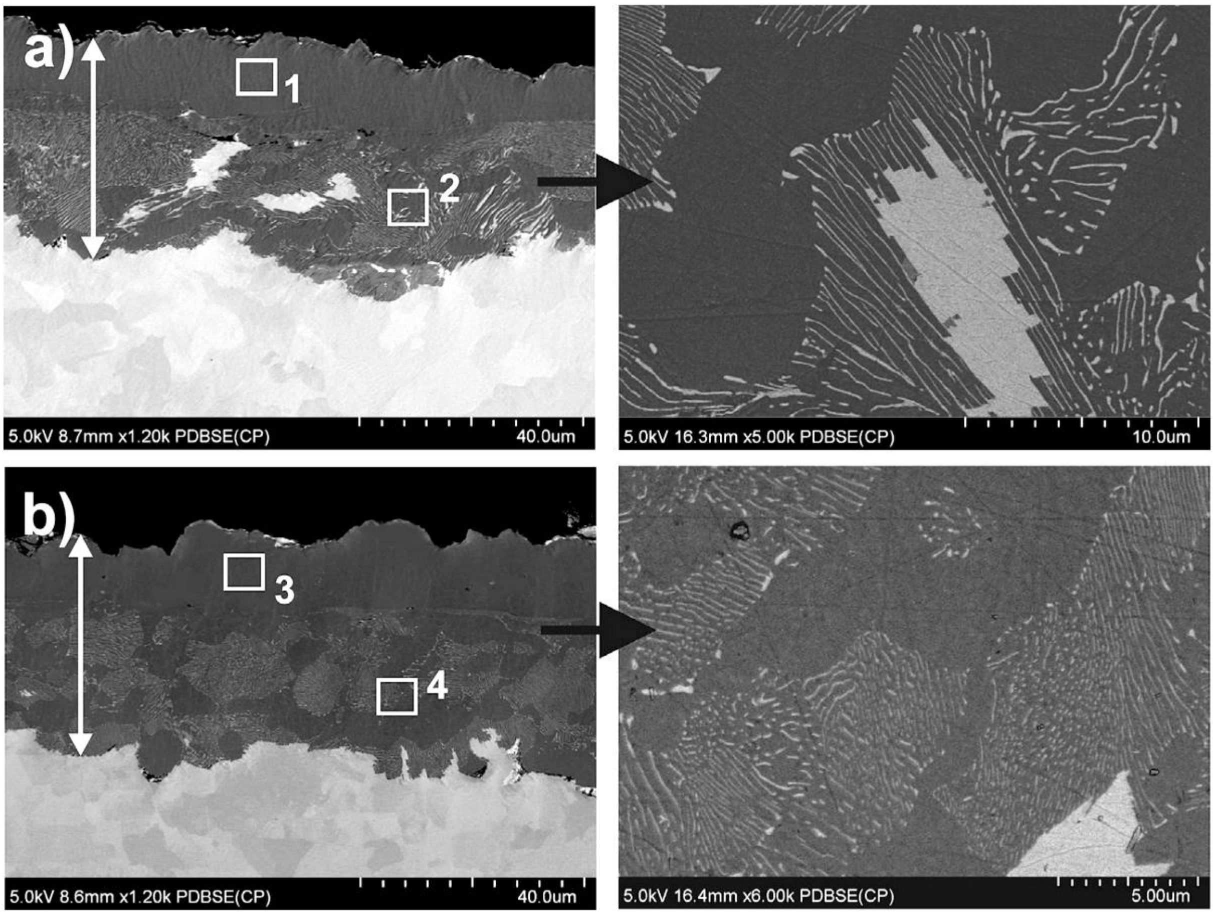

Figure 3.13: SEM observation of morphology of corrosion products layer produced in a 96-h test at 50 bar CO_2 at 50°C, 40 g Cl^-/L. a) steel K55, b) steel N80-1. Pearlite scaffold remains within the inner layer of the corrosion products [52].

When tested for the hydrogen permeation, the fully pearlitic steels are expected to show relatively greater drop in hydrogen flux from peak to the stable value. It has been shown [53] that the pearlite lamellae spacing affects hydrogen diffusivity and trap density of the steel. In the referenced work, fine pearlite resulted in high hydrogen trap density and low diffusivity as shown in Fig. 3.14. Lamellar pearlitic steel is superior to the other more spheroidized tensile wires microstructures in terms of diffusion coefficient [54] and was reported superior to martensitic thermo-mechanically treated steel [55]. It was reported in the literature that cold drawn martensitic steel improved the resistance to hydrogen degradation. The effect was is attributed to trapping of hydrogen on defects, alignment of elongated dislocation cell walls with the wire axis and decreased transverse wall spacing, all effects which are accentuated by increasing drawing strain. The beneficial effects of increased strain are thought to be limited eventually by the formation of internal fissures and voids [56]. Similar conclusions were made for drawn pearlitic steel, but in addition an effect of crack deflecting was emphasized [57].

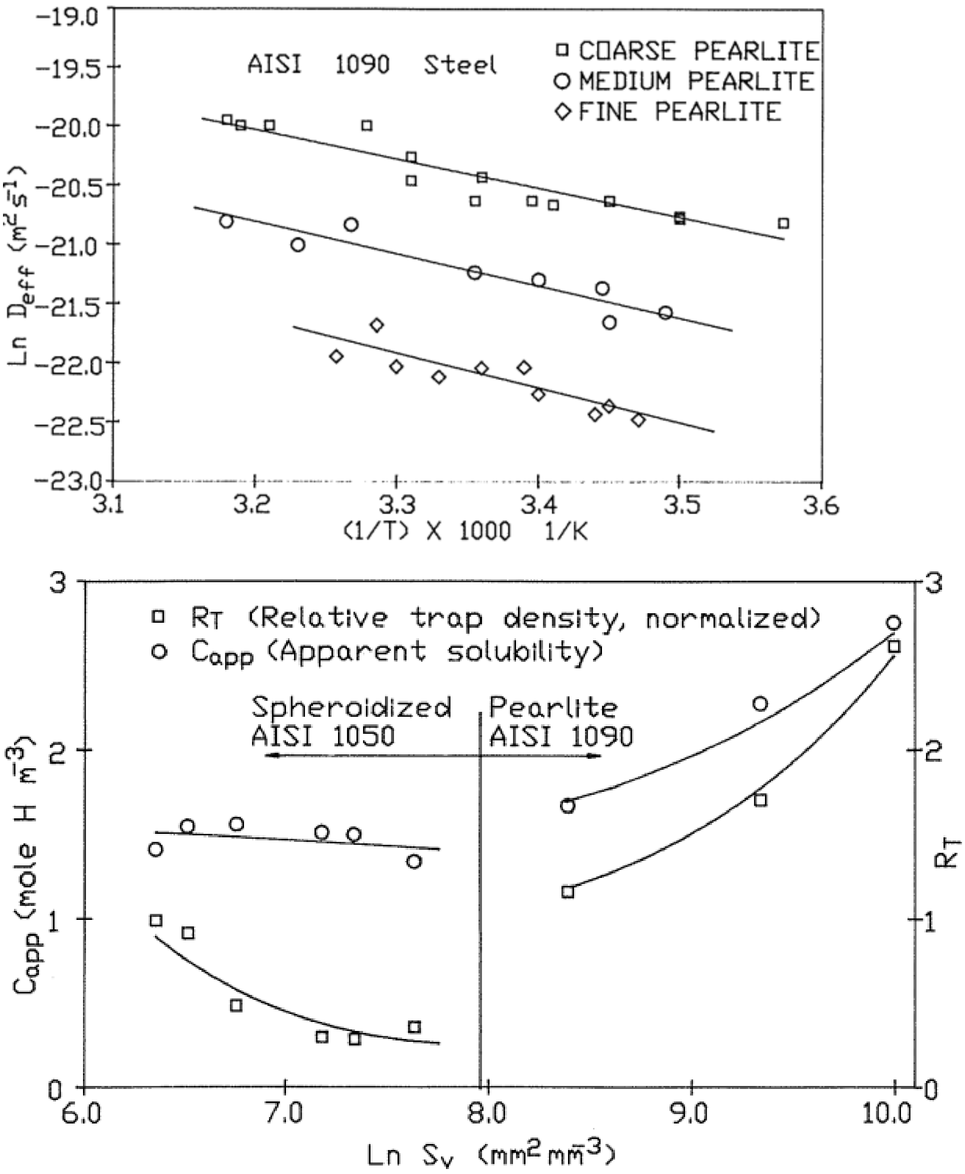

Figure 3.14: Apparent solubility and relative trap density of spheroidized and pearlitic microstructures as a function of carbide/ferrite interfacial area. Effective diffusivity vs inverse temperature as a function of pearlite fineness [53].

SSC Resistant Steels

It is a consensus in the industry that the susceptibility to SSC is related to mechanical properties of steels, namely the higher strength the higher susceptibility to SSC. It was codified in the standard NACE MR0175 [58] that the carbon and low alloy steels (with some grades being excluded from the rule) with hardness $\leqslant$ 22 HRC are resistant to SSC at H_2S partial pressure up to 1 bar. In those conditions only general corrosion is expected. To allow use of higher strength steels in mild environment [59], the NACE standard gives rules for fit for purpose qualification. In summary the qualification consists of testing three casts of material in service pH and H_2S conditions. This allows use of high strength materials like C110 or C125 casings having hardness up to 30 HRC.

In the design of high strength low alloys resistant to SSC there are four global trends:

1. Acicular ferrite and granular bainite microstructures [60]

2. 1Cr-0.8Mo-Nb steels [61], [62]

3. W alloyed steels [63], [64]

The acicular ferrite morphology toughens the microstructure as randomly oriented ferrite grains effectively deflect propagating cracks. Those developments are limited to pipeline steels having less than 0.1 % C. The other two designs increase the grain boundary cohesion and introduce high density of non-reversible hydrogen traps in the form of carbides. The alloying elements have to be in the ferrite's solid solution to be able to segregate to grain boundaries. The carbon content of those steel grades is limited to 0.35 %.

Grain Boundary Cohesion

Grain boundaries play a key role in crack propagation. For hydrogen embrittlement a reverse effect - decrease of grain boundary cohesion is especially problematic. Temper embrittlement is a known phenomena in low alloyed steels caused by segregation of phosphorus. In nickel alloyed steels also tin, bismuth and arsenic segregate to grain boundaries and partake in temper embritlement. The segregation occurs in a temperature range 420 °C to 580 °C. The hydrogen embrittlement shows synergistic deleterious effect of with the temper embrittlement [65–67]. There are multiple ways in which temper embrittlement can be mitigated - control of heat treatment so that exposition in the sensitive temperature region is minimized, addition of 0.15 to 0.35 % molybdenum, control of phosphorus levels to very low values, or when possible use of plain carbon steels with manganese content lower than 0.40 %.

In some alloys it is possible to use grain boundary engineering techniques to manufacture a high density of special grain boundaries that show improved resistance to hydrogen embrittlement [68]. Another approach is segregating elements that increase the cohesion energy. The driving energy for segregation and grain boundary cohesion are shown in Fig. 3.15 for simple binary alloy. The embrittling effect of copper should be noted. It should be also noted that segregation energy and cohesion effect depend on the crystallographic orientation of particular grain boundary. Of particular interest of this work is grain boundary coherence modelled in presence of hydrogen. Results of such analysis are summarized in Fig. 3.16. The figure shows interaction energy between solute and hydrogen on the grain boundary energy. Silicone has slightly beneficial effect, and manganese shows no effect on grain boundary cohesion in the presence of hydrogen. On the other hand those elements favour grain boundary segregation of phosphorus, which effect was not modelled in the work, and can significantly decrease the grain boundary cohesion [69]. The authors concluded that boron [70], tungsten and rhenium have a potential grain boundary strengthening effects in steels charged with hydrogen.

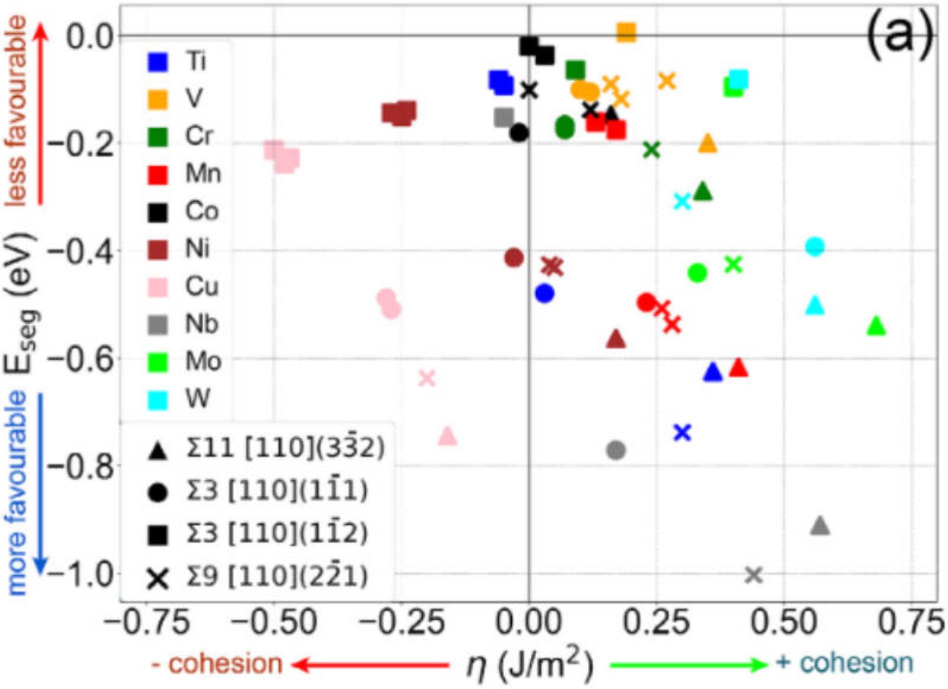

Figure 3.15: Transition metal interactions and how they affect cohesion in α-iron. The minimum segregation energy (E_{seg}), representative of tendency for a particular element to segregate to a GB, is plotted against their effects on GB cohesion when segregated (1 atom). (2a) The cohesion effect (η) that a segregated element has on the relaxed GB cohesion (Methods) is plotted against E_{seg} [71] .

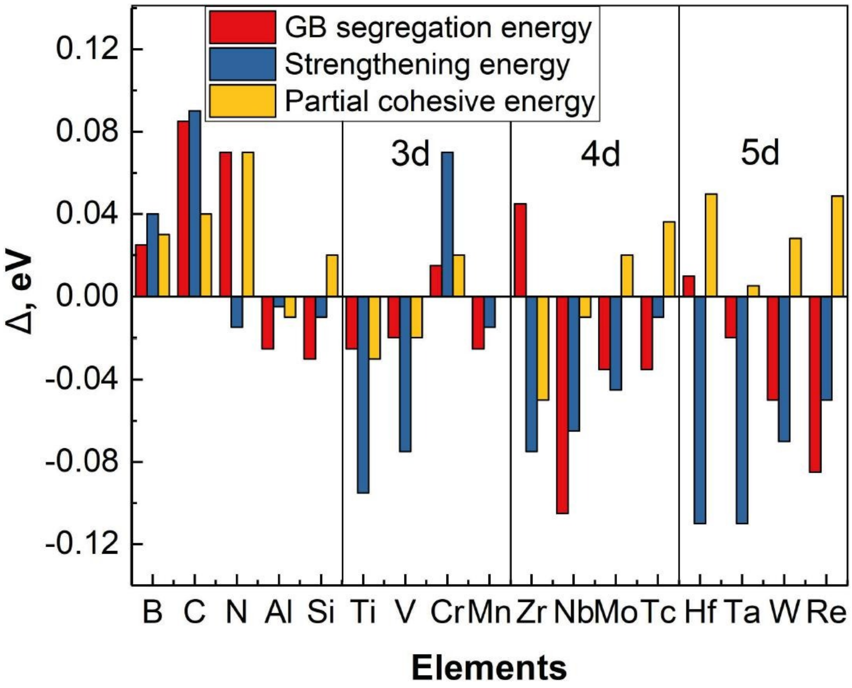

Figure 3.16: The effect of H-solute interaction on the GB segregation, GB strengthening and partial cohesive energy. The positive or negative sign of the interaction energy indicates repulsion or attraction between H and a solute atom respectively [72].

4 Methodology of Microstructure Evaluation of Wires

The microstructure analysis of the tensile wires is to a degree problematic. The material readily corrodes. Ultra fine and cold worked microstructure etches poorly with standard etchants. Some features necessitate the use of SEM, and others require speciality etching methods. Significant progress was achieved since 2014 when the evaluation of batch test failures began being carried out in the Materials Laboratory dedicated to Engineering Design Center in Warsaw. This chapter summarizes the developed procedures.

4.1 Sample Preparation

The wire samples require mounting in, unless otherwise stated, non-electrically conductive resin. Whenever there are cracks (SSC or HIC) to be examined, the sample surface shall be briefly ground dry. Surface voids should be filled with an epoxy resin, preferentially under vacuum. During wet grinding, the samples shall be dried as soon as possible in-between grinding steps. At least the last step of grinding shall use waterless coolant. Due to local soft spots, hand grinding or polishing is impossible. Polishing using 3 μm diamond suspension is generally sufficient.

4.2 Revealing the General Microstructure

It was found that etching using nital is inappropriate for such fine microstructure. The literature [73] suggests amyl nital or Goerens' amyl picral which produce significantly better results. The drawback of picral is that it does not reveal grain boundaries.

The best results were achieved using a water solution of 5 % ammonium persulfate $(NH_4)_2S_2O_8$ with few mg of EDTA per 100 ml. The approximate etching time is 10 s. This solution has the advantage of clearly revealing bainite features in a way that it can be distinguished from pearlite or martensite with optical microscope. Results of etching with this solution are presented in Fig. 3.1 a), b), c). The SEM inspection shown in Fig. 3.1 d) was after etching with picral.

4.3 Revealing the Prior Austenite Grain

Prior austenite grain boundaries are partially revealed by allotriomorphic ferrite when the general microstructure is revealed. It was found that modified Marshal's etch provides the best delineation of that feature, along with pearlite colony grain boundaries. The etching solution consists of two pre-mixed solutions A and B that are mixed directly before etching. Solution A consists of 8 g of oxalic acid, 5 ml of concentrated H_2SO_4, 100 ml of water. Solution B consists of 100 ml of 30% hydrogen peroxide. Modification of the standard etching solution is by adding a few drops of HF. Etching is carried out by immersion for about 4 s. The etched surface needs to be kept vertical to avoid pitting. Grain boundary delineation can be further enhanced by secondary etching for 20 seconds in saturated water solution of picric acid with EDTA. An example of etched microstructures is shown in Fig. 4.1. The result is degraded in areas of high plastic deformation.

4.4 Revealing the Manganese Segregation

Manganese segregation manifests as bands within the wire. In longitudinal sections those are revealed by etching with nital as dark etching areas. In transverse sections the only sign of segregation are areas with reduced deformation of grains. A special three-step etching procedure was developed to reveal that feature.

1. Electrolytic etch in 20% KOH saturated with picric acid at 8V for 40 s. Saturated solution requires a few mg of picric acid per 100 ml. The solution is left stirring overnight and filtered before use. Unfiltered solution causes pitting. The etchant selectively attacks cementite.

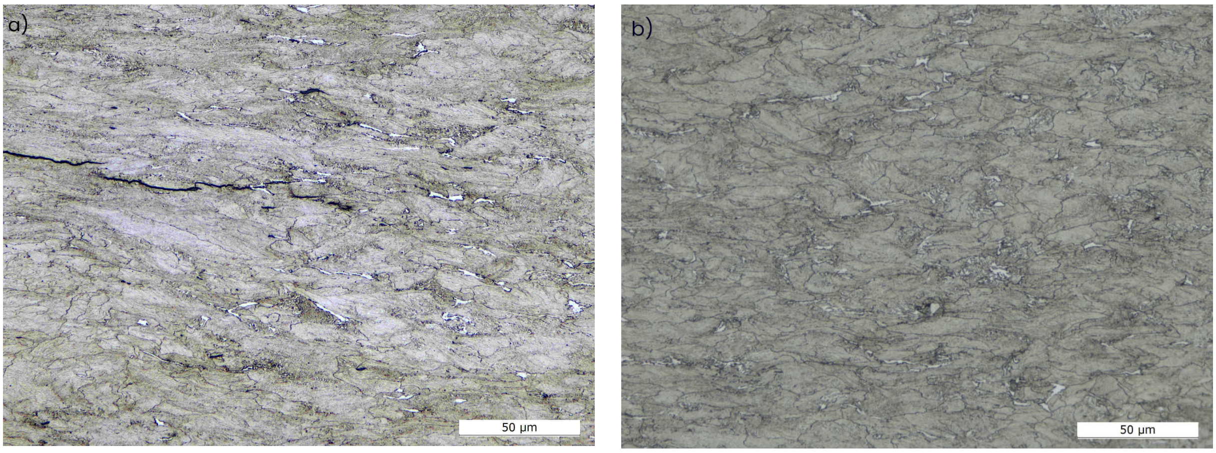

Figure 4.1: An example of prior austenite grain boundaries etched with modified Marshal's etch followed by secondary etching in saturated water solution of picric acid and EDTA. a) Microstructure near centreline. HIC present. Grain boundary delineation is poor in heavily plastically deformed areas; b) Microstructure near surface above centreline reveals flattening of grains. Grain boundary delineation is good.

2. 0.5% Nital 3-5 s. This step is required for surface activation.
3. 40 ml glycerin (waterless), 3 ml HNO_3, 6 ml HF 5-10 s. General microstructure is revealed. Manganese rich areas are etched dark brow as shown in Fig. 5.12.

For welded or heat treated samples step 3 is sufficient.

4.5 Revealing the Phosphorus Segregation

Phosphorus segregation can be revealed with a standard Oberhoffer etchant [74], but requires for the samples to be mounted in electrically conductive resin. The recipe for the etching solution is 100 ml water, 100 ml ethanol, 3 ml HCl, 0,2 g $CuCl_2$, 3 g $FeCl_3$ and 1 g $SnCl_2$. The procedure requires immersion etching for about 30 s. Phosphorus enriched regions are white. For transverse sections, the contrast is greatly improved by pre-etching with alkaline potassium picrate as per steps 1 and 2 of the previous procedure. An example of the difference is shown in Fig. 4.2.

An alternative procedure involving the use of potentiostat gives a very good results, but was barely used due to labour intensiveness. The sample needs to be connected

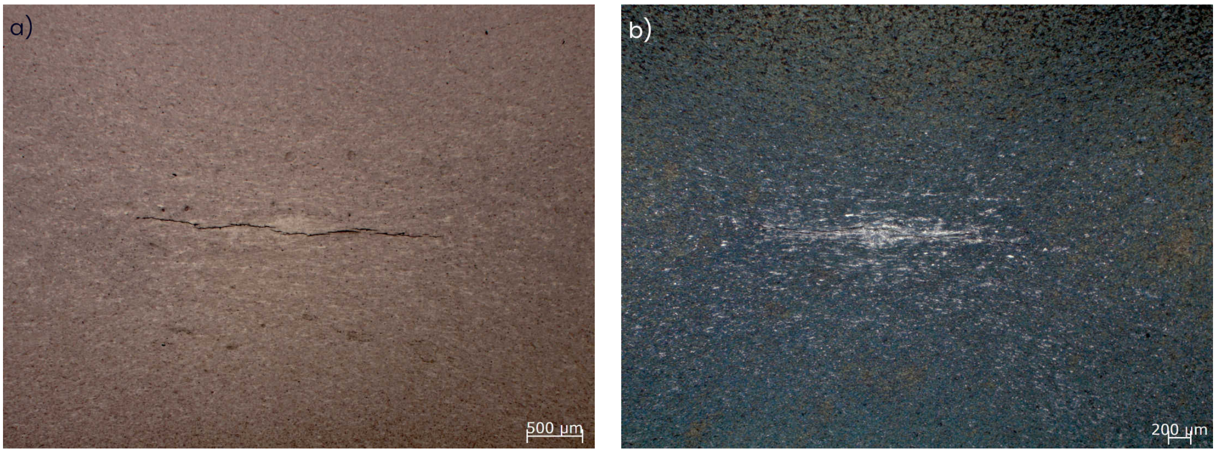

Figure 4.2: An example of transverse section of sample where phosphorus segregation is revealed near the centreline region where HIC is present. a) Oberhoffer etch; b) Pre-etching with alkaline potassium picrate followed with Oberhoffer etch.

to insulated electrical leads. The procedure involves potentiostatic etching for 240 s at -680 mV vs. Ag/AgCl reference electrode in 2N Na_2SO_4 with 2 ml 1N H_2SO_4 per litre of solution. The etching reveals general microstructure with similar resolution as amyl nital. Regions where phosphorus segregates remain non-etched (white).

4.6 Revealing the Distribution of Manganese Sulphide Inclusions

Typically, ASTM E45 [75] or ISO 4967 [76] are used for non-metallic inclusion evaluation. Those standards specify inspection of polished samples at 100x optical magnification. Inclusions finer than 2 μm are ignored. The inclusions in the majority of wires are finer than that limit. Those standards can not evaluate the spacial distribution of inclusions thus are of limited value for this work.

The following procedures colour inclusions and allow easier evaluation. The limitation is that only sulphide type inclusions are revealed. Etching is carried out in a solution of 0.1 g ammonium persulfate $(NH_4)_2S_2O_8$ per 100 ml of water by immersion for 20 s. The inclusions and nearby microstructure is stained. General microstructure is not revealed. An example of etching effect is shown in Fig. 4.3 a). In areas of high density of inclusions, the individual inclusions may become unintelligible due to staining overlap. An improvement of this procedure is achieved by addition of 1 ml of H_2SO_4 and 1 ml H_2O_2 per 100 ml of solution and swab etching. The modified etchant tints manganese sulphides black, leaves an unaffected halo around inclusions, and reveals general microstructure away from the inclusions. An example of inclusions revealed by this procedure is shown in Fig. 4.3 b).

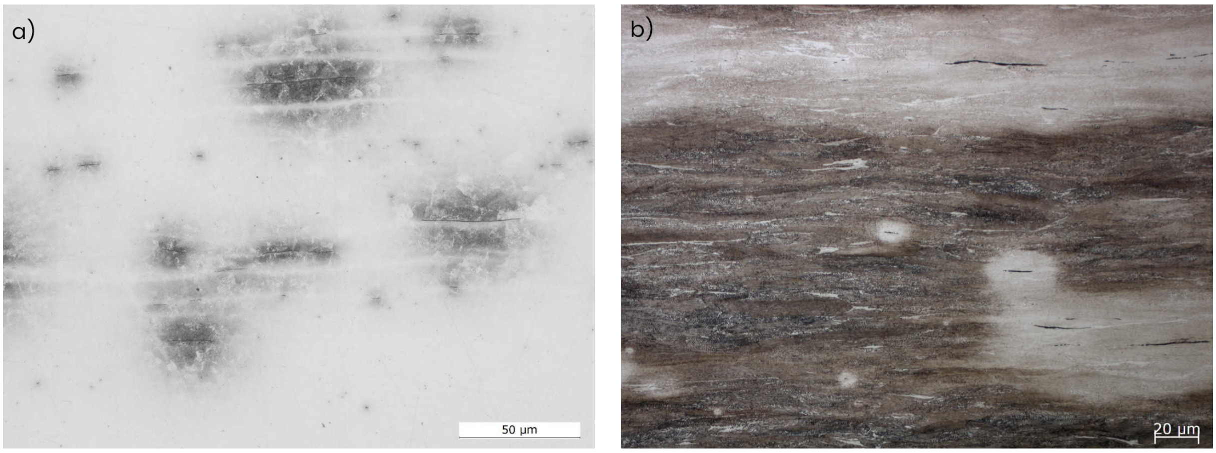

Figure 4.3: Manganese sulphide inclusions coloured by speciality etching procedures. a) Standard procedure; b) Modified procedure.

5 Microstructure Evaluation Results and Observations

This chapter summarizes:

- meaningful findings from analyses of the samples after the batch testing,
- welding trials and tempering temperature effect,
- correlation of anisotropy of mechanical properties to HIC.

The last item is published [77], results are briefly summarized in this chapter. Please find the full paper in Appendix A.

Ideally, all the microstructure characterization methods listed would be used for every analysis, so there is a full characterization of each batch of the wire. To date no single MTL-5100 wire batch was fully characterized. Some of the results presented here were a part of an attempt to link a microstructural feature to a failure mechanism with a statistical significance. With this approach, there were always complications like, samples that could not be etched properly despite multiple attempts, one-off samples with unique features and out-layers performing against predictions. The findings of this chapter are anecdotal evidence and indications of trends.

5.1 Parent Material SSC

The wire surface in as manufactured state is at least partially decarburized. A case decarburization reaching down to $80\,\mu\mathrm{m}$ is shown in Fig. 5.1 a). After the sour service test, the ferrite layer is never observed. Prior to testing the samples are ground by hand with sandpaper, but it was never established how deep the grinding is. After the test the sample surface profile is fairly smooth in a sense that there is not trace of preferential corrosion of ferrite. The voids after corrosion of ferrite grains seem to be a potential stress rises. What's worse the decarburization occurs along prior austenite grain boundaries which are more susceptible to hydrogen embrittlement.

The other observation is that pearlite colony grain boundaries near the surface are decorated with granular and film-like cementite particles as shown in Fig. 5.1 b). This is fairly uncommon for locations closer to the core. It was found that the prior austenite grain size varies from ASTM 5.5 to 7.5. The grain size based on the pearlite colonies size is form ASTM 7.5 to 9. Ferrite morphology varies from typical allotriomorphic to more granular morphology as shown in Fig. 5.2.

Evaluation of SSC failures shows a pattern. The wire corrosion is somewhat non-uniform. There are regions which develop shallow pitting. This can occur both at the tension and compression side of the wire. Microcracks begin to develop from the bottom of pits on the side of wire in tensions. Microcracks deeper than approximately $500\,\mu\mathrm{m}$ become unstable and lead to a complete fracture of the sample. An evaluation of SSC failure and microcracks is shown in Fig. 5.3.

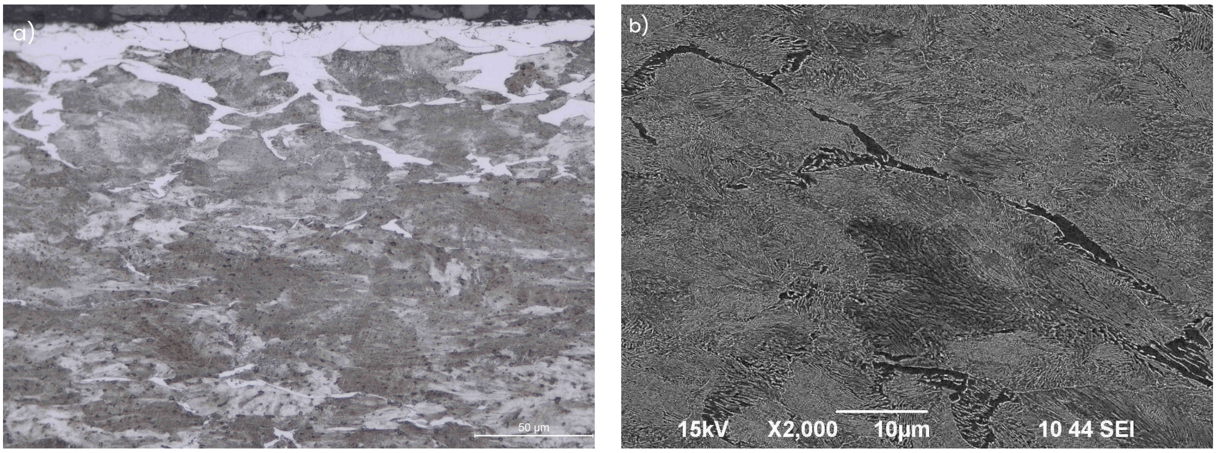

Figure 5.1: Microstructure subsurface. a) Decarburization depth; b) SEM revealing pearlite-bainite microstructure with allotriomorphic ferrite. Cementite film is decorating grain boundaries.

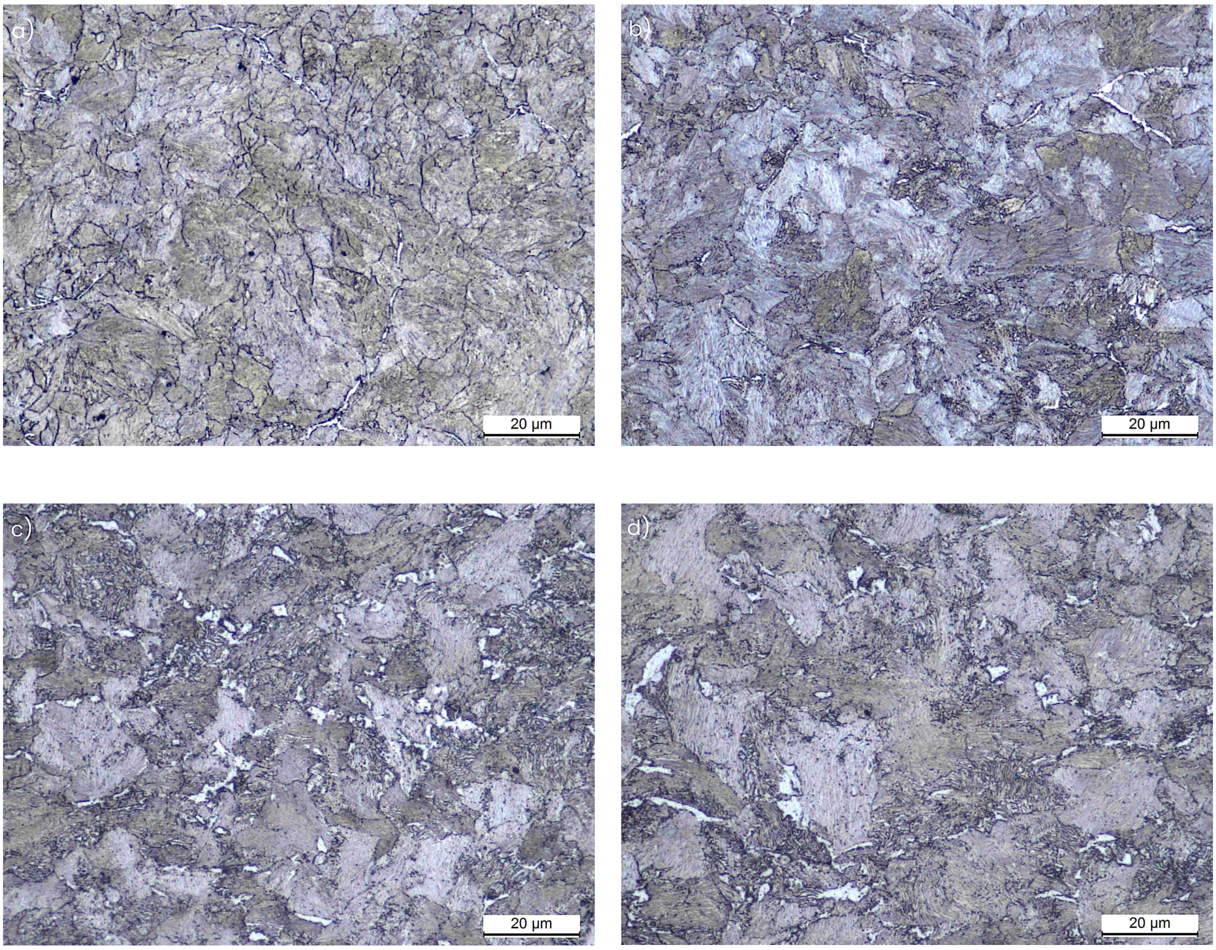

Figure 5.2: Microstructure subsurface etched with modified Marshall etch, reveals grain size and ferrite morphology. a) b) allotriomorphic ferrite; c) d) allotriomorphic and granular ferrite

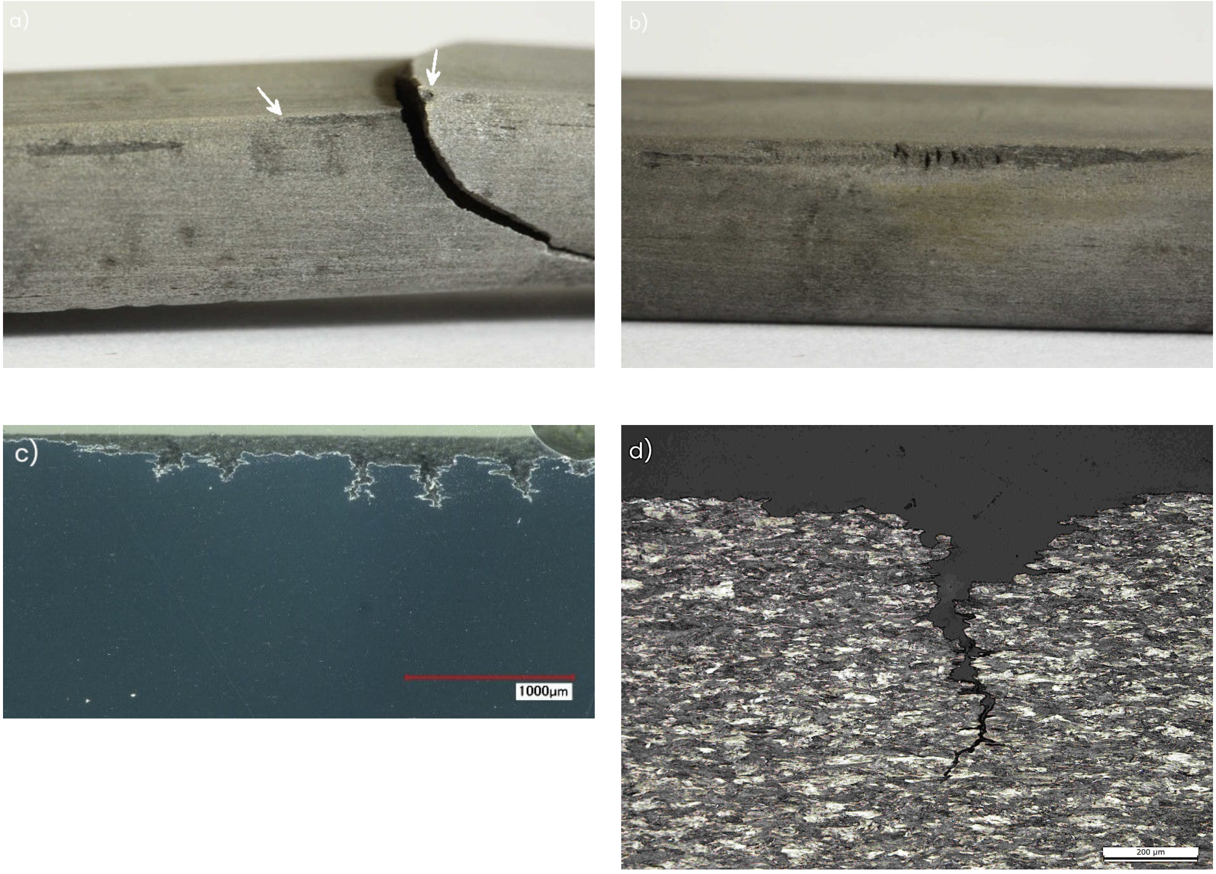

Figure 5.3: Evaluation of a typical SSC failure. a) SSC initiating from a pit indicated by arrows; b) Localized corrosion - shallow pits and microcracks observed on the same sample; c) Metallographical section through the pitting. Sample mounted in translucent resin. The pit depth is about $250\,\mathrm{\mu m}$ *and microcracks are about* $450\,\mathrm{\mu m}$ *from the surface. d) Transgranular propagation path.*

5.2 Weld SSC

5.2.1 Morphology

The weld SSC is associated with two distinctive morphologies of corrosion and pitting.

1. Semicircular independent deep pits located on both sides of the bond line, typically up to 1 mm away, as show in Fig. 5.4,

2. Shallow, round interconnected pits with etched bottoms as shown in Fig. 5.5. Pits are located next to the bond line and up to 3 - 5 mm away from it.

There are also wires which show features in-between those two. The common feature of both pitting morphologies is that the bond line itself appears to be more resistant to corrosion. The corrosion maximum is located $400\,\mu\mathrm{m}$ to $700\,\mu\mathrm{m}$ from the bond line centre. Evaluation of cross-sections through pitting suggests that cracking initiates when the pit reaches the critical depth of about $500\,\mu\mathrm{m}$ regardless of the pit morphology.

5.2.2 Phosphorus Segregation

The phosphorus segregation in longitudinal cross-section was revealed with Oberhoffer's etch. The white lines indicating phosphorus segregation are denser and wider near the centreline. The lines are bent toward the surface and exit near the bond line. This pattern is an expected consequence of the material upset during welding. The width of the zone where those lines meet the surface is $500\,\mu\mathrm{m}$ to 1 mm, as shown in Fig. 5.6 a). Once initiated, the crack favours propagation along the phosphorus segregation bands. There are interconnecting cracks propagating through regions without segregation. The crack at the macro scale remains about $500\,\mu\mathrm{m}$ from the bond line as shown in Fig. 5.6 b). The observed pits do not favour the high phosphorus spots, as shown in Fig. 5.6 c). There are surprisingly common occurrences where cracking does not occur, but very deep pits are observed. This morphology is also categorized as SSC in the batch test reports. Those samples show preferential corrosion, but it is not aligned with phosphorus segregation as shown in Fig. 5.6 d)

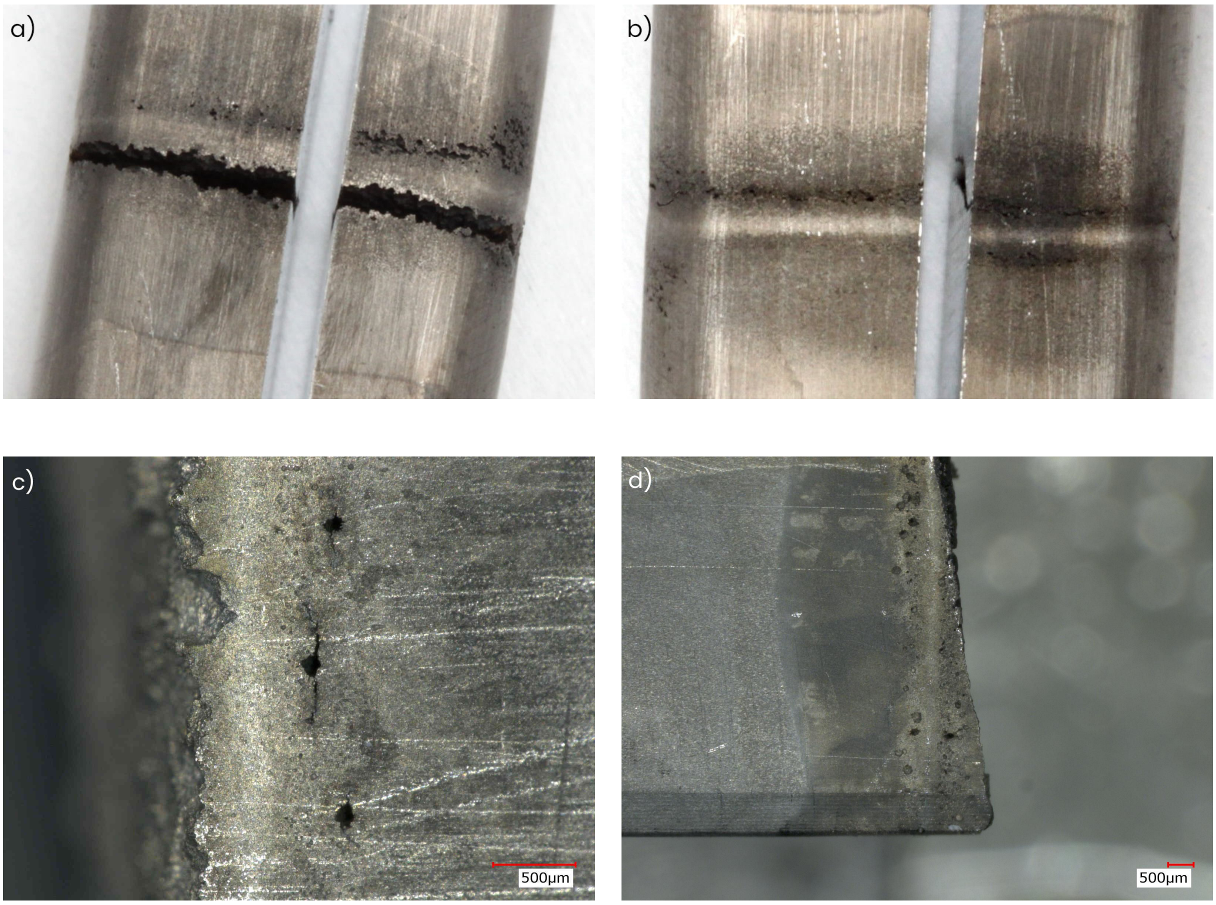

Figure 5.4: Evaluation of a typical SSC failure of weld initiated on independent deep pits. a), b) same sample, tension and compression side respectively. Wire width is 10 mm; c) microcracks initiating from deep pits; d) deep pits filled with dark corrosion product.

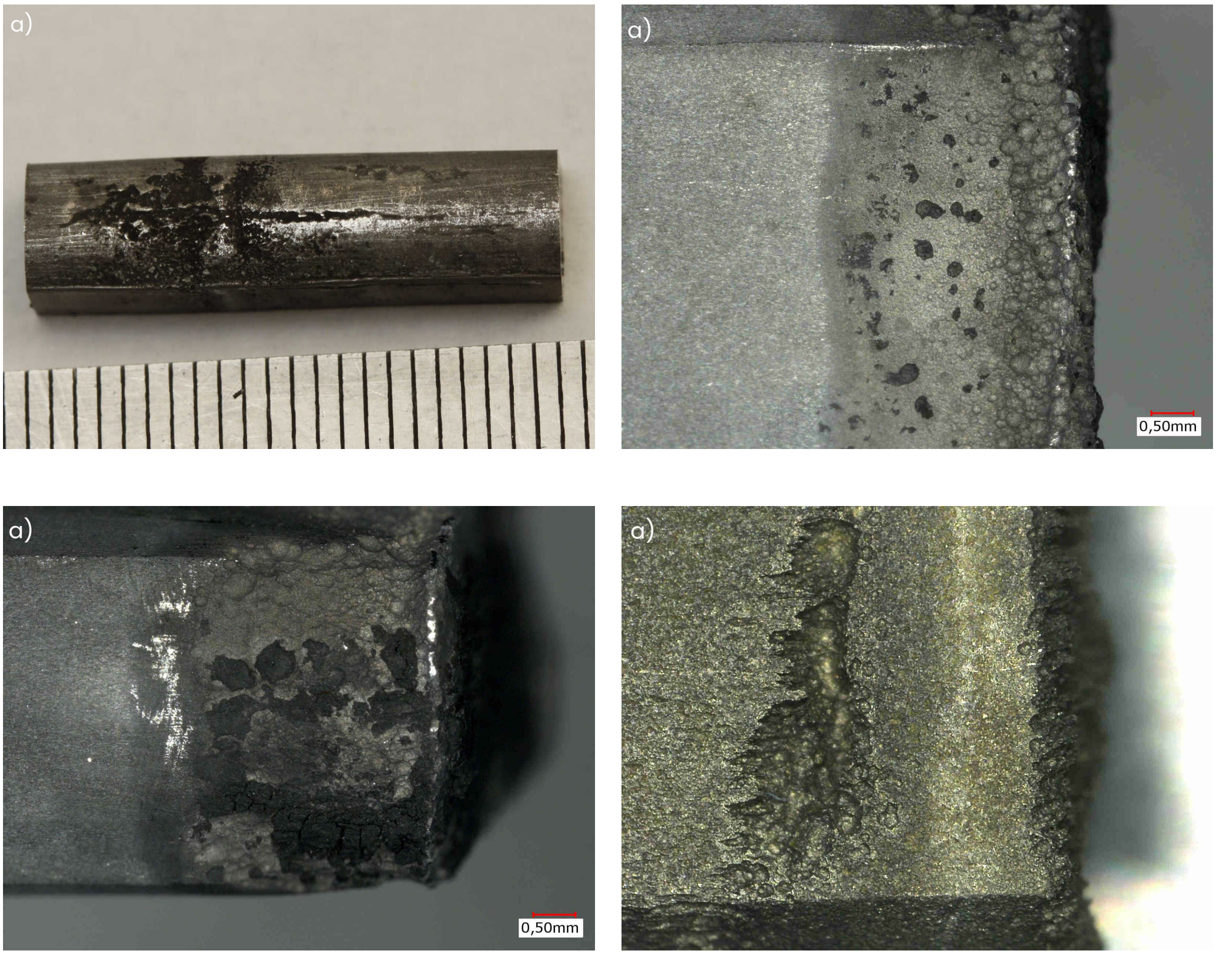

Figure 5.5: Evaluation of a typical SSC failure of a weld initiated from connected and shallow pits. a) b) c) Pits with dark corrosion product attached. d) Pits after cleaning reveal shiny etched pit bottoms.

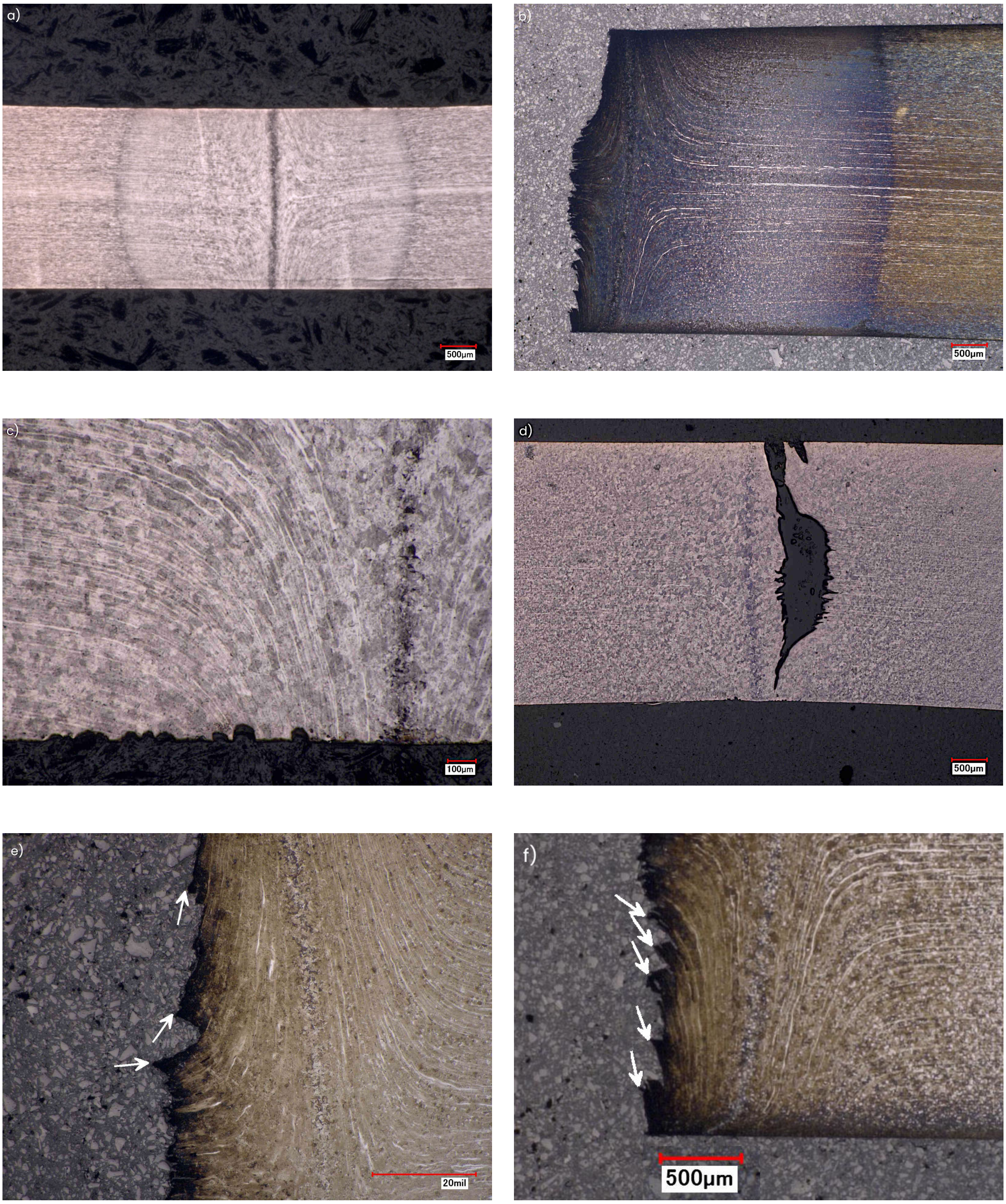

Figure 5.6: Phosphorus segregation in the upset weld revealed with Oberhoffer etch a) overview of the weld; b) weld failed to SSC; c) shallow surface pitting; d) deep surface pit without SSC; e), f) crack propagation along phosphorus segregation bands.

5.2.3 Manganese Sulphide Inclusions

Inclusions distribution was revealed by etching. As expected extrusion lines toward the wire surface in the upset zone were observed. Observations revealed that pitting near the bond line appears to be linked with non-metallic inclusions presence at the surface. When there are no inclusions the sample does not develop pitting or SSC as shown in Fig. 5.7 a), b). Whenever the inclusions are segregated toward the wire core they are extruded toward the surface in a relatively narrow zone. This can be associated with pit morphology 1 as shown in Fig. 5.7 c). Uniform distribution of MnS in the wire cross-section can be associated with pit morphology 2 as shown in Fig. 5.7 d).

The MnS inclusions do not show within the bond line. Most likely the inclusions are solubilized in the liquid steel and the majority of sulphur is discarded with the liquid from the bond line area. The remaining sulphur supersaturates the solid solution as it is unable to precipitate at high cooling speeds.

5.2.4 Weld Hardness

The bond line appears to have a relatively high resistance to corrosion. As mentioned earlier the bond line has lower carbon content due to the segregation of carbon to liquid. It is expected that the same effect occurs with manganese and silicone. It is described in the literature that manganese slightly lowers the corrosion potential of steel.

The microstructure of the bond line is a mixture of bainite and Widmanstätten ferrite. It is depleted in carbon and thus has a relatively low hardness as shown in the hardness survey in Fig. 5.8. The Widmanstätten ferrite is expected to be deleterious microstructure, the grain boundaries of large and straight ferrite grains are potential crack initiation sites. Despite that, cracks do not propagate in this zone.

Evaluation of hardness profiles reveals that the area of CGHAZ adjacent to the bond line shows local maximum in hardness $500\,\mu\mathrm{m}$ up to 1 mm from the bond line. The overall maximum hardness region is located about 30 mm from the bond line and is caused by strengthening due to recrystallization of ferrite resulting in sub-micron grain size. Overall the wire hardness decreases with increasing tempering temperature.

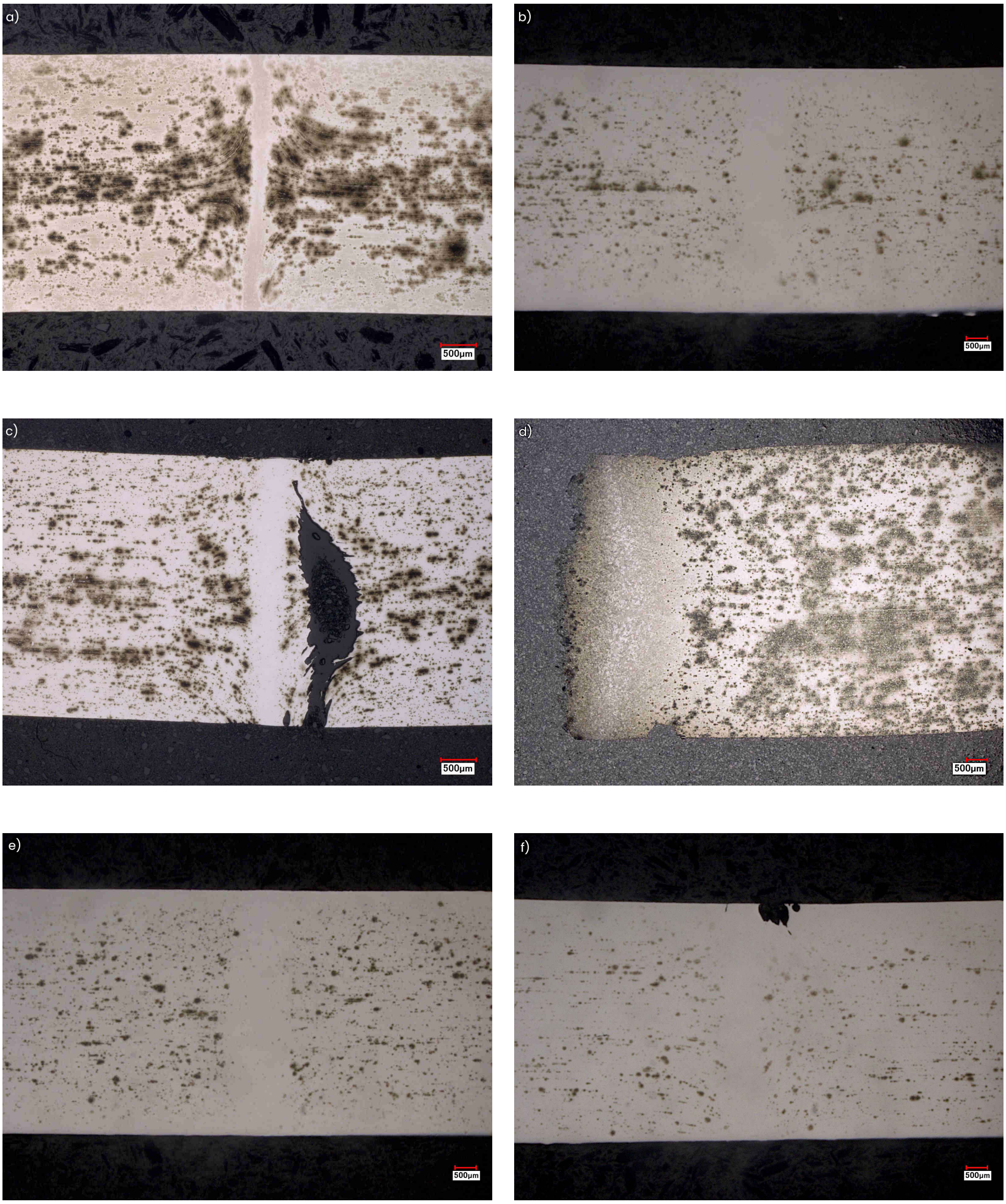

Figure 5.7: Distribution of manganese sulphide inclusions revealed by etching. a), b) distribution typical for samples not developing pitting ; c) distribution typical for an independent deep pits; d) distribution typical for a connected and shallow pitting; e), f) cases with very narrow inclusion free subsurface zone.

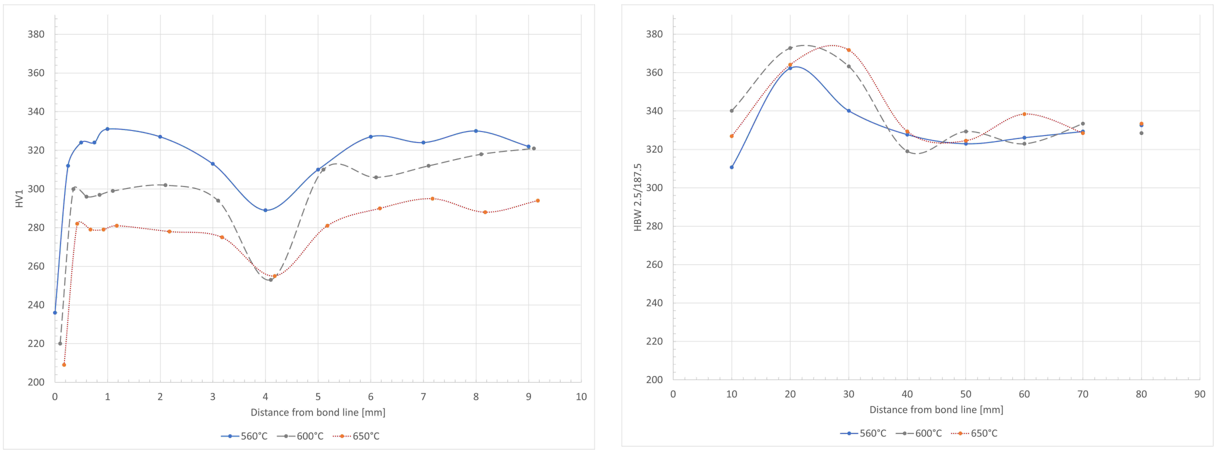

Figure 5.8: Hardness profile of the weld starting from the bond line as a function of tempering temperature.

5.2.5 Effects of PWHT Temperature on the CG HAZ Microstruture

In the experiment the wire from one batch was welded and subsequently PWHT at three temperature levels 560 °C, 600 °C and 650 °C. Samples were evaluated with SEM after electrolytic etching in alkaline potassium picrate. The microstructure consists of tempered lower bainite with traces of upper bainite and pearlite.

The heat treatment causes some spheroidization of cementite, the degree of spheroidization increases with temperature. For the highest tempering temperature, about 50% of carbides are spheroidized. The most curious thing is the cementite located at grain boundaries. It is observed that the grain boundary cementite, indicated with arrows in Fig. 5.9, forms semi-continuous networks at the tempering temperature of 560 °C, and the precipitates becomes more granular when tempered at 650 °C. Surprisingly, the grain boundary cementite is very sparse, forming fine granules at tempering temperature of 600 °C.

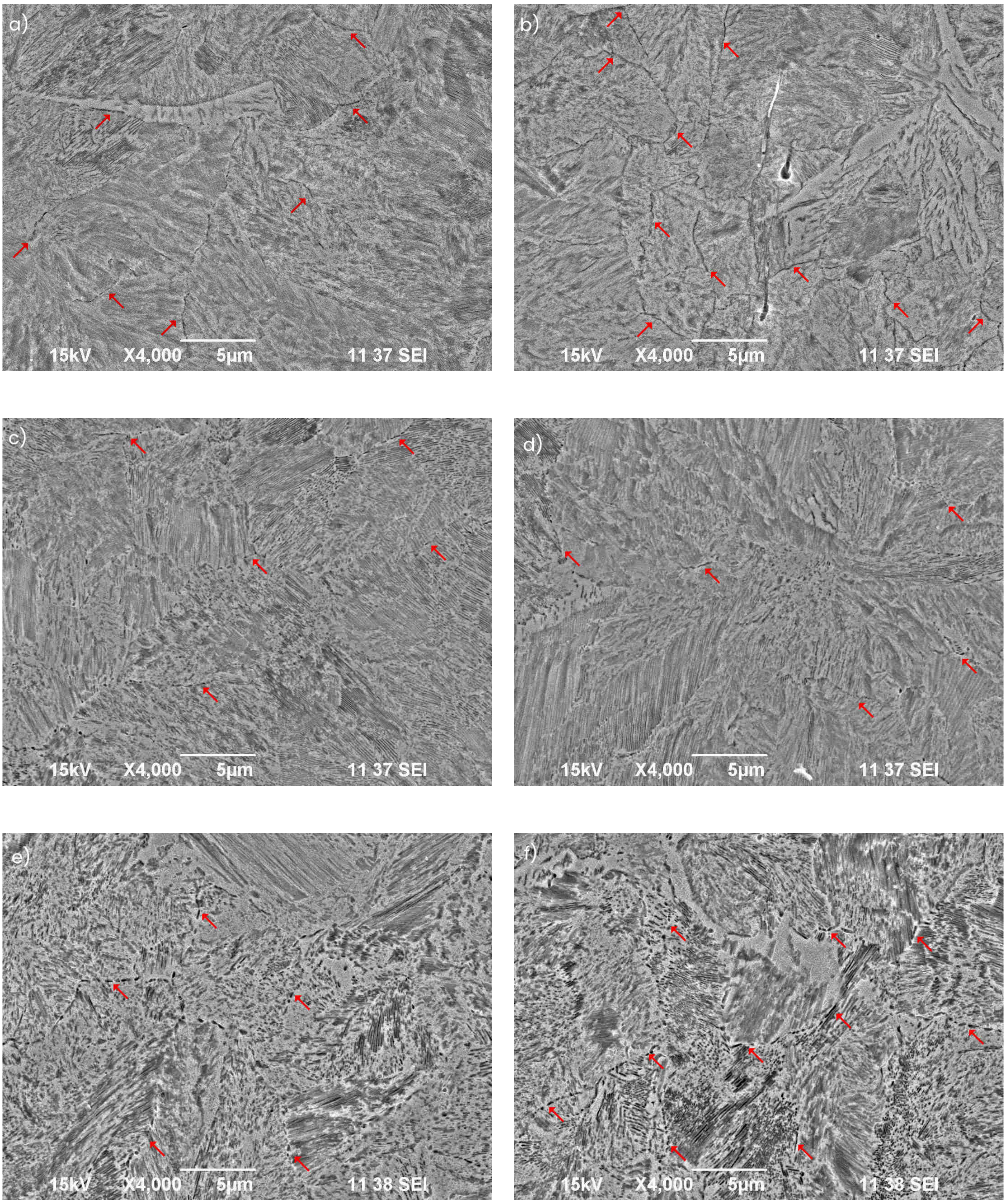

Figure 5.9: Microstructure evaluation of CG HAZ after PWHT a), b) 560 °C*; c), d)* 600 °C*; e), f)* 650 °C*. Arrows indicate grain boundary cementite.*

5.2.6 Strain Ageing

A literature review pointed toward a possible effect of strain ageing mechanism [78], and its interaction with CO_2 corrosion. It was reported that dislocation slip bands are preferentially dissolved and create a critical defects for crack initiation. After welding there may be a supersaturation with nitrogen which may cause strain ageing. To research this hypothesis an attempt to reveal the pattern of deformation during bending was made. Samples PWHT at 560 °C, 600 °C and 650 °C were used. After a month from welding the samples were cut to a rectangular cuboid, polished one of the faces, sputtered with gold and bend. After bending the sample surface was evaluated by a visual examination and SEM.

It was found that there were no difference between different tempering temperatures. Lüders band were absent. The deformation was visualized as surface roughening. Most of it localized in the bond line and CG HAZ. The surface pattern resembles a cross-hatch as shown with arrows in Fig. 5.10 The pattern does not correlate with SSC. When viewed under the SEM the prior sputtering with gold improves contrast to a sufficient level that dislocation slip bands are revealed. The slip bands at the bond line are more pronounced and longer, while in the HAZ those features are about 20 µm long. The difference can be attributed to the grain size.

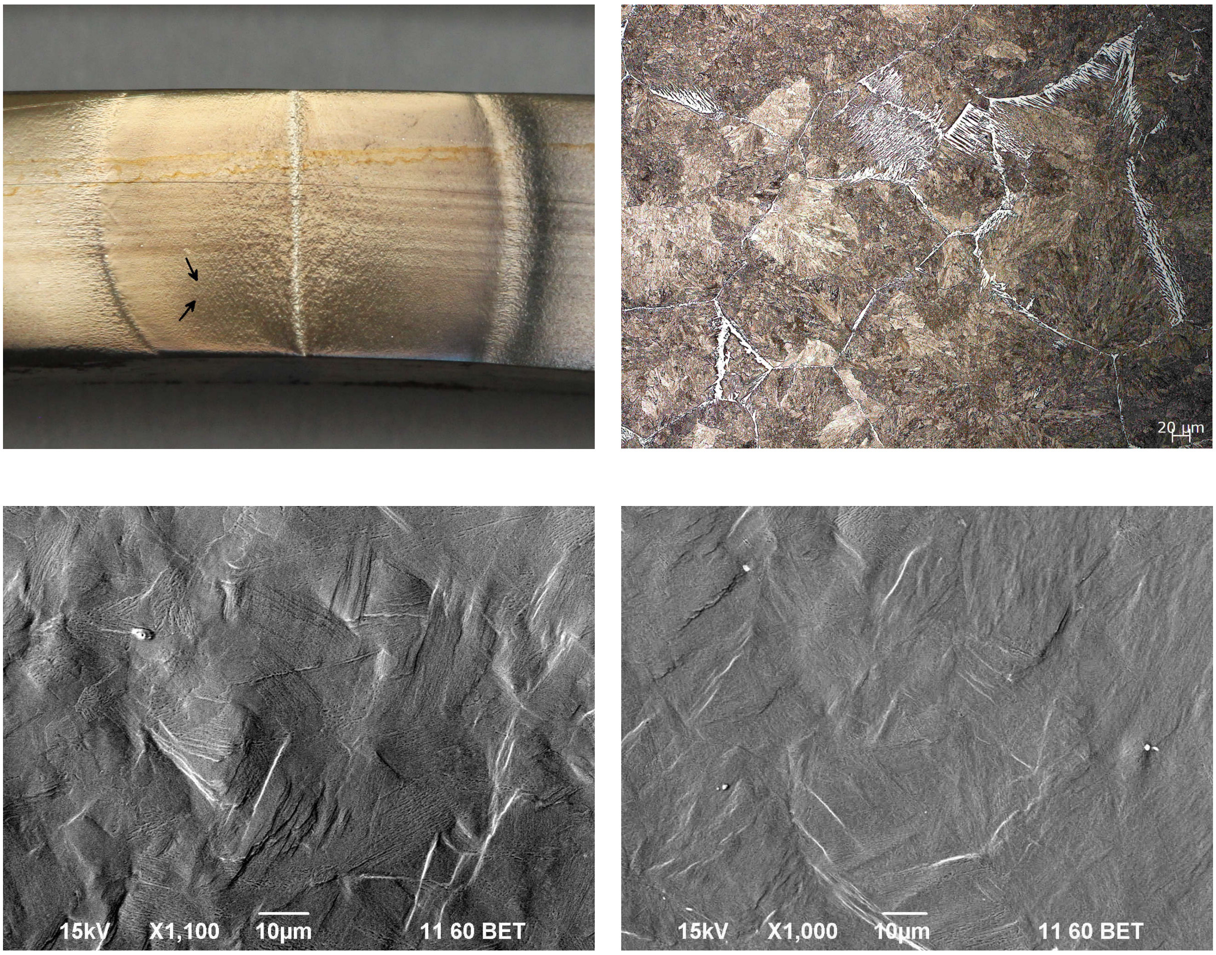

Figure 5.10: Surface roughening after deformation of the welded sample sample tempered at $560\,^{\circ}\mathrm{C}$*. Top left. Macro view ; Top right. Typical bond line microstructure; Bottom left. SEM observation of dislocation slip bands at the bond line; Bottom right. SEM observation of dislocation slip bands* $500\,\mu\mathrm{m}$ *from the bond line.*

5.3 Hydrogen Induced Cracking

5.3.1 Morphology

The HIC phenomena is typically summarized as a non-metallic inclusions problem. Anecdotally, the oversized silicate type inclusions were found near the HIC cracks, but the inclusions themselves did not develop cracking. Testing revealed that there are two typical morphologies of HIC, both located near the wire centreline.

1. In some wires, the microstructure near the centreline is heavily deformed. The grains are very flat and often unrecognizable. The HIC follows strictly this deformation and is often limited to a singular crack. The high deformed zone is more common in wires with high aspect ratio, but this is not a defining factor, as counter examples are plentiful.

2. In the other morphology type, there is a much lower localization of deformation. The grains near the centreline are elongated axially, but do not appear to be significantly flattened. HIC manifests as multiple cracks.

The comparison of the two microstructures is shown in Fig. 5.11.

5.3.2 Manganese Segregation

It was observed that a manganese segregation could be reliably revealed by etching. Surprisingly, within the wires examined some of the wires had the region of segregation offset from the centreline as much as $600\,\mu\mathrm{m}$. Those samples appeared more resistant to HIC. Microhardness survey reveals that segregation regions are significantly higher hardness 490 - 540 HV1 as compared to 405 - 460 HV1 of the surrounding microstructure, as shown in Fig. 5.12. It appears that whenever the segregation is located at the wire centreline, there is a higher deformation of the nearby microstructure directly above or below the segregation region. It was found that those areas are prone to HIC.

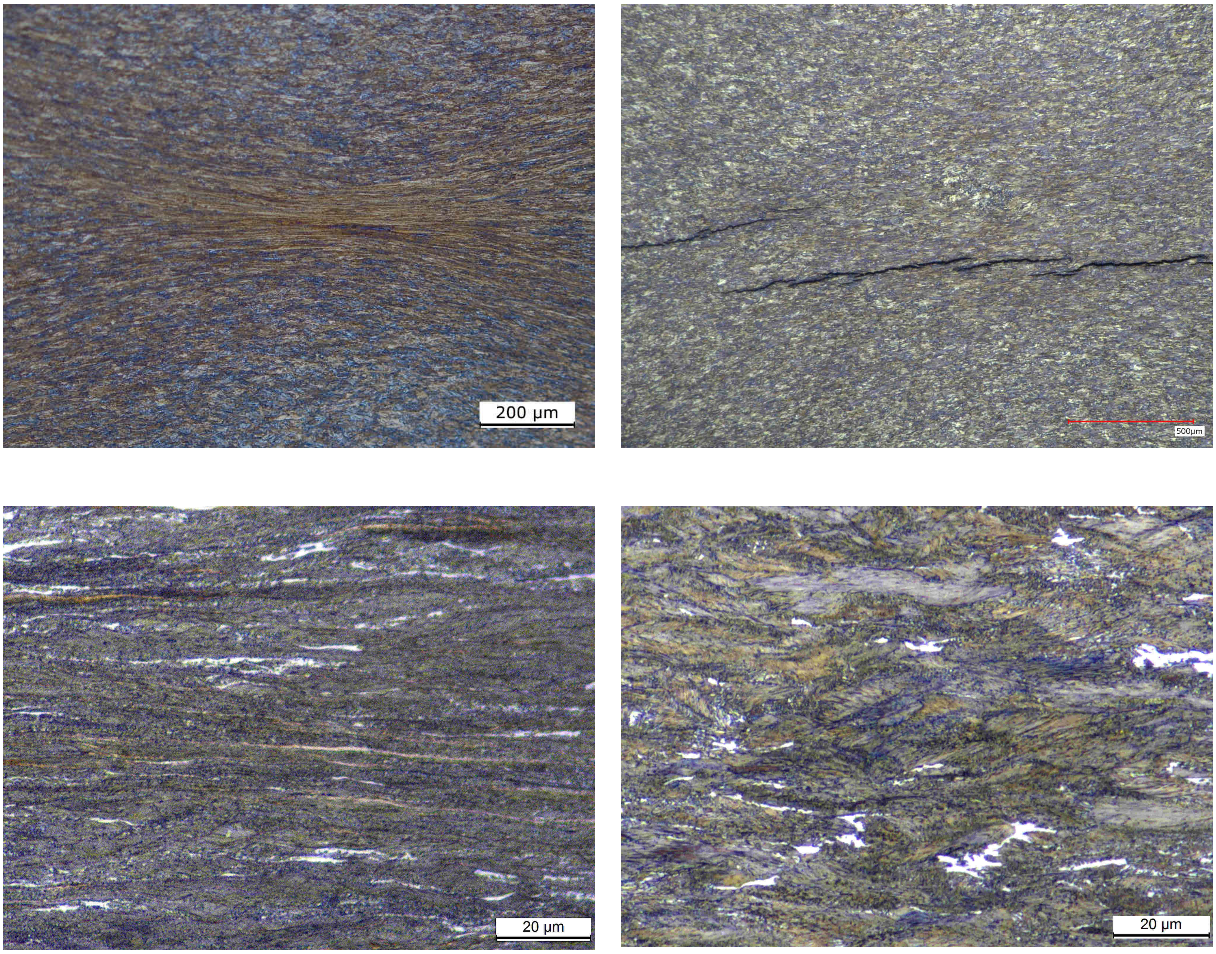

Figure 5.11: Microstructures typical for different morphologies of HIC. Left - heavy localization of plastic deformation and single crack. Right - general deformation and multiple cracks.

5.3.3 Phosphorus Segregation

It was only once observed that HIC goes through manganese segregation region, which was shown in Fig. 4.2. In the particular case, the phosphorus segregation was very localized. Cases of a more typical segregation patterns are shown in Fig. 5.13. It was found that phosphorus segregates within the wire core, and typically is not very localized. It was found that the segregation can be offset from the geometrical wire centre.

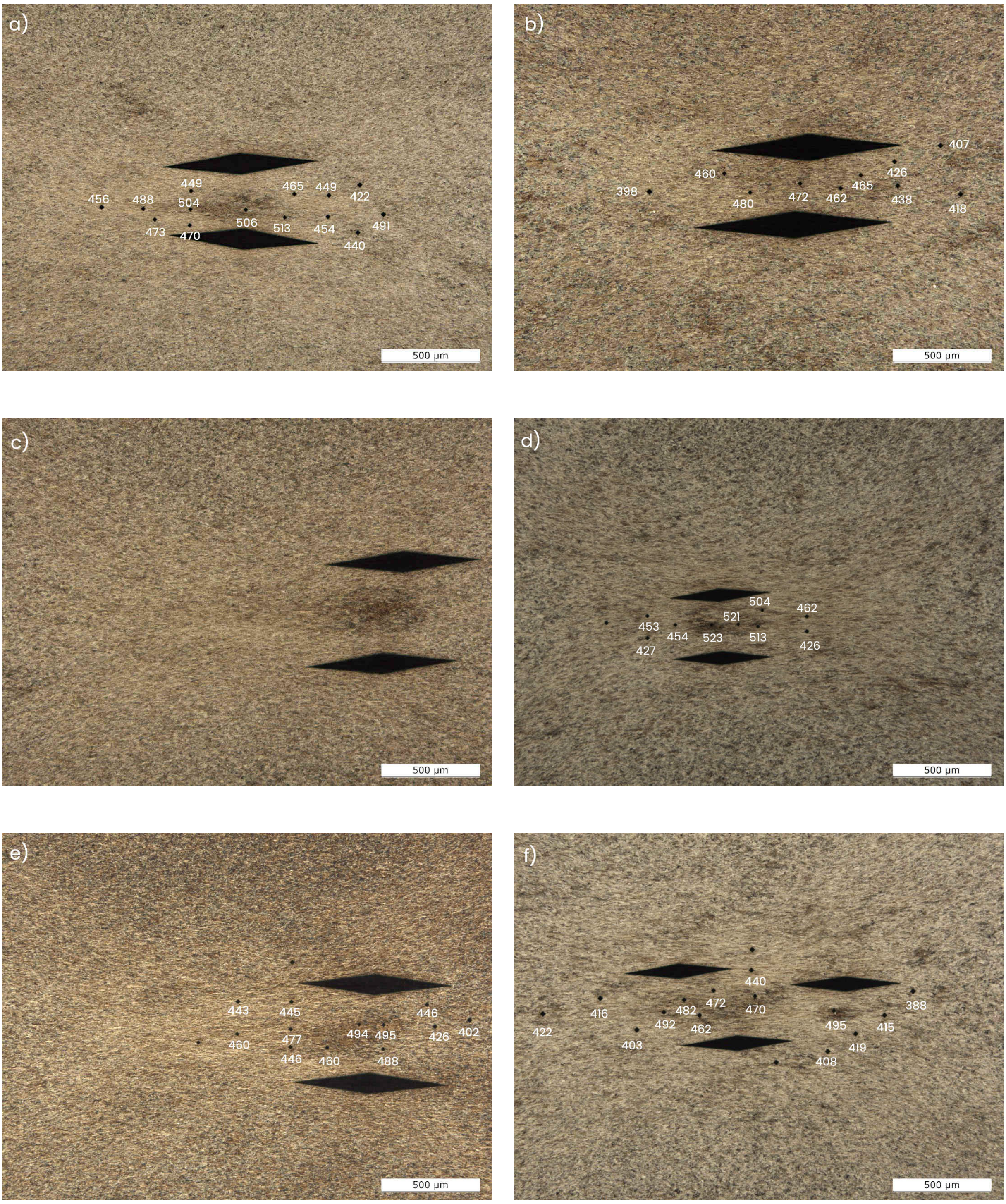

Figure 5.12: Typical centreline manganese segregation revealed by etching as dark areas. Results of a hardness survey using HV1 shown next to the respective indentation. Pictures are centred to the wire geometrical centreline to reveal offset of the manganese segregation.

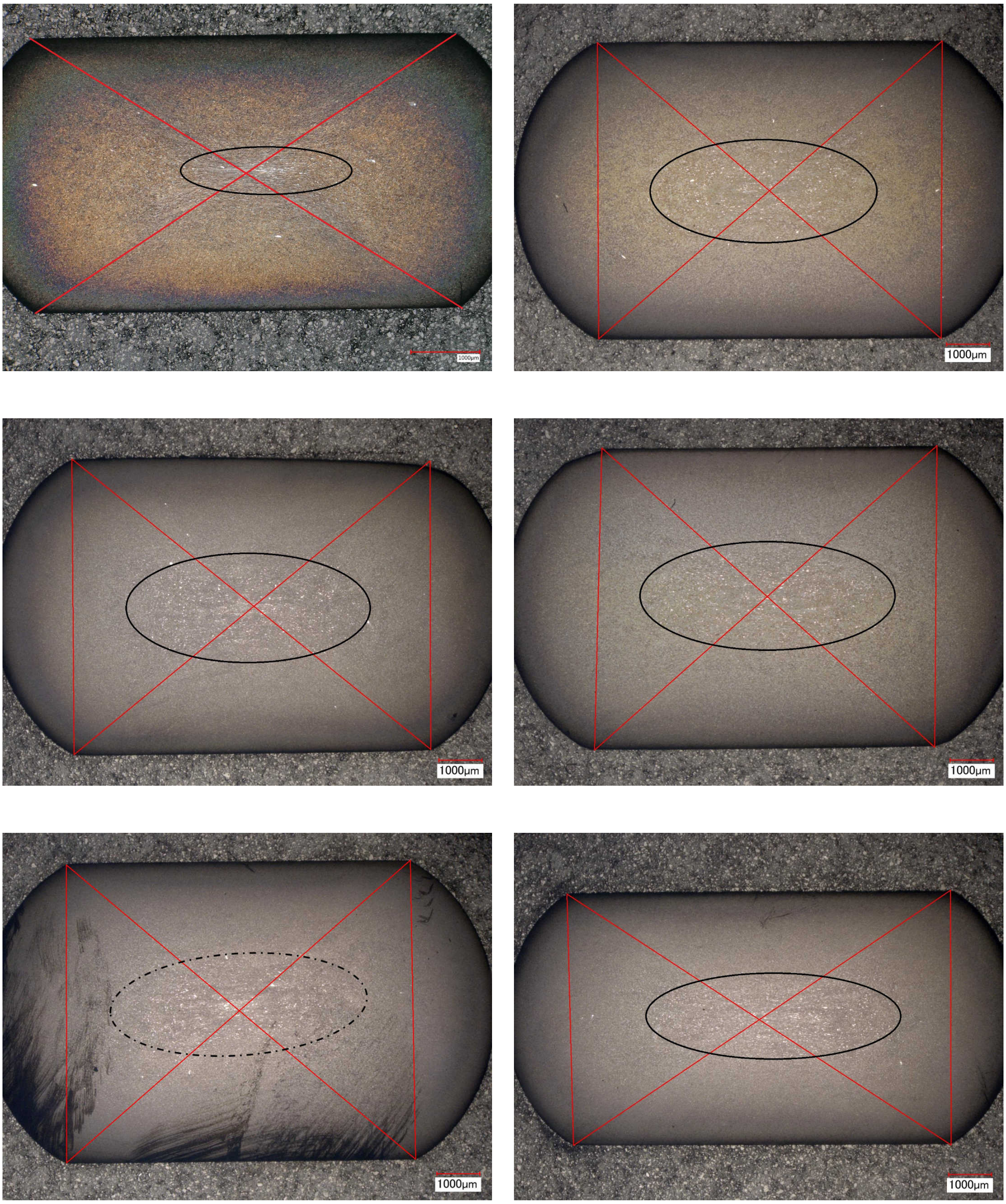

Figure 5.13: Examples of a typical centreline phosphorus segregation revealed by Oberhoffer etch. Black ellipsis outlines segregation. Red lines indicate wire centre.

5.3.4 HIC Microstructural Features Revealed by SEM

Evaluation of microstructure at higher magnification near cracking reveals that all non-metallic inclusions are delaminated. Majority of inclusions found are sub-micron size MnS inclusions. Inclusions at pearlite-pearlite grain boundaries appear stable - do not initiate cracks, as shown in Fig.5.14 a), b). Inclusions at ferrite-pearlite grain boundary seem to be the preferred HIC initiation spots, as shown in Fig. 5.14 c). The microstructure is heavily deformed. Cementite shows slip steps, buckling and fragmentation. Cementite at ferrite grain boundaries is coarser, which is interpreted as a form of ternary cementite. Microvoids formation near those coarsened carbides was observed as shown in Fig. 5.14 d).

It appears that HIC propagation occurs primarily by intergranular path, as shown inn Fig. 5.15 a). The propagation favours grain boundaries of coarser pearlite. Transgranular propagation can also occur thought regions where pearlite lamellae fragmented, as shown inn Fig. 5.15 b). In the regions of heavily localized deformation, pearlite lamellae were fragmented, plates were broken and formed microvoids, as shown in Fig. 5.15 d).

5.3.5 Influence of Anisotropy of Mechanical Properties

A mechanical property, flow resistance in principal directions, was measured using the Wheeler and Ireland technique near the wire centreline. The measurement involves Knoop hardness measured in six orientations, as presented in Fig. 5.16. The method enables construction of flow resistance surface from which a flow resistance in principal directions can be found. In the study, 16 different samples and 3 wire grades were used. MTL-5100 is marked as grade CR. The HIC severity did not show correlation with the flow resistance in Z direction, the direction perpendicular to HIC propagation. It was found that an Z/X ratio, a measure of anisotropy correlates with HIC as shown in Fig. 5.16. Based on findings it was postulated that Z/X ratio is a measure of damage accumulation within the wire centreline. It can be speculated that this damage is of the type that can be partially reversed by a heat treatment. The observation of microstructural damage can be linked to a concept critical-strain for hydrogen embrittlement [79]. The damage can be dislocation structures [80] or other non-reversible

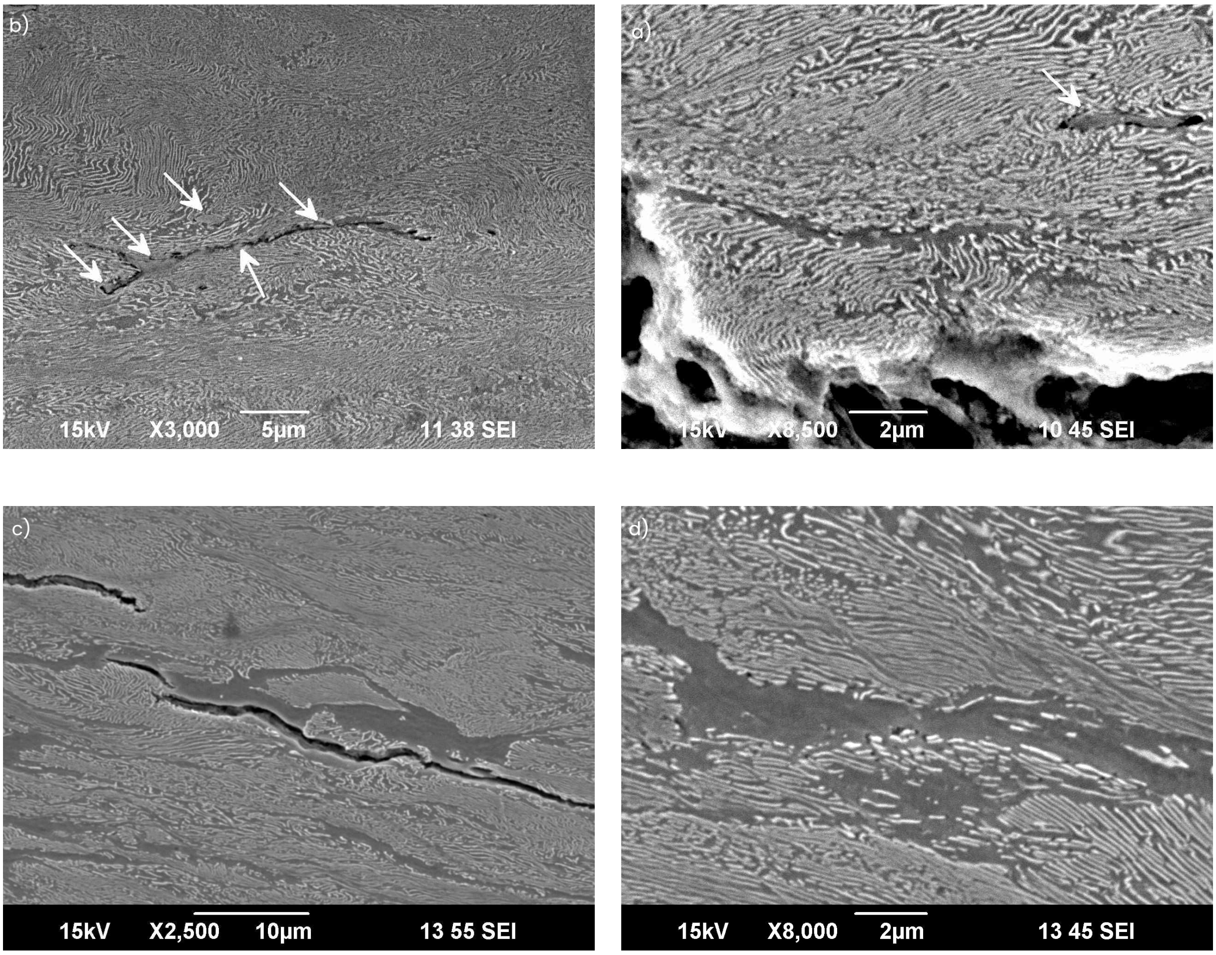

Figure 5.14: Microstructure features in transverse section near centreline observed with SEM. a) Inclusion cluster. Arrows indicate inclusions; b) Delamination around MnS inclusion; c) HIC preferential cracking path along ferrite grain boundary; d) Microvoids next to coarse cementite particles (ternary cementite).

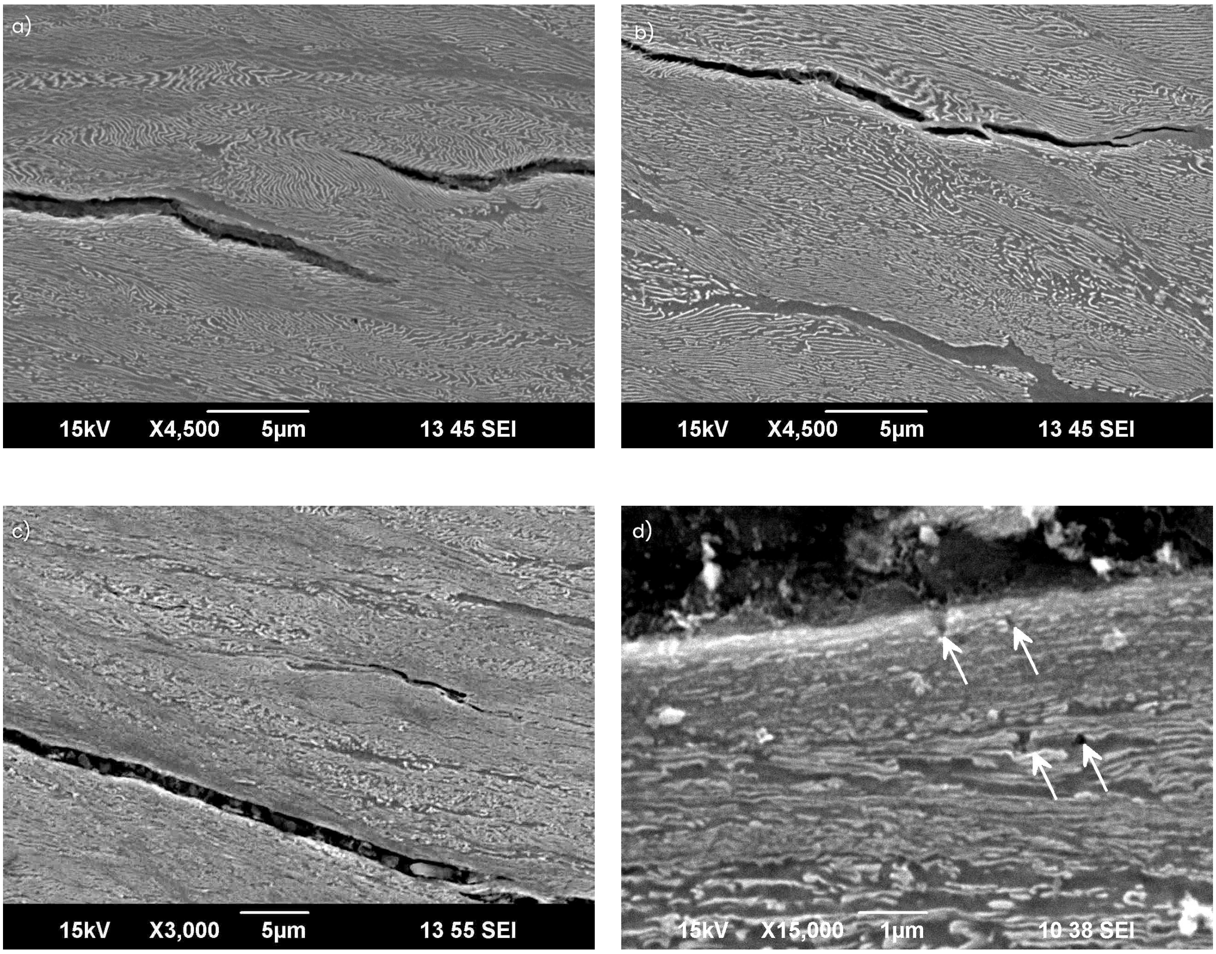

Figure 5.15: Microstructure features in transverse section near centreline observed with SEM. a) Transgranular propagation of HIC, top through pearlite fragmented at bends, bottom crack deflects from ferrite grain boundary to propagate along pearlite lamellae; b) Intergranular propagation along ferrite grain boundary and in between pearlite colonies; c) HIC through heavily deformed region; d) Deformed, fragmented and broken pearlite lamellae in heavily deformed region. Arrows point at microvoids.

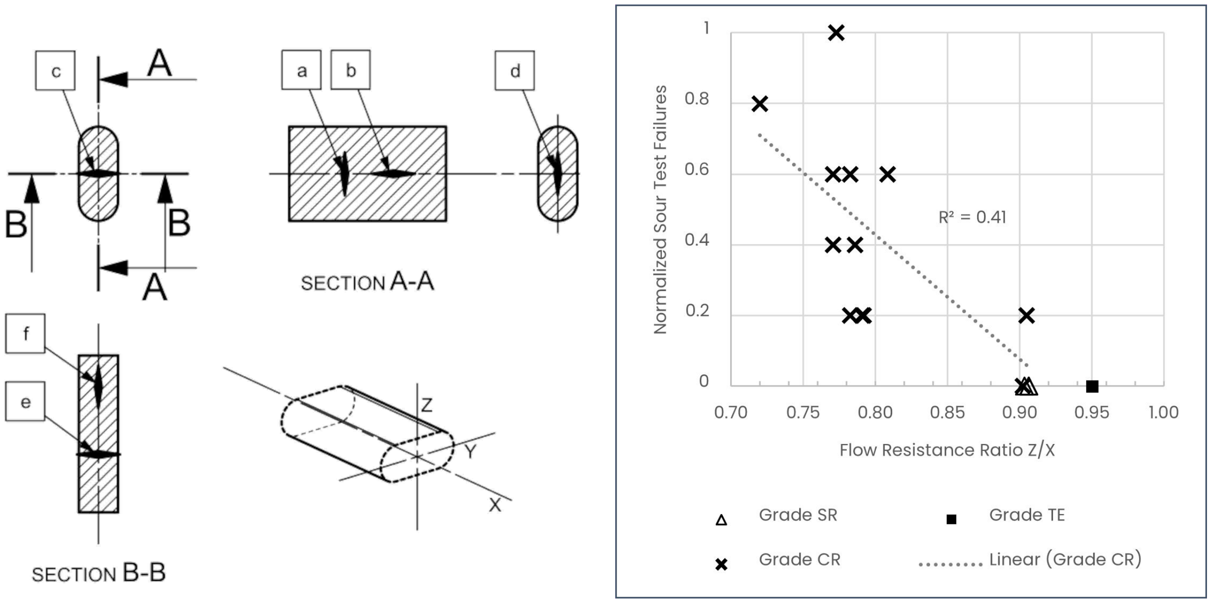

Figure 5.16: Left - wire cutting plan and orientation of Knoop indents for Wheeler and Ireland method. Right - correlation of HIC to the flow resistance anisotropy.

defects including microvoids.

Within that study there were samples E and I with high aspect ratio which developed heavy localization of deformation in the centreline. They did not show significantly different behaviour from the other samples.

6 Discussion of Microstructure Evaluation. Research Hypothesis

To summarize previous chapter observations, the following points can be made:

1. Parent SSC
    - The corrosion is a general corrosion, but localization of corrosion in form of pits can occur in any place on the sample surface,
    - Pits are typically deep and shallow,
    - It appears that decarburization plays no role,
    - It appears that the contact points to the four point bend fixture do not experience SSC. Heavy corrosion is observed in those areas, but SSC is localized in the highest stress region,
    - The SSC tends to originate from stable growth of microcracks. It appears that after a threshold value of $500\,\mu\mathrm{m}$ deep from the original surface, the crack accelerates and leads to sample failure.
2. Weld SSC
    - The bond line is more corrosion resistant than the surrounding CG HAZ,
    - The bond line microstructure consists of bainite and Widmanstätten ferrite. Despite theoretically being a SSC susceptible microstructure no cracks were found there,
    - The SSC is found about $500\,\mu\mathrm{m}$ to $1000\,\mu\mathrm{m}$ from the bond line,
    - The pitting next to the bond line is correlated with MnS inclusions extruded to the surface in the upsetting process. There is no correlation with phosphorus segregation,

- There are two morphologies of pits: shallow and connected or deep and disjoined,
- The depth limit for a stable pit or microcrack is $500\,\mu\mathrm{m}$. However, occasionally SSC does not occur and pit growth can lead to sample failure,
- The cracking preferred path is through phosphorus segregated regions,
- MnS inclusions distributed such that the subsurface region of at leats 1/4 thickness is virtually free from inclusions and the inclusions are evenly distributed through the wire core has improved weld SSC resistance,
- It was shown that the tempering temperature affects not only hardness, but also grain boundary carbides morphology. Increase of the tempering temperature to $600\,^{\circ}\mathrm{C}$ produced the most desirable microstructure,
- It was shown that strain ageing of welds does not manifest. Deformation during bending within the weld localizes to the bond line and CG HAZ. The slip band pattern size reflects the grain size and does not seem to correspond with SSC.

3. HIC

   - Whenever the centre of segregation is offset from the geometrical centre of the wire, it appears that the wire has lower HIC susceptibility. HIC correlates with segregation of manganese and extreme cases of phosphorus segregation,
   - Heavy localization of deformation within the wire centreline occurs for some wires and not others. Is more common in high aspect ratio wires, but not completely determined by the geometry,
   - HIC originates from inclusions located at ferrite - pearlite grain boundaries. After the crack initiation, the intergranular path is preferred. Transgranular path is possible especially in areas where pearlite is aligned with the crack propagation direction or in grains where pearlite lamellae are segmented or broken,
   - It was observed that pearlite lamellae of grains neighbouring ferrite are coarsened. It is interpreted as a form of ternary cementite precipitation.

Evidence of micro-void formation next to coarsened cementite is found,

- In heavily deformed pearlite the cementite lamellae partially dissolve, fragment or break. Formation of micro-voids was found at broken lamellae.
- It was found that the flow resistance anisotropy can be a measure of microstructural damage from cold rolling.
- The microstructural damage is, at least partially, of the type that can be reversed by a heat treatment.

Neither of the observations mentioned gives a definitive answer regards to whether or not the wire sample will fail in testing. To progress an attempt to do a full characterization of samples including:

- Ferrite content and morphology,
- Sulphur content and MnS distribution,
- Manganese segregation region hardness,
- Phosphorus segregation distribution,
- Anisotropy of mechanical properties.

and building a predictive model can be done. Due to labour intensiveness, that approach is not practical. There are indications for HIC and weld SSC, but so far no indications of SSC susceptibility were found. There may be other factors than listed that affect the test result. Those microstructural features should all be related to the wire chemical composition. That leads to the research hypothesis. The following, opposing hypotheses can be formulated.

H_0: There is no influence of the chemical composition on the sour service test outcome. The variation of the chemical composition within the specification is too small to significantly affect the wire properties and microstructure. The material performance is inherently inadequate for the sour service test environment.

and

H_1: The chemical composition affects the microstructure and determines the test outcome. The material performance can be improved by chemical composition changes, within the specified range, to reliably pass sour service tests.

7 Statistical Data Analysis

The input for the analysis was assembled from material certificates and batch test reports. Documentation was digitized into an Excel spreadsheet. The approach was that all information could be relevant and should be put into the database. Overall, the dataset consisted of 1164 sour service test, 4559 individual samples from 500 unique steel casts. The overlap was due to retests, simultaneous tests at different conditions, or sporadically requirements to test the first and the last coil from the batch. Among others the following information was collected:

- Wire characteristic: size, manufacturer, condition: parent or welded, weld tempering parameters,
- Mechanical properties: YS, UTS, elongation, hardness of the parent material,
- Chemical composition consisting of up to 17 elements, as certificates reported more than required by the specification,
- Sour test parameters: pH, H_2S partial pressure,
- Sour test result: number of samples failing, number of samples tested, mechanism of failure.
- Details like steel rod supplier, laboratory, comments on test abnormalities e.g. pitting, oversized inclusions.

Over 30 parameters could be considered in the model.

7.1 Assumptions

7.1.1 Effect of Sample Volume

It was observed in internal company statistical analyses that the failure rate increases with the increasing wire size. The increase was non-linear. To be able to reduce the dimensionality and remove the wire size as a factor, the following assumption was made.

A$_1$: Within the wire there are multiple microstructural defects, sites where the cracking (SSC or HIC) can initiate. Each defect can be characterized by a critical hydrogen amount [N$_\mathrm{C}$] for crack initiation. The [N$_\mathrm{C}$] has a Weibull distribution.

The Weibull distribution model is used in Materials Science to describe for example brittle failure of ceramics and fatigue phenomena. It was also shown that time to failure by hydrogen embrittlement adheres to Weibull distribution [81]. By this assumption, the probability P of single sample failure of volume V is given as (7.1)

$$P = 1 - \{\exp(\frac{H_i - Hu}{H_0})^m\}^{\frac{V}{V_0}} \tag{7.1}$$

where H_i is an environment aggressiveness index, H_u is a threshold environment aggressiveness, H_0 is a scale factor, m is a Weibull modulus. The term (7.2) can be interpreted as a survival probability of a sample with a volume V_0.

$$\exp(\frac{H_i - Hu}{H_0})^m = P_{V_0} \tag{7.2}$$

This work will focus on a Normalized Failure Probability defined as (7.3)

$$NFP = 1 - P_{V_0} \tag{7.3}$$

A$_2$: The Normalized Failure Probability (NFP) is a **material constant** for a given chemical composition and test parameters, regardless of the wire size or sample volume.

7.1.2 Test Results and NFP Evaluation

The probability of an actual test result where k samples fail out of n samples tested is given by the Bernoulli distribution (7.4):

$$P_{(n,k)} = \frac{n!}{k!(n-k)!} \cdot (NFP^{\frac{V}{V_0}})^k \cdot (1 - NFP^{\frac{V}{V_0}})^{n-k} \tag{7.4}$$

The test result is probabilistic, thus the next assumption about NFP estimation is required.

A$_3$: The Normalized Failure Probability (NFP) can be evaluated based on the actual test result by maximum likelihood estimation (MLE).

The test result is a counting variable approximating a continuos variable. For $n = 3$ the observed test results can assume four values $(0, \frac{1}{3}, \frac{2}{3}, 1)$. To accurately distinguish wires by performance, it is desired to have an accurate estimation of NFP. It can be easily shown from (7.4) that for 1% global failure rate based on at least four out of five samples passing the test the corresponding NFP is .033. The Monte Carlo analysis where the sample failure was modelled with NFP shows a distribution of test results as shown in Fig. 7.1. For NFP = .033 the most likely estimation is zero up to $n = 34$, above which the NFP estimator becomes $\widehat{NFP} = \frac{1}{35} = .029$.

A$_5$: The resolution of NFP evaluation is sufficient for comparison of wire performance when it is based on at least 35 samples ($n \geq 35$).

7.1.3 Comments on Assumptions

Traditionally, it is taken as granted that there is a threshold environment aggressiveness below which the SSC does not occur. This view is a basis for fit for purpose material selection, as reinforced by international standards.

It appears that the assumptions, so far, discard this view and replace it with a probabilistic theory of failure. The equation (7.1) introduced Weibull distribution parameters H_i, H_u, H_0, m. Estimating those parameters is beyond the scope of this work. It would require an experimental design approach as described in EN 843-5 [82]. When plotted with arbitrary parameters, the probability of failure of a single sample as a function of H_i - the environment aggressiveness, has a shape shown in Fig. 7.2. The threshold value is a feature of the three parameter Weibull distribution function, and the assumptions provide for a stochastic description of failures in the transition zone between certain pass and certain failure.

It should be noted that the assumption A_5 refers to the number of samples with volume V_0. When the actual volume of samples changes, the apparent probability of failure changes as well. The sensitivity of the test is constant when the test volume is equivalent to $35 \cdot V_0$. The estimators will be different values, because NFP is a counting

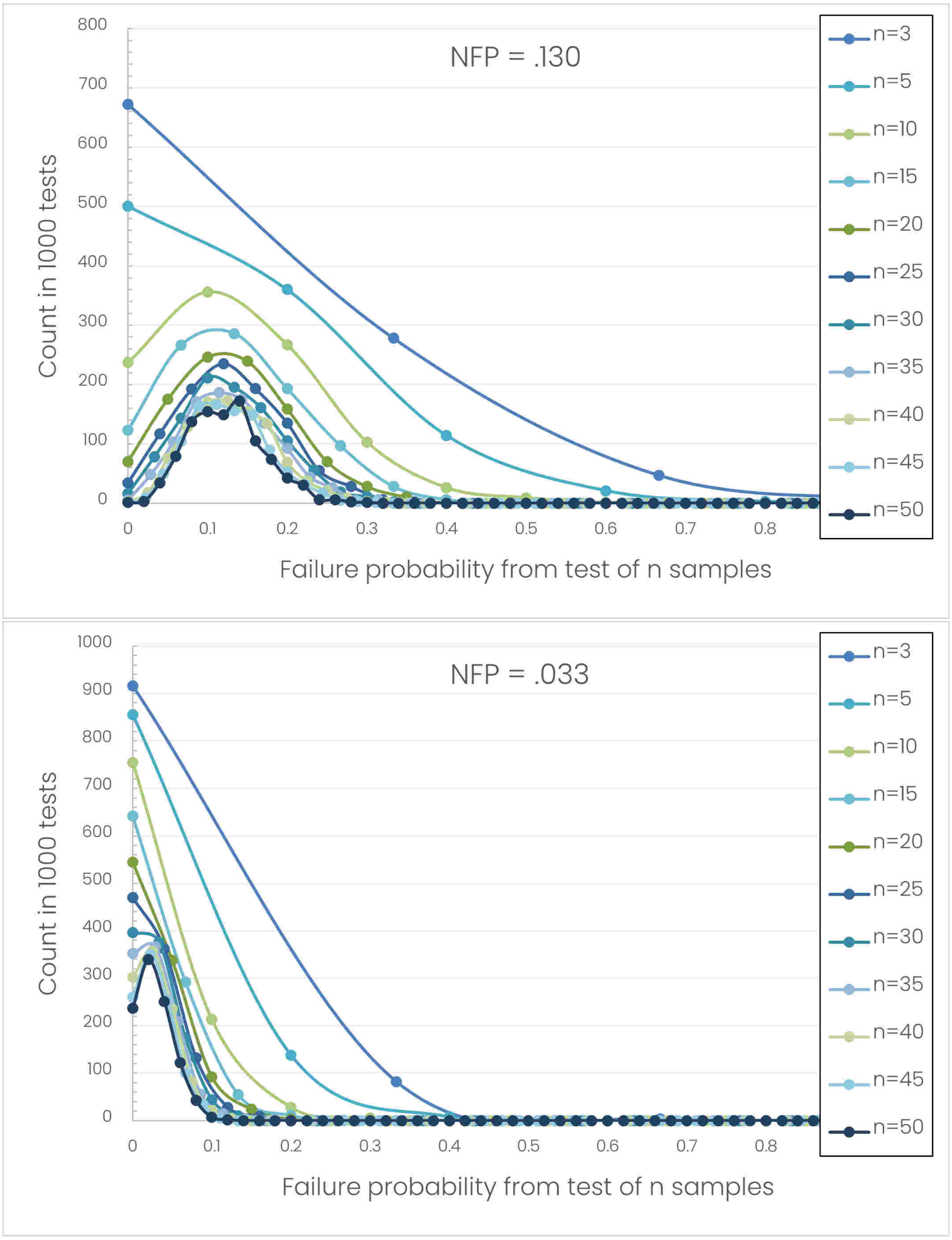

Figure 7.1: Monte Carlo analysis indicating the distribution of observed $\widehat{NFP}$ *in the test based on number of samples tested and NFP. a) for NFP=.130 corresponding to 12.9% global failure rate; b) for NFP=.033 corresponding to a global failure rate of 1%.*

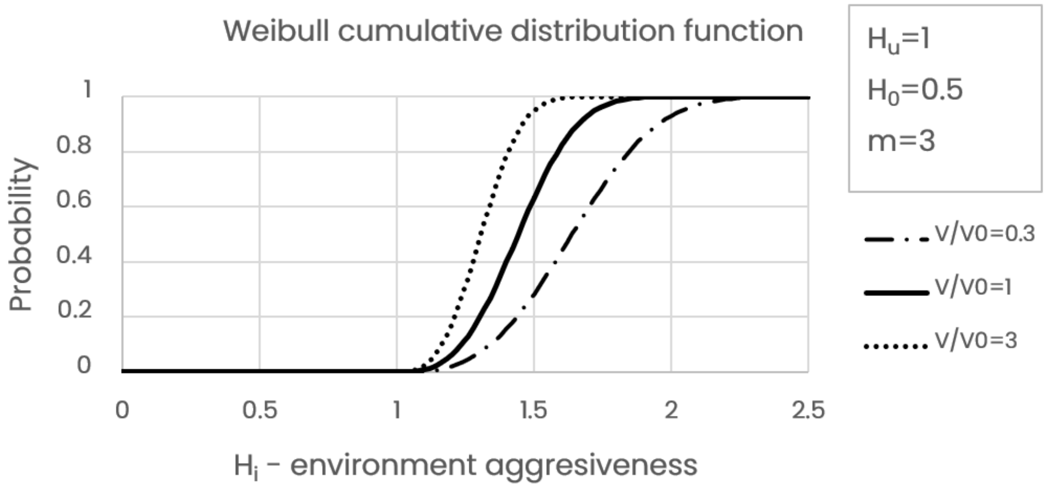

Figure 7.2: Weibull distribution based on arbitrary parameters and sample volumes

type variable.

Whenever there are i sizes of the wire with their corresponding V_i within the the same category the $\widehat{NFP}$ for that category becomes a samples volume weighted average:

$$\widehat{NFP} = 1 - \frac{\sum_1^i (n_i \cdot V_i \cdot \exp(1 - \frac{k_i}{n_i})^{\frac{V_0}{V_i}})}{\sum_1^i (n_i \cdot V_i)} \tag{7.5}$$

7.2 Methodology

7.2.1 Binning by Wire Shape, Condition and Failure Mechanism

The initial review of the data indicated that the wires of aspect ratio of 2 and lower, which includes profiles like 8x4, 10x5, 12x6 and 12x7, should be separated from high aspect wires. Low aspect wires fail by all three mechanisms while high aspect wires fail to HIC at double the rate. For high aspect wires tempering received by welded wires does not decrease the HIC occurrence, as shown in Table 7.2. High aspect ratio wires fail to weld SSC, followed by HIC and parent SCC as summarized in Table 7.1. Relatively small amount of high aspect ratio wires was tested, and the failure pattern could have multiple interpretations. To address those issue this group of wires was excluded from the dataset.

Table 7.1: NFP for wires with aspect ratio ≤ 2 *by the failure mechanism and wire condition.*

Wire condition	HIC	SSC	Pitting
Welded	.024	.068	.065
Parent	.061	.020	.014

Table 7.2: NFP for wires with aspect ratio > 2 *by the failure mechanism and wire condition.*

Wire condition	HIC	SSC	Pitting
Welded	.108	0	0
Parent	.126	0	0

7.2.2 Test Environment Aggressiveness Map

The test conditions are described by two parameters: pH and H_2S partial pressure. It should be possible to reduce those two to one parameter. Environment agressivenes for SSC should correlate to hydrogen flux. Based on the equations (3.3) and (3.4) it can be quantified as:

$$A = [H^+] \cdot [H_2S] = e^{-pH} \cdot [H_2S] \tag{7.6}$$

Maps presenting pH, H_2S concentration and NFP were prepared as shown in Fig. 7.3, 7.4 and 7.5 for HIC, weld SSC and parent SSC, respectively. The expected behaviour is for the environment is: the highest NFP toward the bottom right corner and the lowest NFP toward the top left corner. The environments along the the other diagonal should be equivalent in agressiveness. It is quite surprising that the NFP increases with increasing H_2S partial pressure only at pH $\leq$ 4.4. This region is delineated with yellow and green on the maps. Above pH 4.4 the failure rate appears to be almost constant whenever the H_2S partial pressure is lower than 1 mbar. This region is marked in orange. The other surprise is a region of pH > 4.4 and H_2S higher than 1 mbar where no failures occurred. This region is marked in blue. Above pH 5.4 no parent SSC

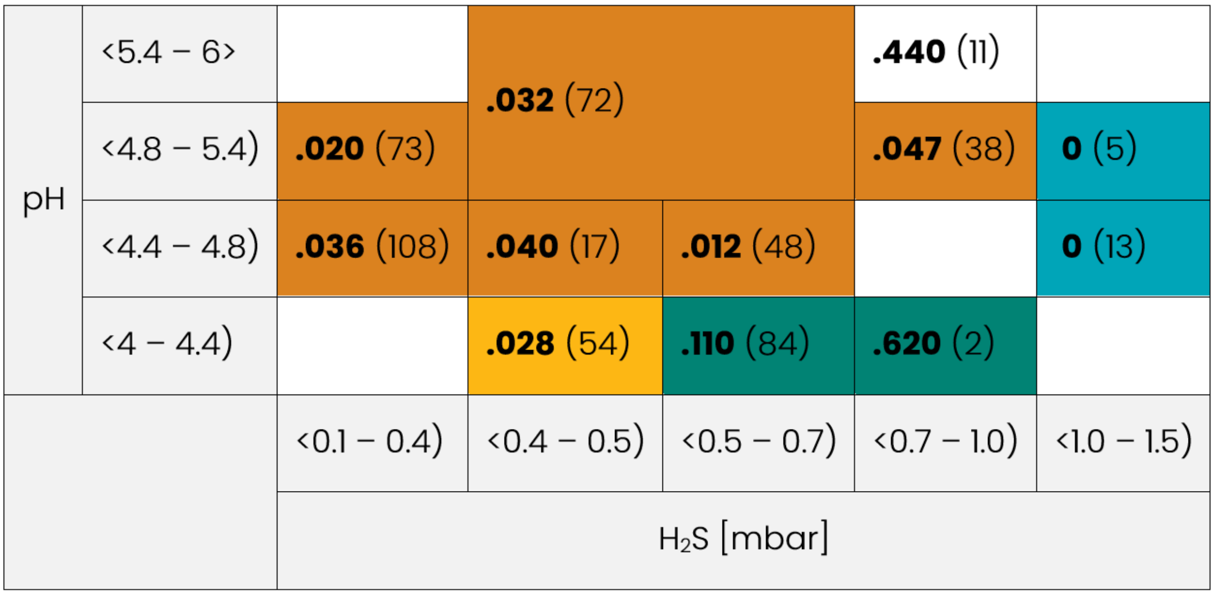

pH	<0.1 – 0.4)	<0.4 – 0.5)	<0.5 – 0.7)	<0.7 – 1.0)	<1.0 – 1.5)
<5.4 – 6>		**.032** (72)		**.440** (11)	
<4.8 – 5.4)	**.020** (73)			**.047** (38)	**0** (5)
<4.4 – 4.8)	**.036** (108)	**.040** (17)	**.012** (48)		**0** (13)
<4 – 4.4)		**.028** (54)	**.110** (84)	**.620** (2)	
	H_2S [mbar]				

Figure 7.3: Map of failure rate by HIC as a function of pH and H_2S partial pressure. The bold number indicates NFP. The number in parenthesis indicates number of samples.

failures occurred. The environment aggressiveness areas are shared by all three failure mechanisms. This allows for further reduction of the model dimensionality. The environment aggressiveness can be represented by thee bins:

- Region of **M**ild acidity (**M**) $4.4 < \text{pH} < 6.0$ and $H_2S < 1$ mbar [orange region]
- Region of high **A**cidity and extra **L**ow H_2S (**AL**) $\text{pH} < 4.4$ and $H_2S \leq 0.5$ mbar [yellow region]
- Region of high **A**cidity and low **S**our (**AS**) $\text{pH} < 4.4$ and $H_2S > 0.5$ mbar [green region]

The data in the last bin with $H_2S \leq 1$ mbar or $\text{pH} > 6$ will be excluded from the analysis.

To summarize the initial binning reduced the dimensionality of the problem to nine categories summarized in Table 7.3.

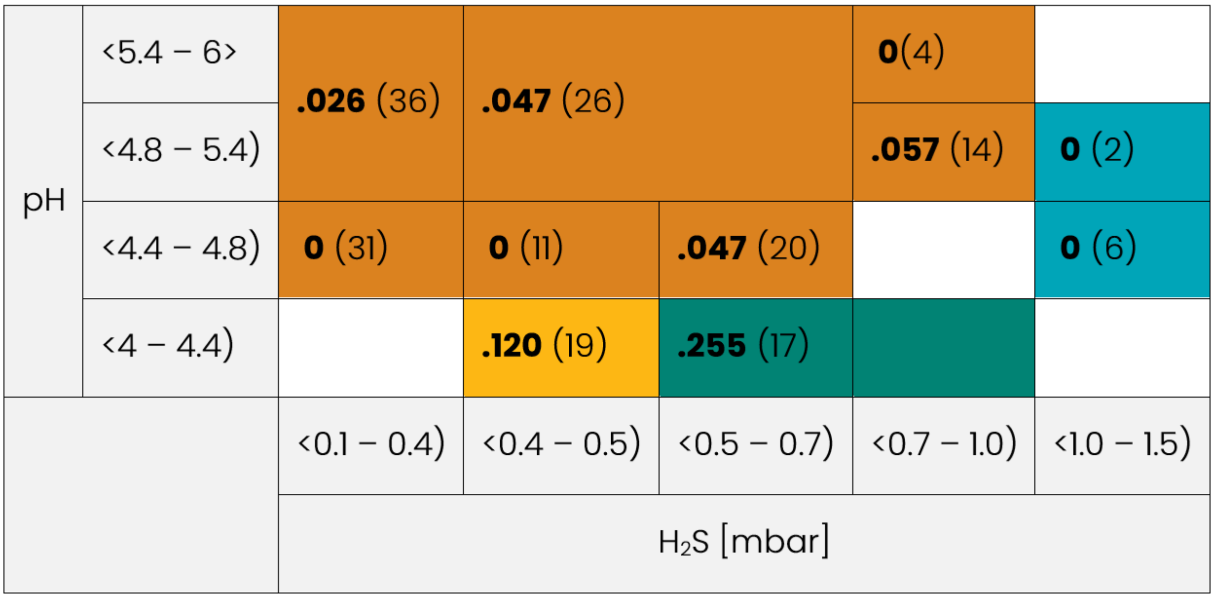

pH	<5.4 – 6>	**.026** (36)	**.047** (26)		**0**(4)	
	<4.8 – 5.4)				**.057** (14)	**0** (2)
	<4.4 – 4.8)	**0** (31)	**0** (11)	**.047** (20)		**0** (6)
	<4 – 4.4)		**.120** (19)	**.255** (17)		
		<0.1 – 0.4)	<0.4 – 0.5)	<0.5 – 0.7)	<0.7 – 1.0)	<1.0 – 1.5)
		H_2S [mbar]				

Figure 7.4: Map of failure rate by SSC of weld as a function of pH and H_2S partial pressure. The bold number indicates NFP. The number in parenthesis indicates number of samples.

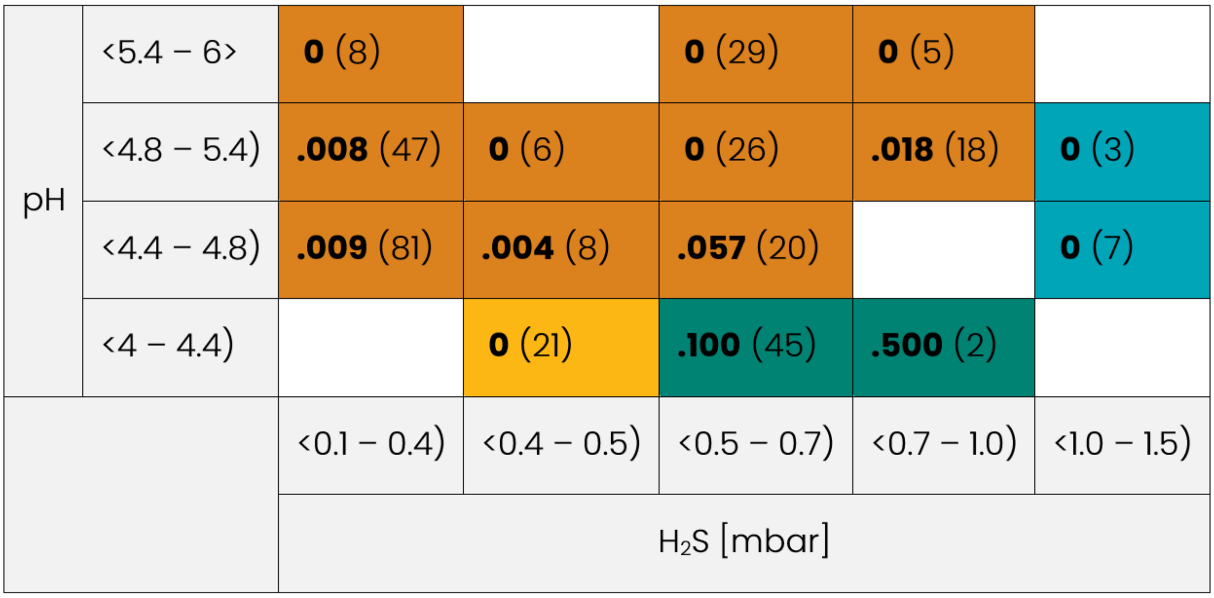

pH	<5.4 – 6>	**0** (8)		**0** (29)	**0** (5)	
	<4.8 – 5.4)	**.008** (47)	**0** (6)	**0** (26)	**.018** (18)	**0** (3)
	<4.4 – 4.8)	**.009** (81)	**.004** (8)	**.057** (20)		**0** (7)
	<4 – 4.4)		**0** (21)	**.100** (45)	**.500** (2)	
		<0.1 – 0.4)	<0.4 – 0.5)	<0.5 – 0.7)	<0.7 – 1.0)	<1.0 – 1.5)
		H_2S [mbar]				

Figure 7.5: Map of failure rate by SSC of parent wire as a function of pH and H_2S partial pressure. The bold number indicates NFP. The number in parenthesis indicates number of samples.

Table 7.3: Summary of binning and bin labels

Environment	HIC Parent	SSC Parent	SSC Weld
high Acidity, extra Low H_2S	ALP	ALP	ALW
high Acidity, low Sour	HIC	ASP	ASW
Mild acidity	MP	MP	MW

7.3 Verification of Assumptions

To verify the assumption that the Weibull distribution model can be used to normalize failure probability over different wire sizes additional check was prepared. The NFP attributed to the wire size were analysed as a function of supplier or environment. As shown in Table 7.4 the NFP is quite uniform between different wire sizes in environment M and between different supplies, with the exception of wires from Supplier 1. Data for Supplier 1 were removed from further analysis, as non-conforming to the model.

In the Table 7.5 the NFP distribution between different bins is presented. It appears that the NFP is uniform within environment and wire condition bin with the exception of results for two wire sizes as indicated in orange. Despite this discrepancy this results are kept in the model.

Table 7.4: Partial NFP contributing to average NFP by wire size as a function of wire supplier. The NFP presented are a sum of HIC, parent SSC and weld SSC in environment M. Analysis shows a good consistency with the exception of Supplier 1.

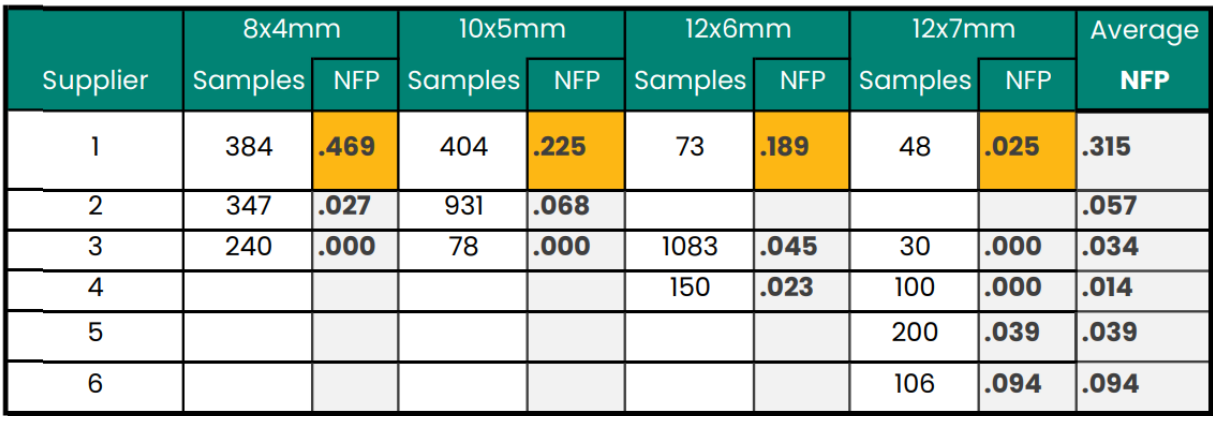

	8x4mm		10x5mm		12x6mm		12x7mm		Average
Supplier	Samples	NFP	Samples	NFP	Samples	NFP	Samples	NFP	**NFP**
1	384	**.469**	404	**.225**	73	**.189**	48	**.025**	**.315**
2	347	**.027**	931	**.068**					**.057**
3	240	**.000**	78	**.000**	1083	**.045**	30	**.000**	**.034**
4					150	**.023**	100	**.000**	**.014**
5							200	**.039**	**.039**
6							106	**.094**	**.094**

Table 7.5: Partial NFP contributing to avearage NFP by wire size. Analysis shows good consistency with the exception of 10x5 wire which shows elevated NFP of HIC in environment M, and 12x6 wire resistance to weld SSC in environment AS.

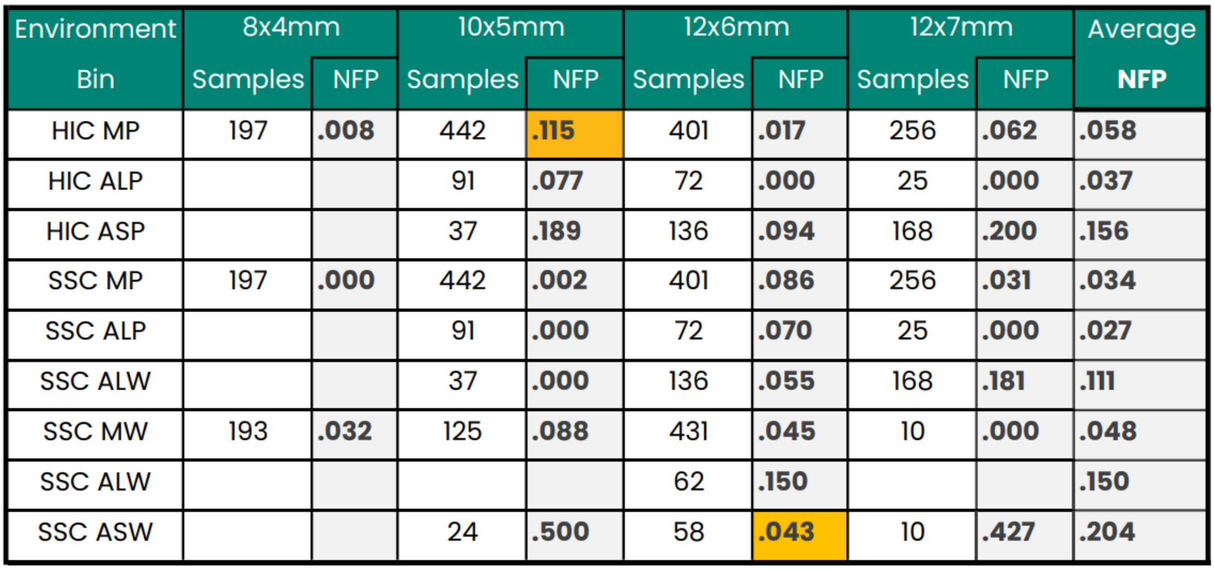

Environment Bin	8x4mm		10x5mm		12x6mm		12x7mm		Average NFP
	Samples	NFP	Samples	NFP	Samples	NFP	Samples	NFP	
HIC MP	197	**.008**	442	**.115**	401	**.017**	256	**.062**	**.058**
HIC ALP			91	**.077**	72	**.000**	25	**.000**	**.037**
HIC ASP			37	**.189**	136	**.094**	168	**.200**	**.156**
SSC MP	197	**.000**	442	**.002**	401	**.086**	256	**.031**	**.034**
SSC ALP			91	**.000**	72	**.070**	25	**.000**	**.027**
SSC ALW			37	**.000**	136	**.055**	168	**.181**	**.111**
SSC MW	193	**.032**	125	**.088**	431	**.045**	10	**.000**	**.048**
SSC ALW					62	**.150**			**.150**
SSC ASW			24	**.500**	58	**.043**	10	**.427**	**.204**

7.4 Single Factor Linear Model

Given the microstructure observations, it would be reasonable to expect one factor to determine the wire performance at least for one failure mechanism. The following section summarizes this attempt. The analysis results will be presented as bar graphs. The bar height indicates the NFP. Near the top of the bar there is a number indicating the number of samples from which the NFP is calculated. Whenever the number of samples is lower than 35 the NFP is treated as an unreliable indication. The NFP scale is narrowed for the sake graphs clarity. In case of bars higher than can be shown on the graph the NFP will be listed under the number of samples. For each factor, there will be three separate graphs, each for one of failure mechanisms.

Intentionally left blank

7.4.1 Sulphur

The effect of sulphur content on HIC NFP is presented in Fig. 7.6. There is a strong correlation between NFP and sulphur content for environments M and AL. Reduction of sulphur is not sufficient to eliminate HIC in environment AS. Somewhat surprising is a lack of failures in the highest sulphur category in environments AL and AS.

The effect on parent SSC is shown in Fig. 7.7. It reveals beneficial effect of high sulphur above 0.010% in environment M. There is a NFP minimum for sulphur content 0.010 % to 0.013% in environment AS.

The weld SSC NFP show in Fig. 7.8 shows no effect of sulphur, except for the highest sulphur content category. There is an indication based on small number of samples that for the lowest category (S < 0.004%) the NFP can be lower.

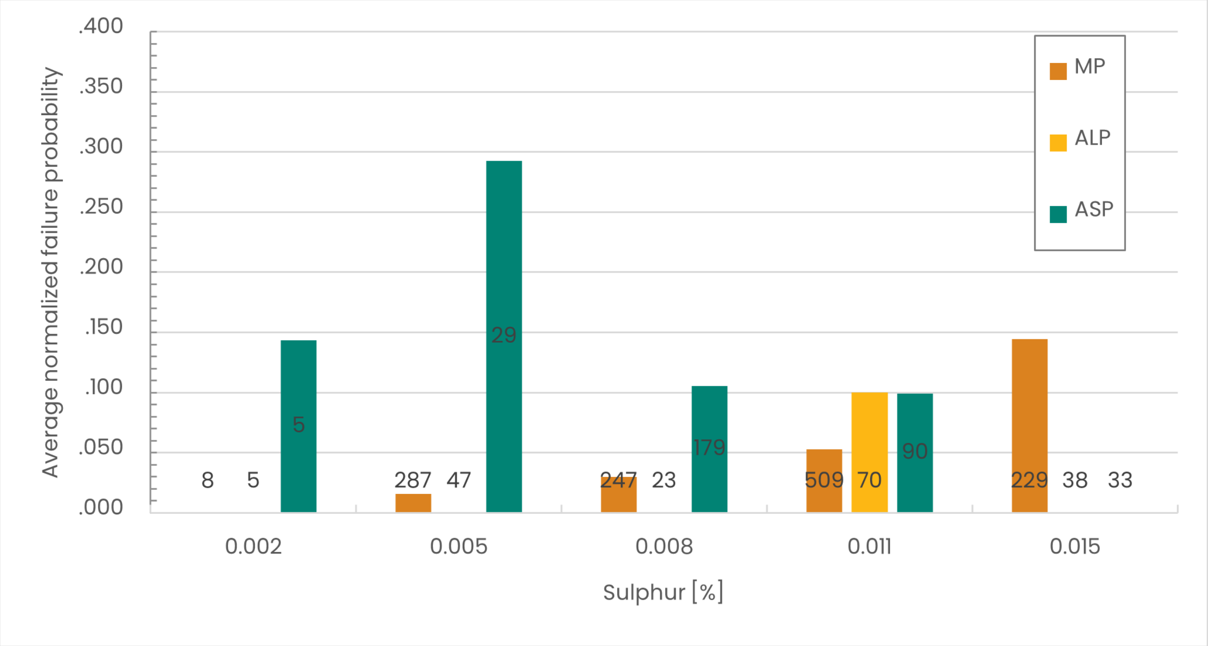

Figure 7.6: Effect of S on HIC measured as NFP.

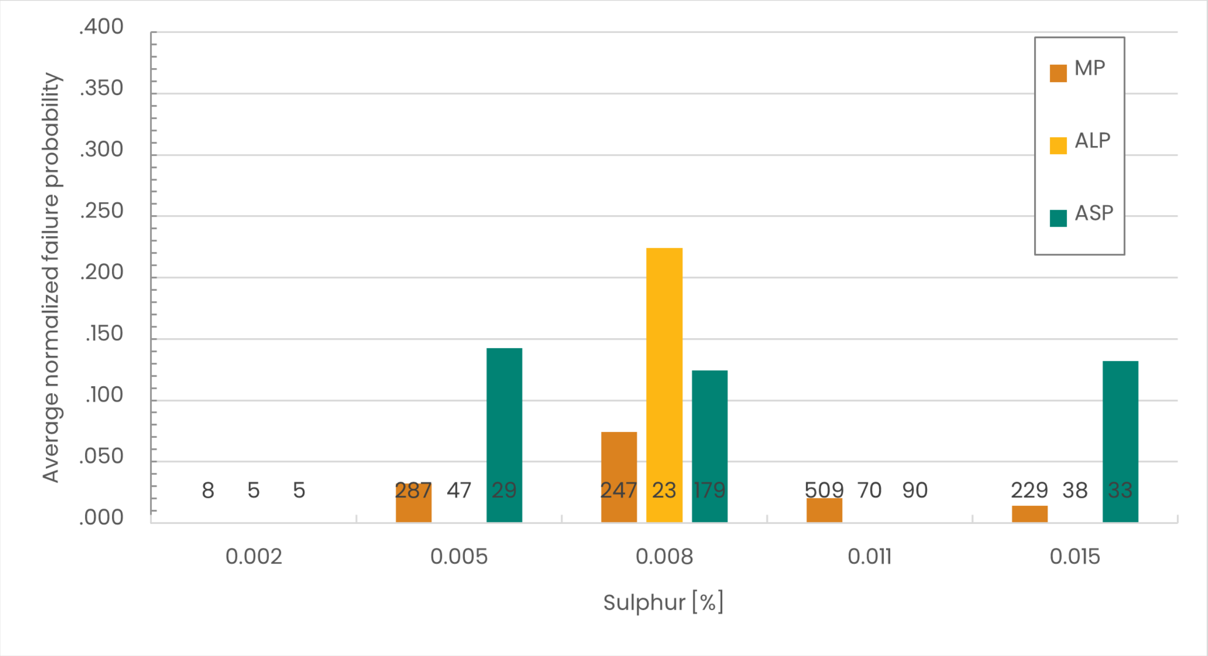

Figure 7.7: Effect of S on SSC parent measured as NFP.

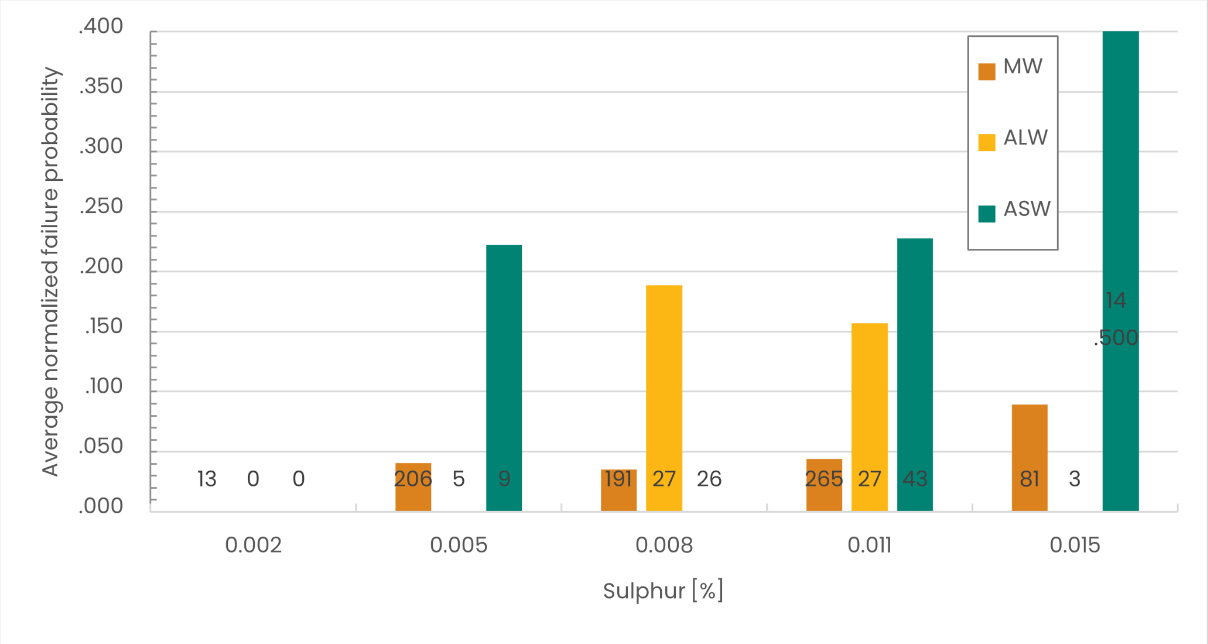

Figure 7.8: Effect of S on weld SSC measured as NFP.

7.4.2 Phosphorus

The effect of phosphorus on HIC is presented in Fig. 7.9. Samples in environment M and AL showed very low NFP when phosphorus was up to 0.006 %. Surprisingly the highest phosphorus category 0.013 % to 0.016 % showed reduction in HIC in environment M. The highest NFP was for wires with phosphorus level between 0.006 % and 0.014 %.

The effect on parent SSC is shown in Fig. 7.10. The NFP in environment M peaks in category 0.04 % to 0.06% and is relatively constant for higher concentrations. The NFP in Al environment seems to monotonically increase with phosphorus content.

The weld SSC shows a minimum when phosphorus in 0.006 % to 0.010 % in environment M ans shown in Fig. 7.11.

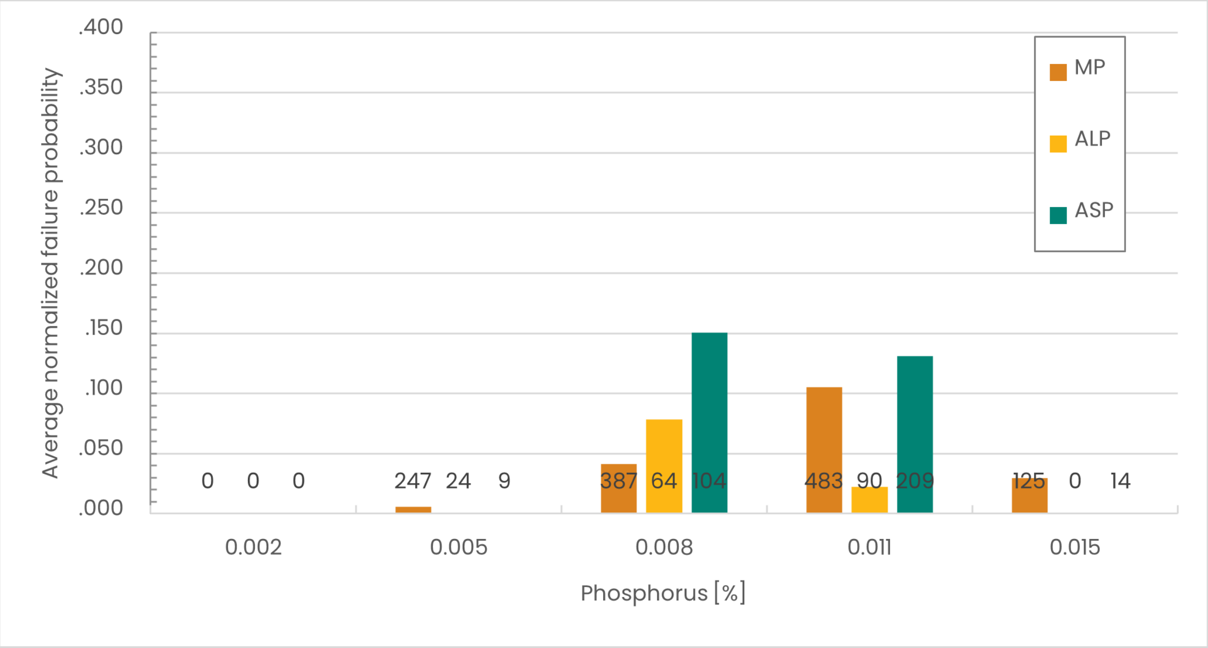

Figure 7.9: Effect of P on HIC measured as NFP.

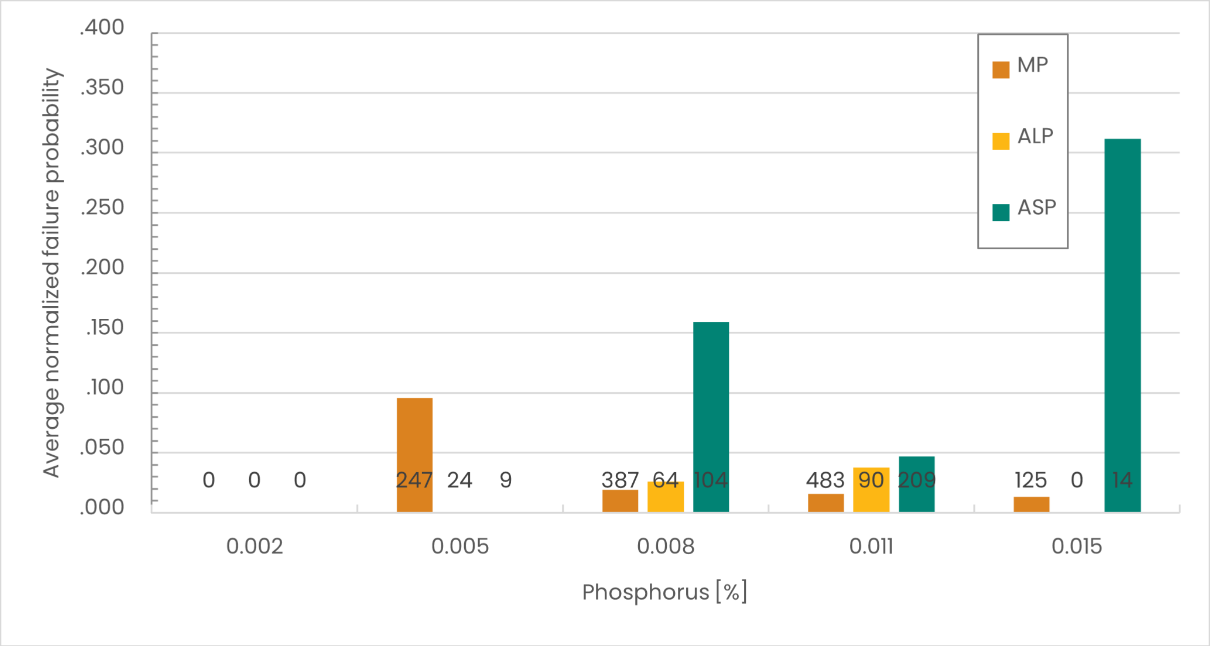

Figure 7.10: Effect of P on SSC parent measured as NFP.

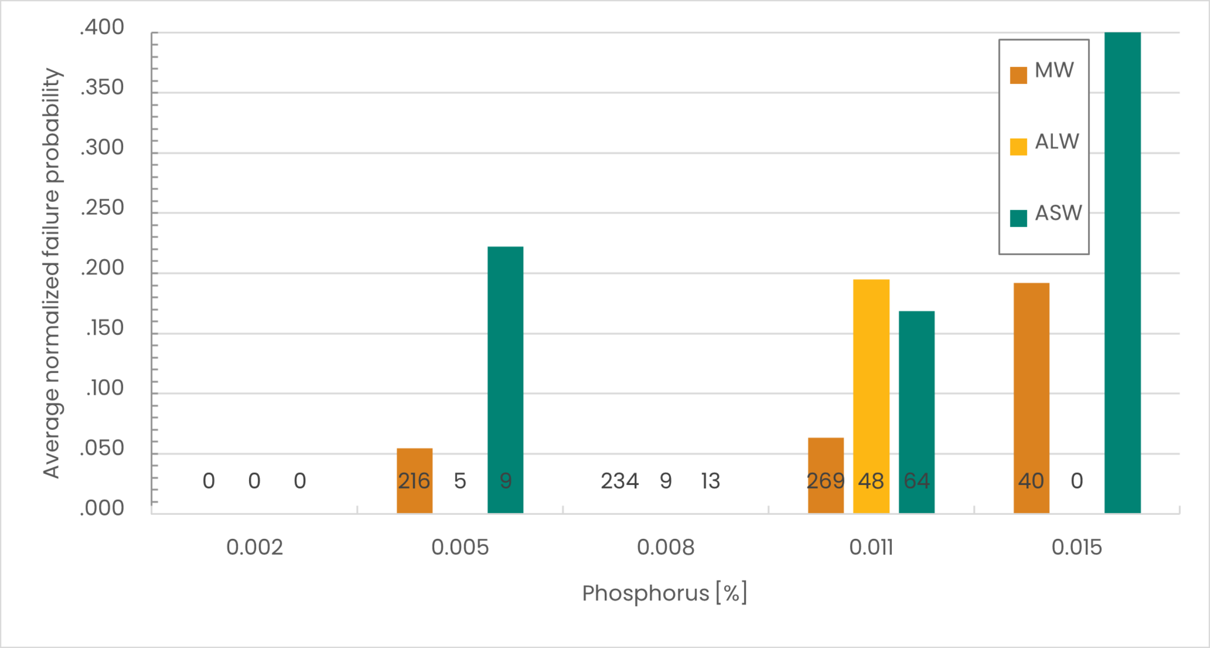

Figure 7.11: Effect of P on weld SSC measured as NFP.

7.4.3 Manganese

Analysis of HIC susceptibility as a function of manganese is shown in Fig. 7.12. Manganese has a clear deleterious effect in AL environment. Similar trend is shown in environments M and AS, with the exception of the category with the lowest manganese content where the NFP is very high. In environment M the local maximum seems to be 0.64 % to 0.66 %.

Manganese has a deleterious effect on parent SSC as shown in Fig. 7.12. The NFP increases with increasing manganese content for all environments, with the exception of the highest manganese content.

For weld SSC manganese seems to have no effect on NFP in M environment as shown in Fig. 7.14. The count of samples in other categories is insufficient to discern any trends.

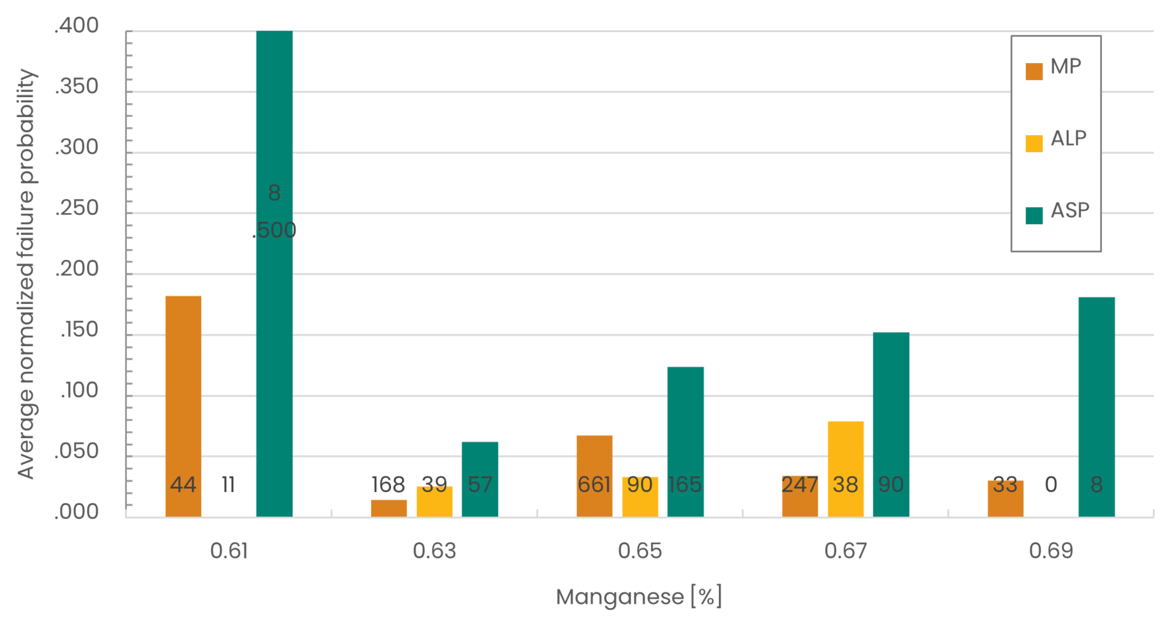

Figure 7.12: Effect of Mn on HIC measured as NFP.

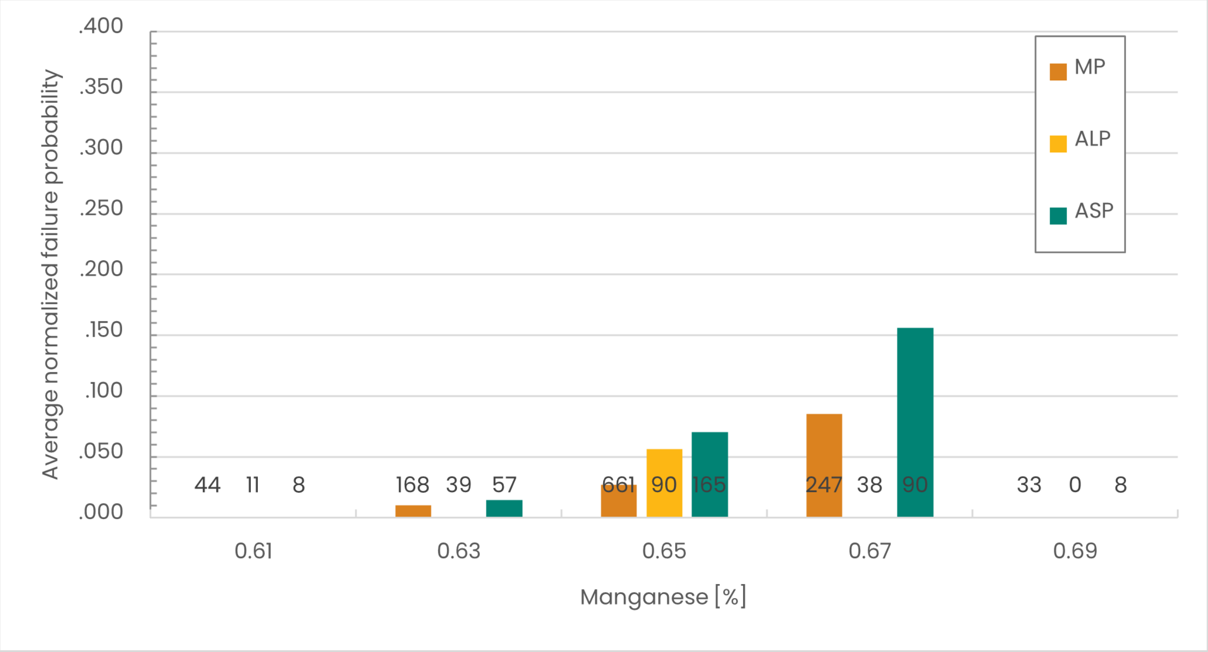

Figure 7.13: *Effect of Mn on SSC parent measured as NFP.*

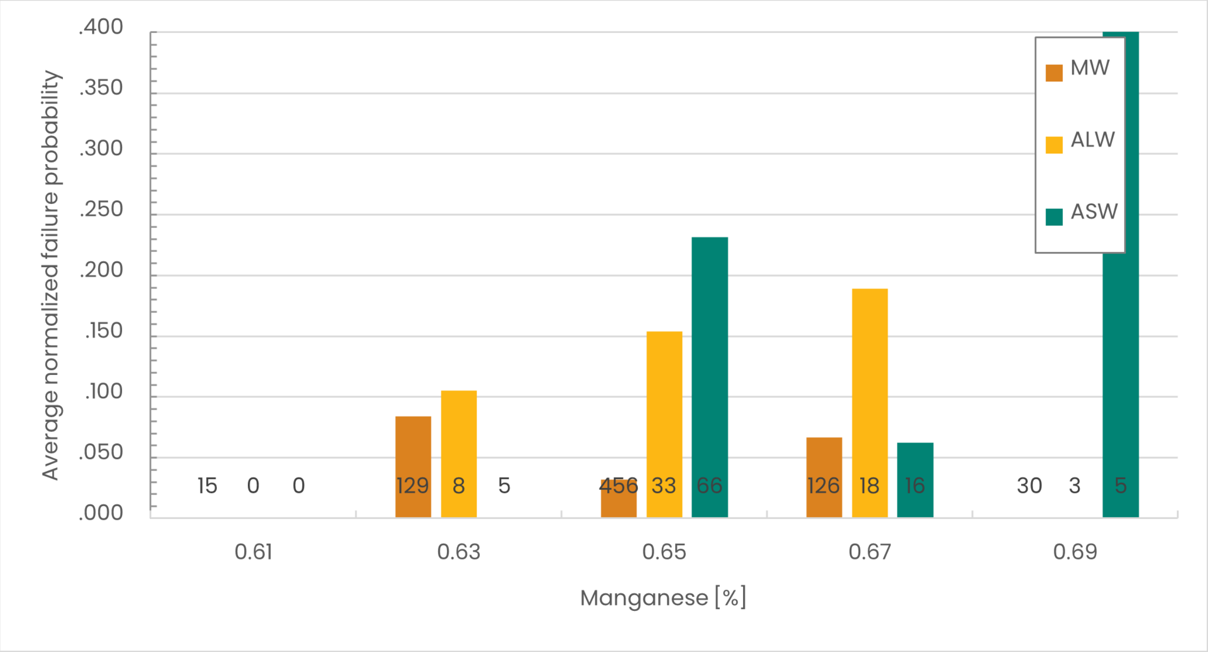

Figure 7.14: *Effect of Mn on weld SSC measured as NFP.*

7.4.4 Silicone

The HIC susceptibility as a function of silicone shows a local maximum between 0.18 % and 0.22 % in all environments as shown in Fig. 7.15.

The parent SSC increases with the increasing silicone content above 0.22 % in environment M. In environment AL the NFP decreases with the increasing silicone content.

Fig. 7.16 shows influence on parent SSC. In the environment M there is a NFP minimum at silicone concentration 0.20 % to 0.22 %. In environment AL increase in silicone seems to decrease NFP. For environment AS silicone concentration 0.20 % to 0.22% correlates with the lowest NFP.

Silicone appears to have a deleterious effect on weld SSC in environment M. The NFP is the lowest for silicone lower than 0.20 %, as shown in Fig. 7.17. In the other two environments the number of samples is too sparse to draw conclusions.

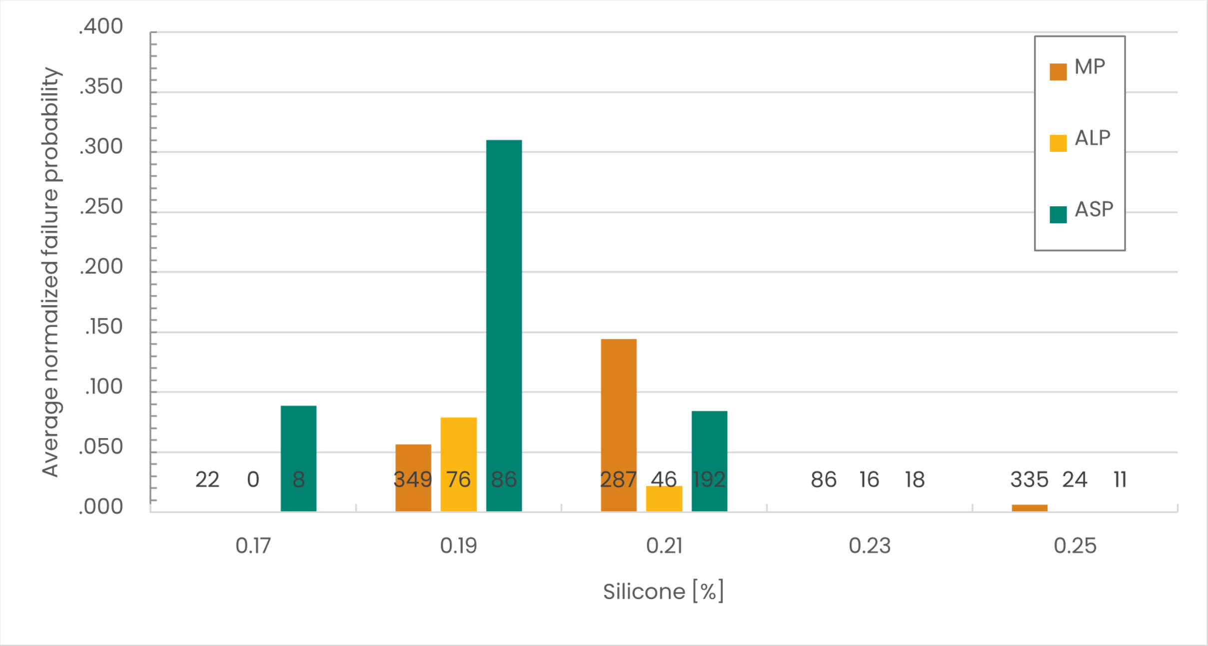

Figure 7.15: Effect of Si on HIC measured as NFP.

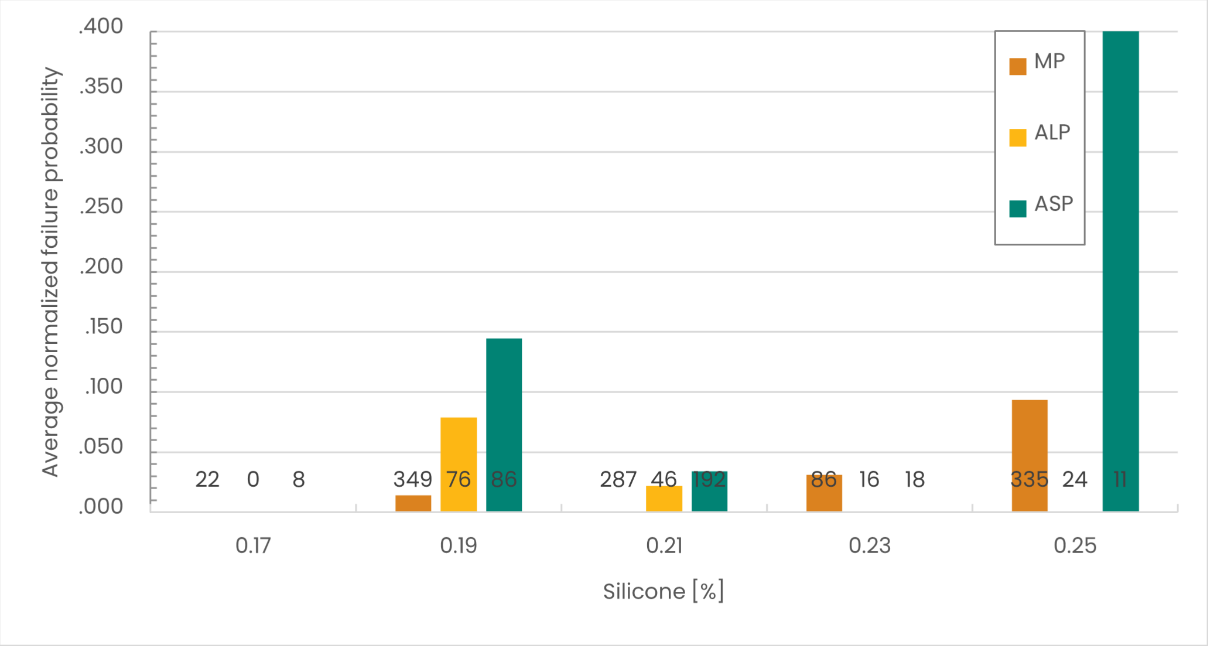

Figure 7.16: Effect of Si on SSC parent measured as NFP.

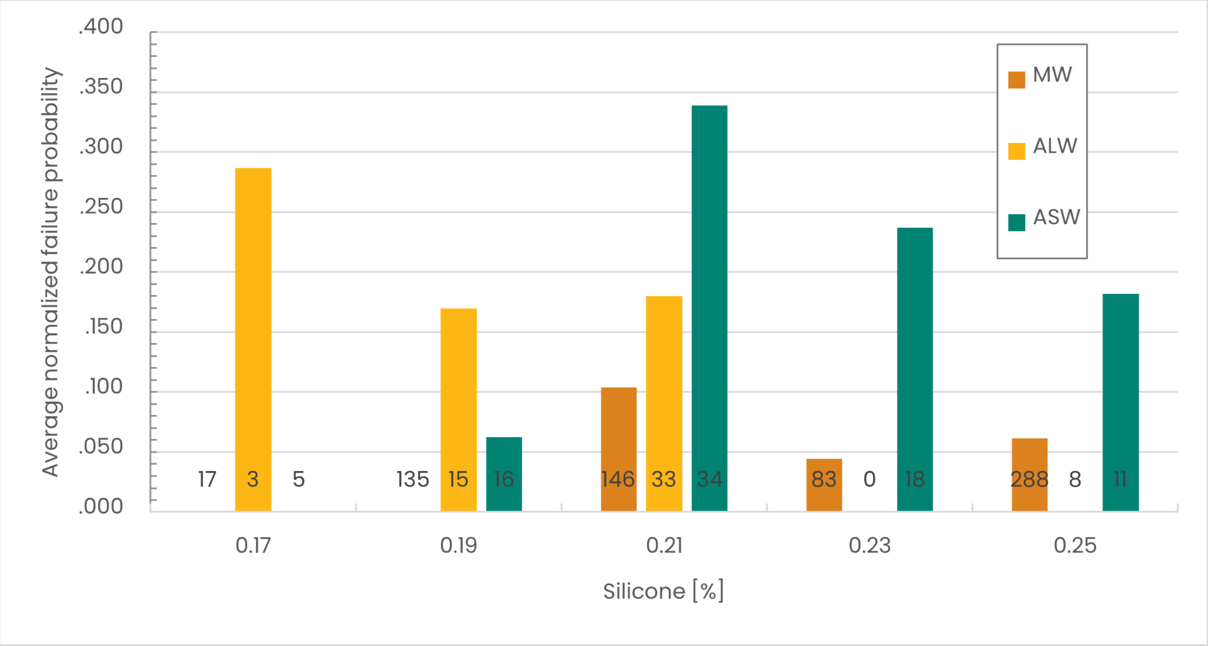

Figure 7.17: Effect of Si on weld SSC measured as NFP.

7.4.5 Carbon

The HIC susceptibility shows a local maximum in-between 0.66 % and 0.68 % carbon for all environments. There were no failures in the highest carbon category, as shown in Fig. 7.18.

The parent SSC susceptibility seems to have no correlation with carbon content in environment M. In environment AL the only failures occurred for carbon content 0.67 % - 0.68 %, as shown in Fig. 7.19. It seems that high carbon is beneficial in reducing NFP in AS environment, but small number of samples was tested.

The weld SSC in environment M shows no correlation with carbon content. The results for AL environment are based on too few samples to draw a conclusion. Carbon seems deleterious in environment AS, as shown in Fig. 7.20

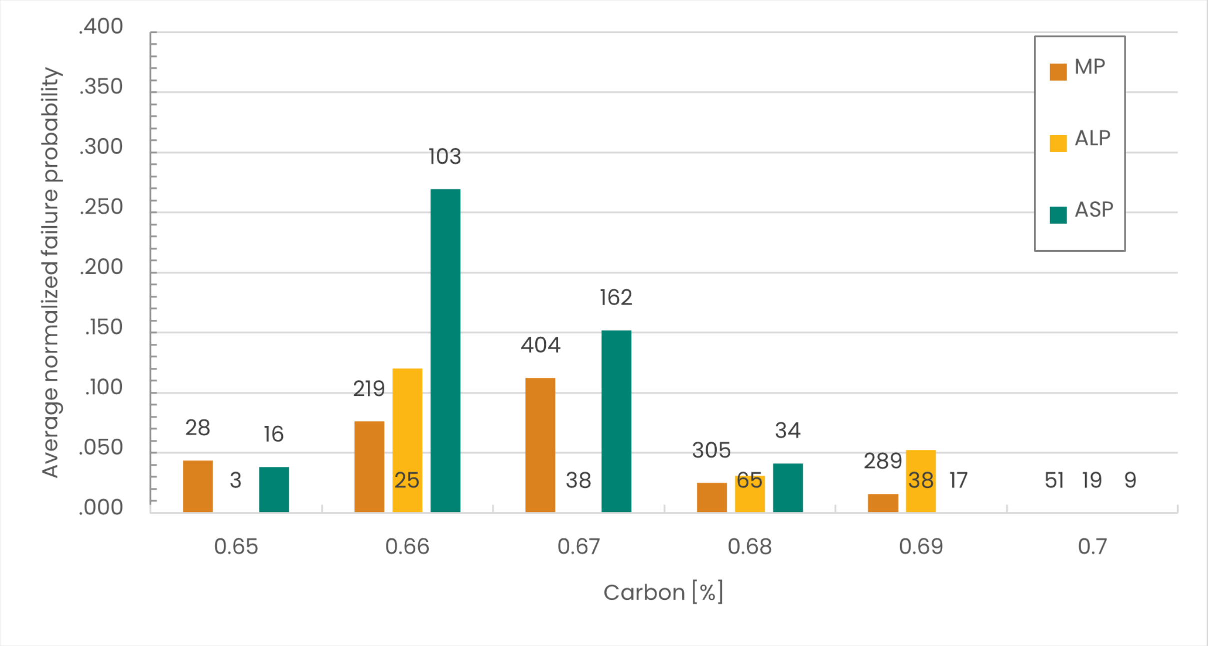

Figure 7.18: Effect of C on HIC measured as NFP.

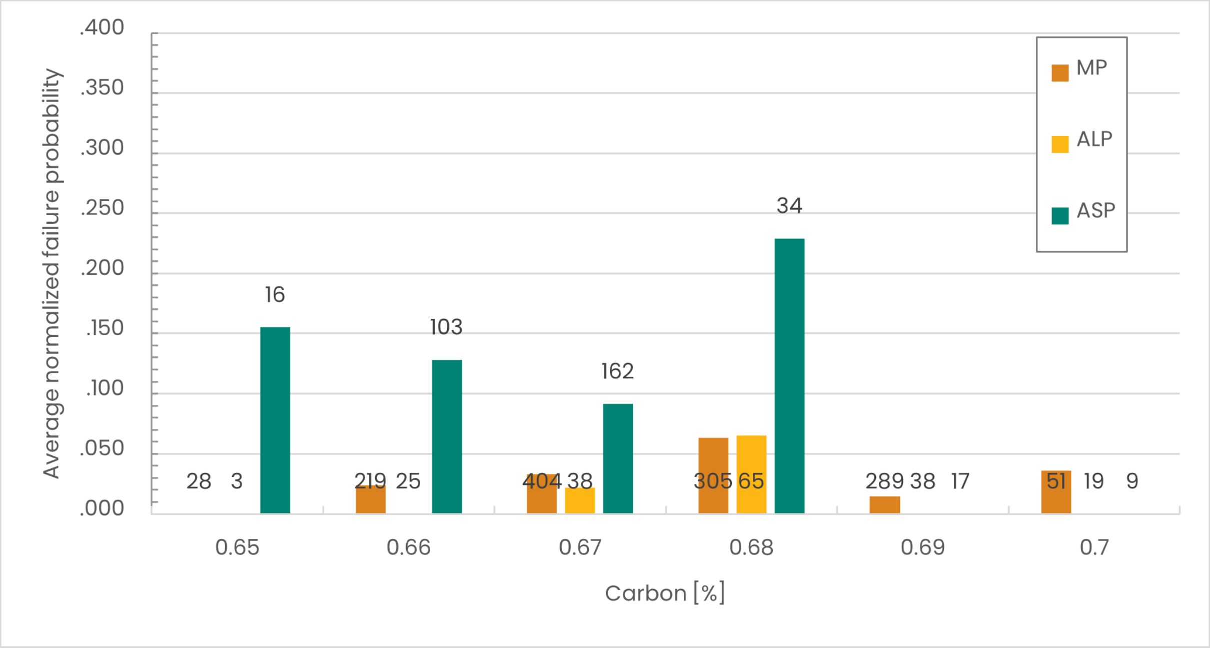

Figure 7.19: *Effect of C on SSC parent measured as NFP.*

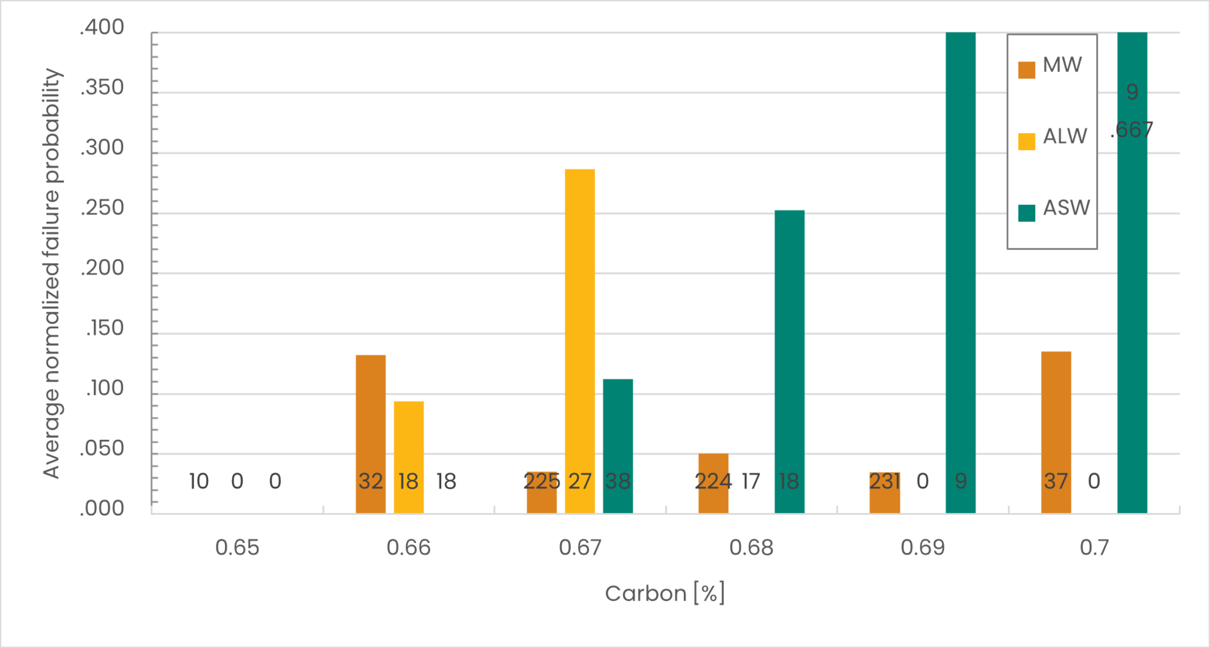

Figure 7.20: *Effect of C on weld SSC measured as NFP.*

7.4.6 Copper

Copper is not controlled by the material specification, but is sometimes reported on the certificate. Analysis of HIC susceptibility shows that a trace amounts of copper 0.03% to 0.06% reduce the NFP in M and AS environments, as shown in Fig. 7.21.

The opposite effect was observed for parent SSC susceptibility. Copper increased NFP in all environments, as shown in Fig. 7.19.

The weld SSC showed deleterious effect of copper in environment M, but positive effect in environment AL and AS, as shown if Fig. 7.23.

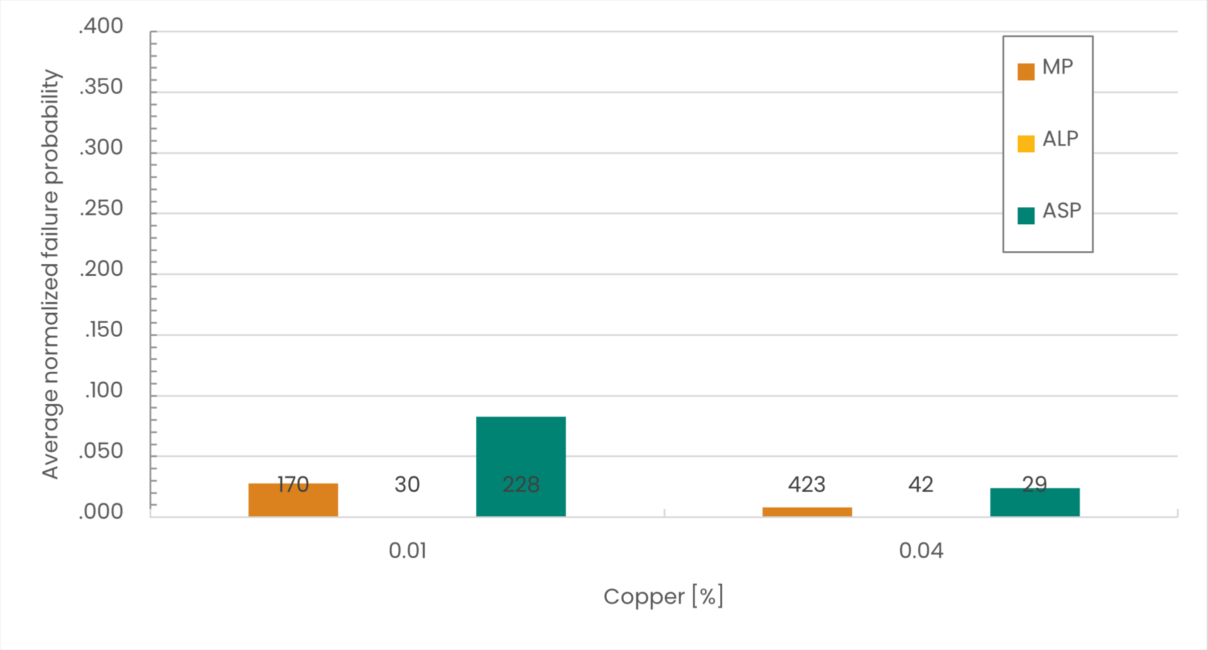

Figure 7.21: Effect of Cu on HIC measured as NFP.

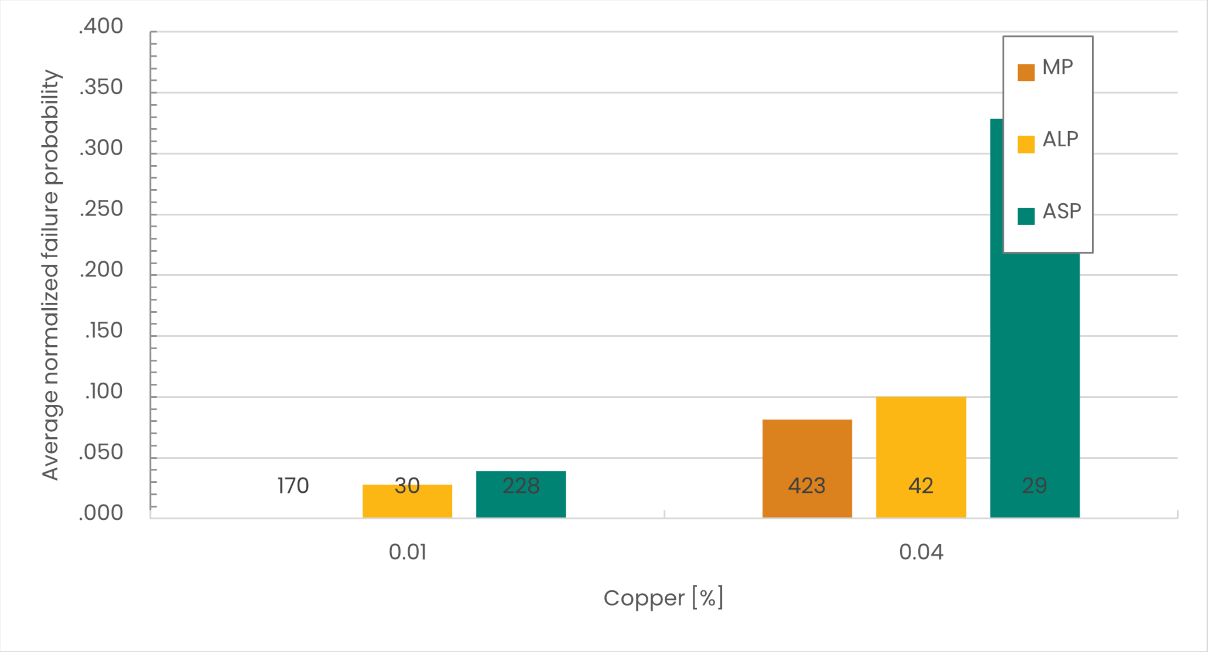

Figure 7.22: Effect of Cu on SSC parent measured as NFP.

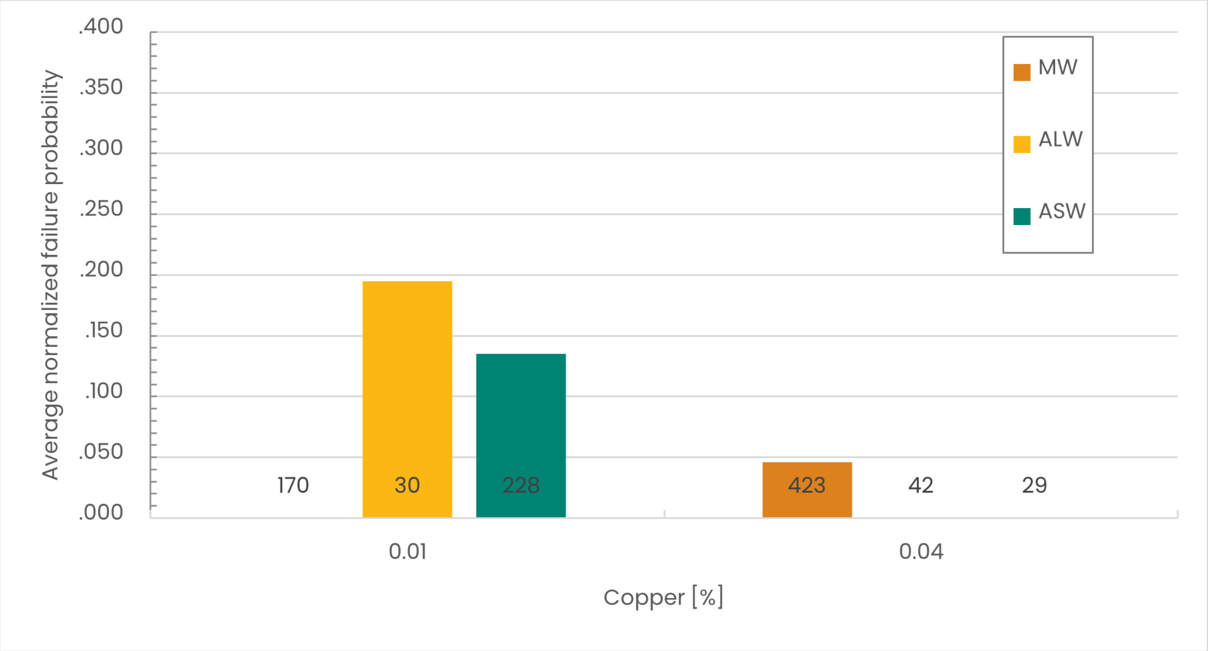

Figure 7.23: Effect of Cu on weld SSC measured as NFP.

7.4.7 Ultimate Tensile Strength

The HIC susceptibility decreases with actual UTS increasing in environment M. For other environments, there are too few samples to judge the effect, as shown in Fig. 7.24.

For parent SSC the NFP increases rapidly with the increasing actual UTS in environment M. There were no failures in the lowest strength category as shown in Fig. 7.25.

No graph for weld SSC is presented here. No correlations were found.

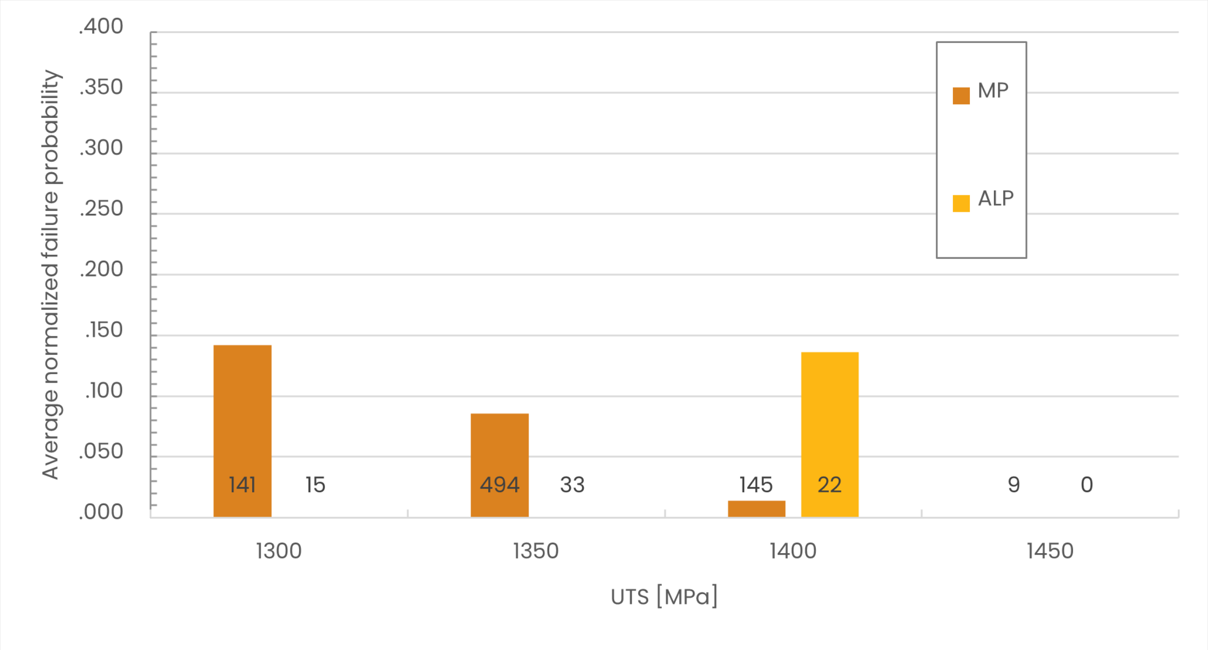

Figure 7.24: Effect of UTS on HIC measured as NFP.

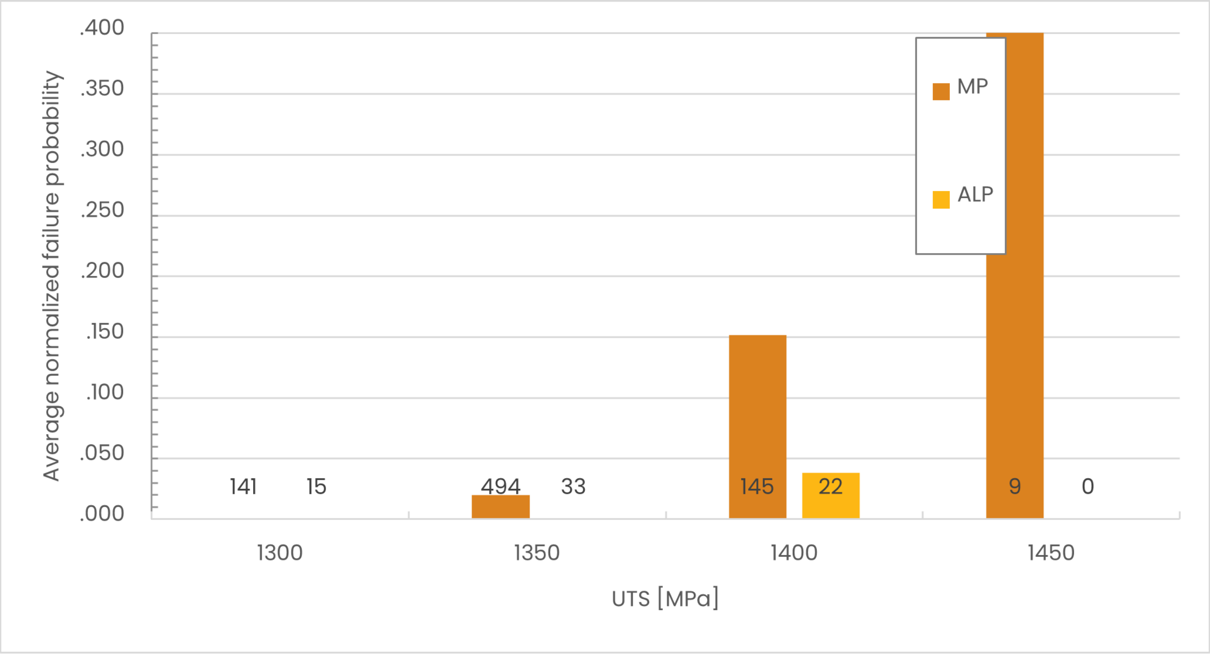

Figure 7.25: Effect of UTS on SSC parent measured as NFP.

7.4.8 Elongation

The NFP for HIC and parent SSC in M environment shows a common minimum when the wire elongation is 9 % to 13 %, as shown in Fig. 7.26 and 7.27. The NFP increases for elongations lower or greater than this range. The number of samples in the other environments is insufficient to discern any trends.

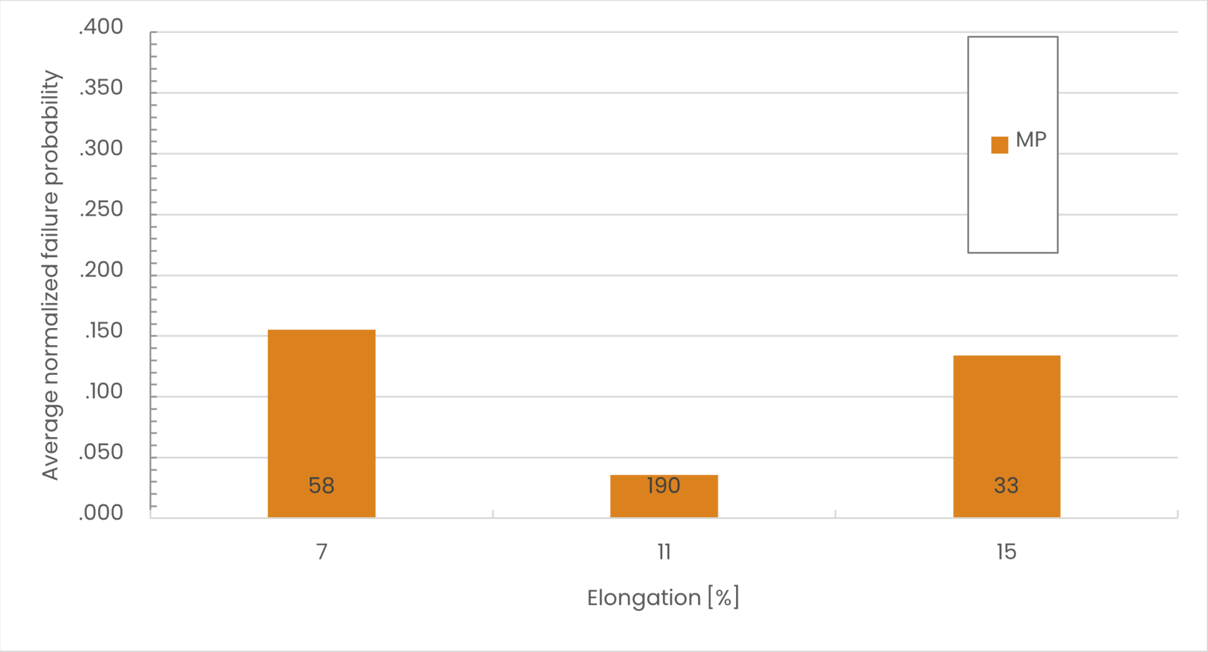

Figure 7.26: Effect of elongation on HIC measured as NFP.

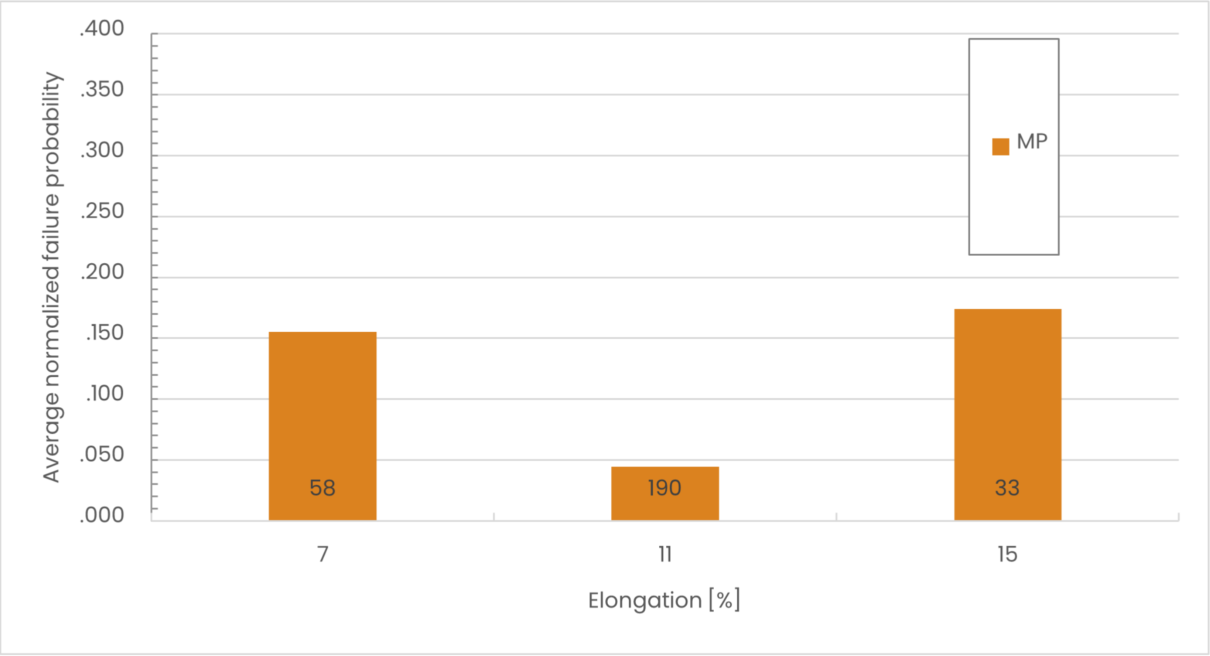

Figure 7.27: Effect of elongation on SSC parent measured as NFP.

7.4.9 Summary

Based on the single factor linear models it is evident that the chemical composition affects NFP of individual failure mechanisms. Whenever only one of those mechanisms is concerned in one environment, the H_1 is true. Whenever the sum of NFPs for all mechanisms is concerned, there is no sufficient evidence to deem H_0 or H_1 true. It appears that out of the elements listed, the design of a robust alloy could be based on high carbon 0.68 - 0.70 % and extra low sulphur < 0.0035 %. The other alloying options are conflicting.

There were multiple surprising results when the NFP did not follow the literature trends. Probably the most surprising was the result for M environment, where the NFP for HIC and parent SSC decreased when the phosphorus exceeded 0.014 %. Phosphorus is known to improve corrosion resistance of weathering steels and cast irons [83] by forming a phosphatic layer within patina layers. The embrittling effect became evident only in welds which showed increase in NFP with the increasing phosphorus content.

It was shown that copper despite very low concentration improved the protectiveness of the corrosion products thus reducing HIC. On the other hand the SSC performance was severely compromised. This was expected, as it was mentioned in the literature review that copper embrittles grain boundaries during cold deformation. The most curious effect was for weld SSC where in environment M copper was deleterious, but in environments AL and AS it was beneficial. There's no explanation in the literature linked to that observation.

High carbon content affects the steel microstructure, reducing the content of ferrite. Ferrites grain boundaries are the preferred spots for HIC initiation. It can be interpreted as having more uniform microstructure improves HIC. On the other hand it seems that the HIC susceptibility was reduced also in the lowest carbon category, which is counter intuitive.

The Ireland and Wheeler method evaluation of flow resistance showed no correlation between flow resistance near the wire centreline and HIC. Flow resistance in X direction approximates actual UTS. Given that result it is surprising that high UTS reduced the occurrence of HIC. The increase of UTS increases the SSC susceptibility which is in line with expectations. It is the scale of increase in susceptibility that is surprising. The elongation in-between 9 % and 13 % showed a very positive influence on both HIC and parent SSC resistance. Elongation can be treated as a measure of microstructure damage, but it is unknown why elongations higher than 13 % would increase NFP.

It can be summarized that the analysis approach is unsatisfactory. There are trends that follow existing models of failure, but there are also observations that deny those models. A consistent model of failure could not be constructed from those observations.

7.5 Orthogonal Matrix

Orthogonal Matrix is a tool for design of experiments where analysis and optimization of multiple interacting factors is required [84, 85]. The procedure carried out here is equivalent of a supervised decision tree in machine learning [86]. Through multiple refinements it was found that the minimum design where optimum solutions were found consisted of 5 factors (C, Si, Mn, S, P). Carbon, Silicone and Manganese were attributed with 2-level factorials (sub-bins). Sulphur required a three level factorial. The sulphur levels were set following the literature [37]. Phosphorus was treated as a cut-off point. There were a total of 24 combinations which were analysed. In essence, the method utilizes a matrix in which each factor is represented at each factorial level. The implementation was done in excel. The factorials were -1 for element concentration lower than a threshold and 1 for element concentration equal or higher than the threshold. Separate matrices were prepared for each sulphur factorial. For each combination, the NFPs for different failure mechanisms and environments were calculated (representing nine bins summarized in Table 7.3). The optimum solutions are defined as having the lowest total NFP for environment M and AL and all failure mechanisms. The thresholds for factorization were set with Excel Solver. The optimization was setup so that the maximum number of combinations with at least 35 samples in each of nine bins is obtained. The result was then fine-tuned by hand, in particular phosphorus was adjusted in a way to understand the point where performance of optimum solutions degrades.

7.5.1 Extra Low Sulphur Level <0.0035 %

The matrix, thresholds and NFP are shown in Fig. 7.28. Low number of samples is available for this sulphur level. Categorization resulted in two populated combinations. Solution 6 highlighted in blue is the optimum solution for which no failures occurred.

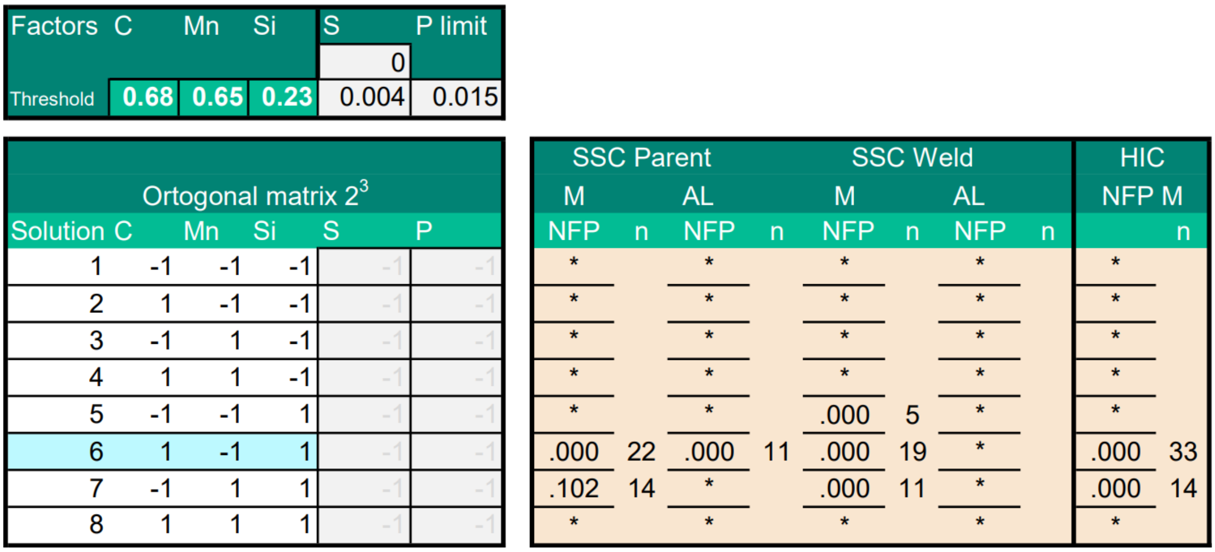

Factors	C	Mn	Si	S	P limit
				0	
Threshold	0.68	0.65	0.23	0.004	0.015

Ortogonal matrix 2^3						SSC Parent				SSC Weld				HIC	
						M		AL		M		AL		NFP M	
Solution	C	Mn	Si	S	P	NFP	n	NFP	n	NFP	n	NFP	n		n
1	-1	-1	-1	-1	-1	*		*		*		*		*	
2	1	-1	-1	-1	-1	*		*		*		*		*	
3	-1	1	-1	-1	-1	*		*		*		*		*	
4	1	1	-1	-1	-1	*		*		*		*		*	
5	-1	-1	1	-1	-1	*		*		.000	5	*		*	
6	1	-1	1	-1	-1	.000	22	.000	11	.000	19	*		.000	33
7	-1	1	1	-1	-1	.102	14	*		.000	11	*		.000	14
8	1	1	1	-1	-1	*		*		*		*		*	

Figure 7.28: Matrix for categorization of test results for extra low sulphur.

7.5.2 Low Sulphur Level 0.0035 < S % < 0.009

The matrix, thresholds and NFP are shown in Fig. 7.29. The number of samples in this category was sufficient to populate all combinations. The solutions with the lowest NFP are solution 2 and 4 highlighted in blue. The worst performing solution was solution 8. The optimum solutions were fairly insensitive to phosphorus concentration up to 0.015 %.

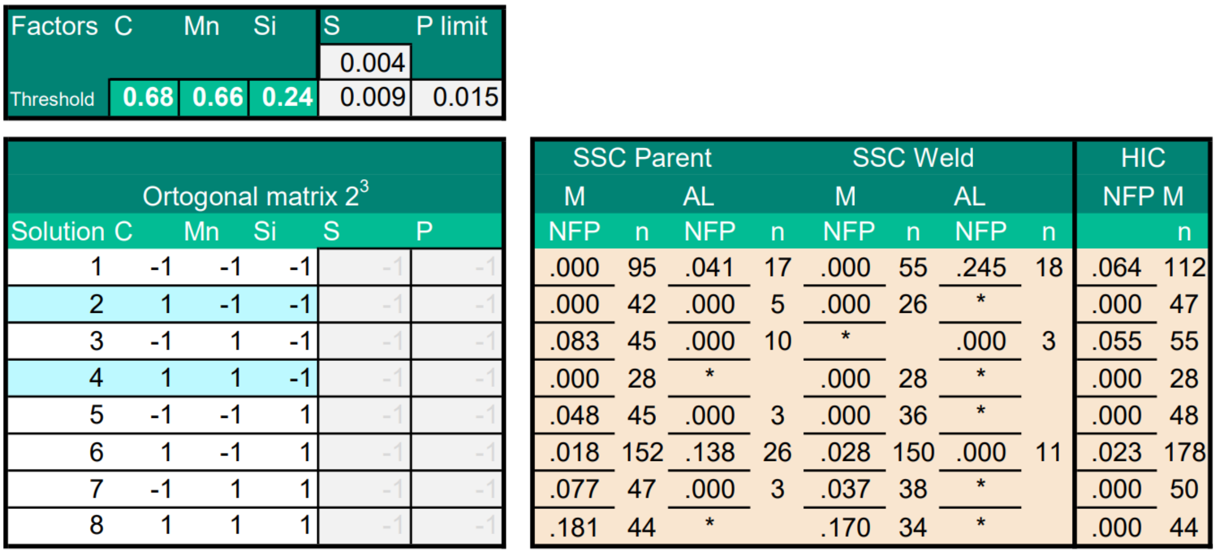

Factors	C	Mn	Si	S	P limit
				0.004	
Threshold	0.68	0.66	0.24	0.009	0.015

Ortogonal matrix 2^3						SSC Parent				SSC Weld				HIC	
						M		AL		M		AL		NFP M	
Solution	C	Mn	Si	S	P	NFP	n	NFP	n	NFP	n	NFP	n		n
1	-1	-1	-1	-1	-1	.000	95	.041	17	.000	55	.245	18	.064	112
2	1	-1	-1	-1	-1	.000	42	.000	5	.000	26	*		.000	47
3	-1	1	-1	-1	-1	.083	45	.000	10	*		.000	3	.055	55
4	1	1	-1	-1	-1	.000	28	*		.000	28	*		.000	28
5	-1	-1	1	-1	-1	.048	45	.000	3	.000	36	*		.000	48
6	1	-1	1	-1	-1	.018	152	.138	26	.028	150	.000	11	.023	178
7	-1	1	1	-1	-1	.077	47	.000	3	.037	38	*		.000	50
8	1	1	1	-1	-1	.181	44	*		.170	34	*		.000	44

Figure 7.29: Matrix for categorization of test results for low sulphur.

7.5.3 Sulphur Level 0.009 < S % < 0.013

The matrix, thresholds and NFP are shown in Fig. 7.30. The best performing solutions are 4 and 6. The worst performing solution was solution 2. The optimum solutions were fairly insensitive to phosphorus concentration up to 0.015 %.

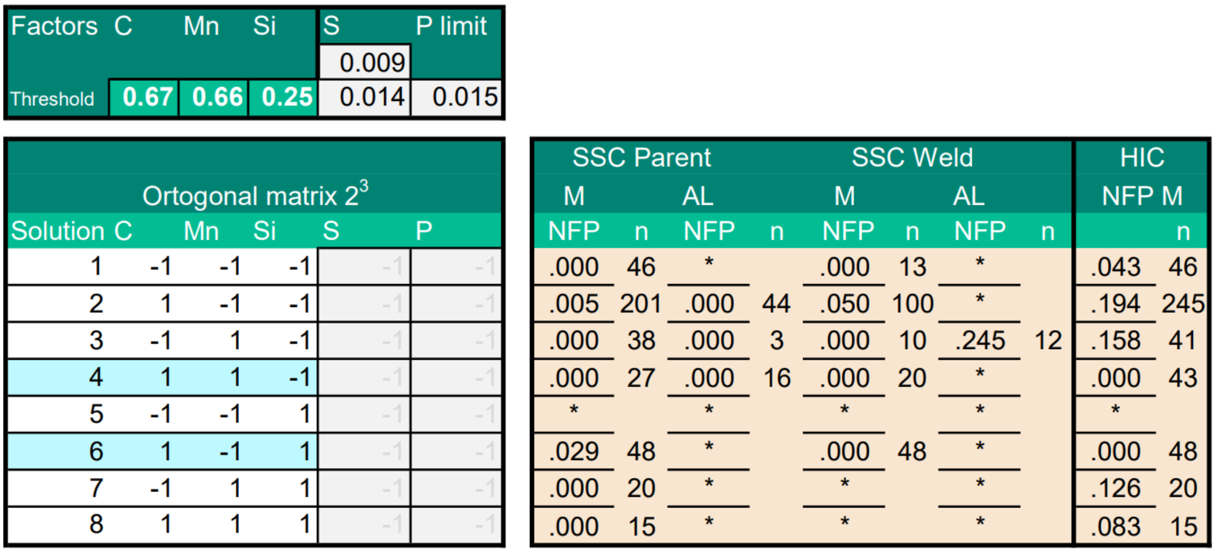

Factors	C	Mn	Si	S	P limit
				0.009	
Threshold	0.67	0.66	0.25	0.014	0.015

Ortogonal matrix 2^3					
Solution	C	Mn	Si	S	P
1	-1	-1	-1	-1	-1
2	1	-1	-1	-1	-1
3	-1	1	-1	-1	-1
4	1	1	-1	-1	-1
5	-1	-1	1	-1	-1
6	1	-1	1	-1	-1
7	-1	1	1	-1	-1
8	1	1	1	-1	-1

SSC Parent				SSC Weld				HIC	
M		AL		M		AL		NFP M	
NFP	n	NFP	n	NFP	n	NFP	n		n
.000	46	*		.000	13	*		.043	46
.005	201	.000	44	.050	100	*		.194	245
.000	38	.000	3	.000	10	.245	12	.158	41
.000	27	.000	16	.000	20	*		.000	43
*		*		*		*		*	
.029	48	*		.000	48	*		.000	48
.000	20	*		*		*		.126	20
.000	15	*		*		*		.083	15

Figure 7.30: Matrix for categorization of test results for low sulphur 0.009 < S % < 0.013.

8 Discussion of the Statistical Analysis Results

8.1 Environment Effects

Underlying issues with the testing procedure were revealed. The lack of failure in mild pH and $H_2S \geq 1$ mbar points toward a protective FeS layer formation within the corrosion products. The effect is known [87], but should not appear in acidified brine. From the data available, it is not entirely clear what is the upper limit of H_2S partial pressure for this effect to continue. From the literature review, 2 mbar were given as a threshold where the corrosion transitions from CO_2 to H_2S dominated, it is likely the upper limit.

The performance in M environment (pH$\geq$ 4.4) does not depend on H_2S concentration, as shown in the environment maps. The interpretation can be along the following. The reduced buffer strength allows for formation of protective corrosion products, where at lower pH (environments AL and AS) the scale is non-protective. Still the batch test at M condition is a valid fit for purpose test, there are failures occurring for susceptible batches. This leads to the unexplored question: Are the failures reproducible without H_2S? It is likely that CO_2 and the buffer solution by themselves can cause cracking? The NFP can be presented as a function of H_2S. This was done for two pH ranges and presented in Fig. 8.1, 8.2. For pH $\leq$ 4.4 the NFP for HIC increases with H_2S partial pressure, but NFP for parent SSC does not seem affected, or at least is not a linear function of [H_2S]. Between pH 4.4 and 5 the increase of H_2S decreases the HIC NFP and increases the parent SSC NFP. Extrapolation of trends indicates that indeed without H_2S some failure should still occur. Unfortunately welded samples data are too sparse to present the data for weld SSC on those graphs. Welded samples could

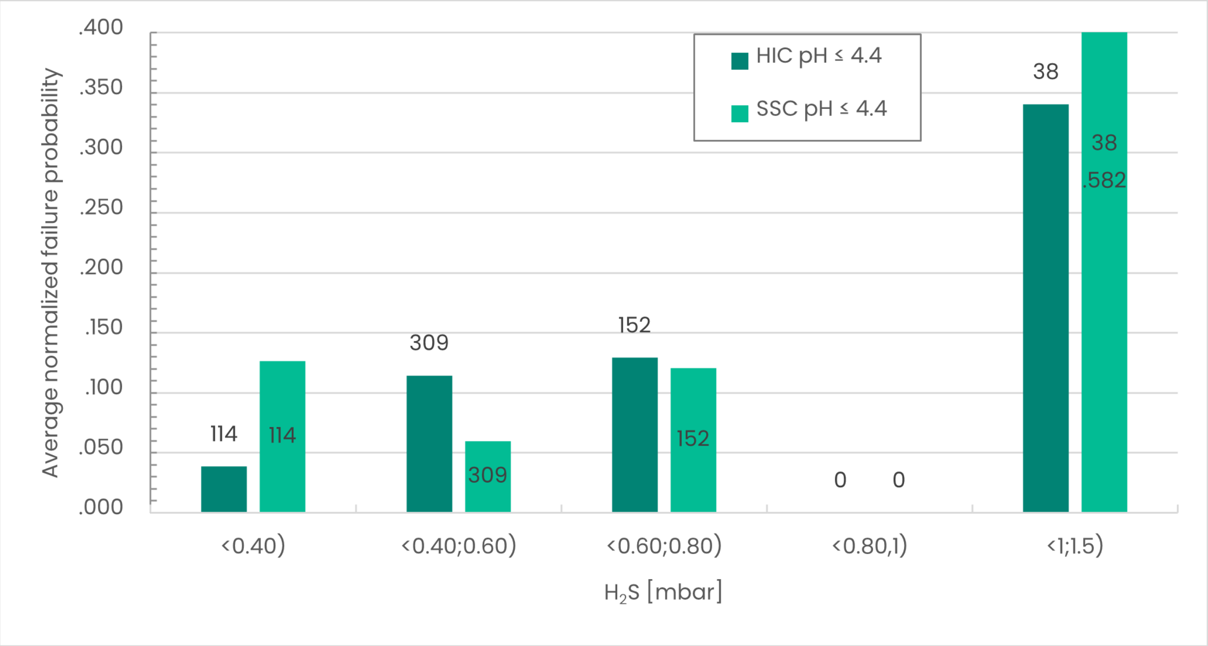

Figure 8.1: NFP as a function of H_2S partial pressure in environments with pH $\leq$ 4.4.

fail by very deep pits without SSC.

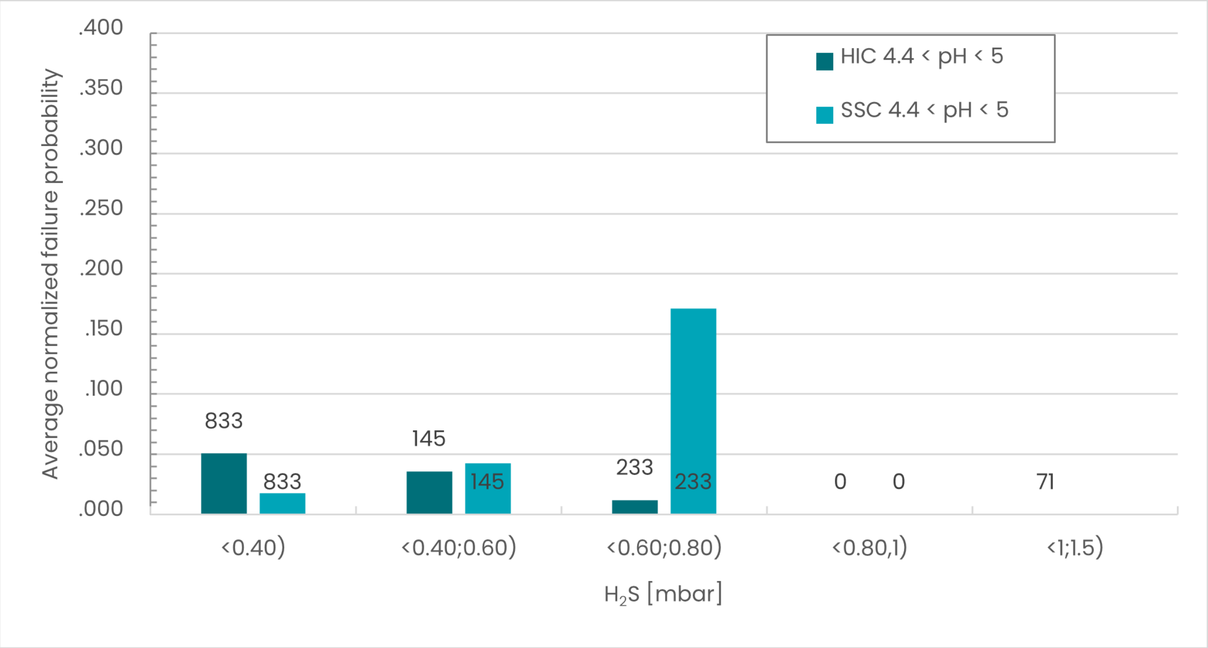

Figure 8.2: NFP as a function of H_2S partial pressure in environments with $4.4 < pH < 5$.

8.2 Consequences for Qualification

Considering the environment effects, selection of the test conditions for qualification becomes a non-trivial task. By one approach, only the harshest condition at pH ≤ 4.4 qualifies the wire up to the qualification level. By the second approach it can be argued that the environment M is the one more representative of the annulus conditions and there should be two tests carried out at local maximum of susceptibility for each mechanism. In particular, H_2S partial pressure of 0.30 mbar at pH 4.9 appears to be a local maximum for HIC susceptibility and should be used for qualification of parent wire. H_2S partial pressure of 0.75 mbar at pH 4.9 appears to be a local maximum for SSC susceptibility and should be used to for qualification of parent wires and welds.

The other consequence of this work is the notion that to estimate NFP a significant number of samples is required. It was concluded that the volume equivalent to 35 samples should be used. The number of samples can approach 72 for finer wires, which is not practical. To achieve a full qualification, it would be required to test wires from three casts, each in parent and welded condition. A massive number of samples is a practical limitation. Due to that the estimation of NFP should be an indicator of process performance, not a goal of qualification.

8.3 Mechanism of HIC

The mechanism proposed for the HIC phenomena is as following:

HIC initiates from inclusions located at ferrite grain boundaries. Extra low sulphur batches will be immune to HIC. Ferrite as the softer phase is susceptible to tearing during HIC initiation. High carbon content ($C \uparrow$) reduces the content of ferrite, and thus reduces the density of HIC initiation spots. Solid solution strengthening of ferrite by P, Si, Mn limits the localization of deformation to ferrite and increases its resistance to tearing. Ferrite strenghtening is effective in reducing the HIC susceptibility. Whenever the ($Mn \uparrow$) causes hard centreline segregation bands it results in increased localization of deformation near that band, thus increasing the HIC susceptibility.

By the proposed model the wires with the chemical composition along solutions 1 and 2 ($Mn \downarrow, Si \downarrow$) would gather the most localized microstructural damage during the cold rolling and thus become the most susceptible to HIC. The solution 3 ($C \downarrow$

$, Mn \uparrow, Si \downarrow$) develops the centreline segregation which leads to high localization of damage. The solution 4 ($C \uparrow, Mn \uparrow, Si \downarrow$) should accumulate damage to a similar extent to the solution 3. The solution 5 ($C \downarrow 1, Mn \downarrow 1, Si \uparrow$) should accumulate less damage despite ferrite content being high. The deformation should be generalized due to high silicone content. The solution 6 ($C \uparrow, Mn \downarrow, Si \uparrow$) should have the best performance as the ferrite content is low and the localisation of damage is low. The solutions 7 ($C \downarrow, Mn \uparrow, Si \uparrow$) and 8 ($C \uparrow, Mn \uparrow, Si \uparrow$) performance should be lower due to localization from manganese segregation.

The model for predicting HIC seems to be supported by observations. For S % > 0.0035 the solution 4 ($C \uparrow, Mn \uparrow, Si \downarrow$) is a notable outlier outperforming the prediction, most likely manganese in absence of silicone ($Si \uparrow$) does not form segregation bands. Solution 7 seems to be performing well for low sulphur level batches, but the tests were carried out at comparatively high pH.

It seems that HIC does not respond to hydrogen trapping capacity of the wire. There is no significant effect of sulphur above 0.0035 %. Likely, HIC damage occurs only after the protective corrosion products have formed, and not during the initial hydrogen flux spike at the beginning of the test.

8.4 Mechanisms of Weld SSC

The following model of welded wire SSC is proposed.

The pitting initiates at manganese sulphide inclusions extruded toward the surface during wire upsetting. Extra low sulphur wire is resistant to weld SSC. The SSC initiation is affected by the distribution of inclusions within the wire. High silicone level ($Si \uparrow$) aids in segregation of manganese sulphide inclusions toward the wire centre, resulting in inclusion-free subsurface. Conditions for SSC occur only temporarily until formation of protective corrosion products layer. In the environment M it occurs shortly after the test started, during corrosion products build-up. For SSC to occur consistently environment AL is required where the corrosion products are less protective. High trapping potential of inclusions effectively retards cracking, as the critical concentration of hydrogen for SSC $[N_C]$ is not reached before the hydrogen flux drops. Whenever pits initiated, but the SSC did not occur due to formation of protective corrosion products, very deep pits can grow up to the sample failure.

It can be speculated that low manganese should reduce the galvanic corrosion potential between bond line and CG HAZ. However, there was a lack of data to confirm it. It would be of interest to re-evaluate this hypothesis by rating the corrosion damage near the weld as a function of manganese on the photographs in the test reports.

The proposed mechanism explains the reduction in NFP for weld SSC with increasing sulphur content in environment M, very high NFP in environment M for low Si, and passes of two batches of wire having high silicone at for low sulphur level (0.0035 < S % < 0.009), and one pass in AS environment for extra low sulphur batch.

It can be speculated that additional H_2S is produced during corrosion of the manganese sulphide. This creates locally very aggressive environment that is occluded under the corrosion products. This observation is supported by the pit morphology showing rounded and shiny pit bottoms.

8.5 Mechanisms of Parent SSC

The following model for the parent wire SSC is proposed.

> Conditions for SSC are only temporary until formation of protective corrosion products layer. For parent SSC to occur the cracking has to initiate shortly after the test started, during corrosion products build-up. High trapping potential of inclusions effectively retards cracking, as the critical concentration of hydrogen for SSC $[N_C]$ is not reached before the hydrogen flux drops. At pH > 5.5 the SSC does not occur. The parent SSC initiates at prior austenite grain boundaries decorated with allotriomorphic ferrite. High carbon ($C \uparrow$) limits the density of potential crack initiation spots. Deformation from cold rolling localizes in ferrite grains. Solid solution strengthening limits that effect and is beneficial. The beneficial effect is counteracted by phosphorus segregation to grain boundaries enabled by high manganese and silicone ($Mn \uparrow \cap Si \uparrow$). Segregation of phosphorus lowers the grain boundary cohesion thus greatly increasing the susceptibility to SSC.

By the model the solutions 1 ($C \downarrow, Mn \downarrow, Si \downarrow$) and 7 ($C \downarrow, Mn \uparrow, Si \uparrow$) should perform the worst. The best performance is expected from solutions 4 ($C \uparrow, Mn \uparrow, Si \downarrow$) and 6 ($C \uparrow, Mn \downarrow, Si \uparrow$).

The proposed model explains failure of extra low sulphur wire (solution 6 vs solution 7) and observations of NFP in low sulphur level (0.0035 < S % < 0.009). The model explains the small difference between environments. The protective corrosion products need to show lesser protectiveness to prevent SSC, as compared to weld SSC. Thus the conditions for SSC are temporary in all environments.

There is an obvious outlier, solution 7 ($C \downarrow, Mn \uparrow, Si \uparrow$) for sulphur levels 0.0035 < S % < 0.013 should have performed the worst.

8.6 Optimization of the Wire Chemistry and Batch Test Environment Limits

The analysis showed that there are three optimum solutions addressing all failure mechanisms. The chemical compositions can be summarized as shown in the Table 8.1.

Table 8.1: Chemical composition of the optimized MTL-5100 wire.

Solution	C	Mn	Si	S	P
Extra low sulphur	0.68 - 0.70	0.60 - 0.65	0.23 - 0.35	0.0035 max	0.015 max
High Mn	0.68 - 0.70	0.66 - 0.80	0.15 - 0.23	0.0035 - 0.014	0.015 max
High Si	0.68 - 0.70	0.60 - 0.65	0.25 - 0.35	0.008 - 0.014	0.015 max

For the extra low sulphur solution, there are relatively few samples. However the result fits mechanisms presented here. This composition may be susceptible to SSC and special precautions like limit on Cu or upper UTS may be required in the long run. The obvious drawback of this steel composition is the increased cost.

The high Mn steel (solution 4) is an outlier from the proposed models, outperforming expectations. It differs from the overall worst performing solution 3 only by carbon content. There were 64 samples, as shown in the orthogonal matrices, and no failures. It seems like this result is fairly reliable and points toward an effect that makes the microstructure more resistant to damage accumulation.

The high Si (solution 6) is well represented in testing. There were 465 samples among all sulphur levels. There were some failures both to HIC and SSC, but the

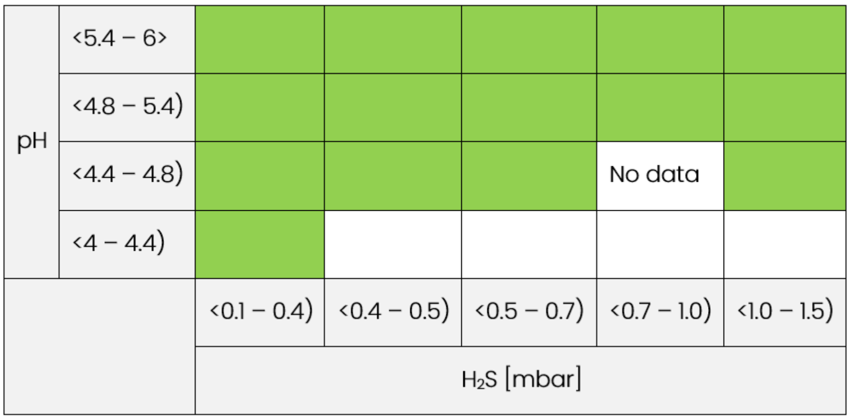

pH	<5.4 – 6>	🟩	🟩	🟩	🟩	🟩
	<4.8 – 5.4)	🟩	🟩	🟩	🟩	🟩
	<4.4 – 4.8)	🟩	🟩	🟩	No data	🟩
	<4 – 4.4)	🟩				
		<0.1 – 0.4)	<0.4 – 0.5)	<0.5 – 0.7)	<0.7 – 1.0)	<1.0 – 1.5)
		H_2S [mbar]				

Figure 8.3: Suitability region of the optimized wires.

projected performance is still satisfactory at below 1 % failures in batch testing.

It can be summarized that the optimized wires are reliable in batch testing within the conditions indicated in Fig. 8.3.

9 Summary and Final Remarks

The MTL-5100 wire is the highest strength and the least expensive wire in the portfolio of the wire grades for use in flexible pipes construction. Based on failure analysis observations and literature a multitude of changes could be employed to improve the wire capability to resist degradation. Patenting of the rod for wire rolling, use of extra low sulphur steel, use of billets processed by electroslag remelting, tempering of the wire after cold rolling... all of which significantly increase the cost. The analysis presented therein revealed a statistical tool for measurement of resistance to failure in batch testing caused by any of the three distinctive mechanisms. It was proven that it is possible to fine tune the chemical composition of the tensile wire to improve its performance, virtually eliminating failure in batch testing, at no additional cost.

It was shown that the cause of seemingly unreliable wire performance is the convoluted nature of corrosion in CO_2 with trace amount of H_2S. At 1 - 1.5 mbar H_2S, the original qualification level, the environment displayed a significant protectiveness against all failure mechanisms.

The statistical analysis was instrumental in understanding the failure mechanisms. Similar analyses were attempted multiple times using different approaches, but the reduction of dimensionality presented in this work was the key for success. There were three critical elements. First, the assumption of Weibull distribution of defects and normalization of failure probability of wires of different sizes and from different suppliers. Second, the test environment aggressiveness maps. Third, was establishing a three-level factorial for sulphur in the design of orthogonal matrix, which was done by inspiration by now forgotten research.

One of the outcomes of the research is a global patent [88]. The premise of the patent is introduction of a sub-micron globular oxide type inclusions to increase of the hydrogen trapping capacity. This is achieved by zirconium and titanium microalloying. The increased trap capacity improves parent and weld SSC resistance.

Within the topic there is still much that could be researched. Effects of the drawing steps and die geometry on damage accumulation to the surface and centreline are especially interesting. It was shown that mechanical property actual UTS strongly influences the wire resistance. This aspect was not addressed in this work. The SSC tests with notched samples in CG HAZ could show the influence of grain boundary carbide networks on SSC propagation. Testing methods indicating failure in situ like Acoustic Emissions could be used to test the mechanisms proposed. There may be other statistical or machine learning models which could give even better results. A Generalized Linear Model or a Neutral Network Model could, for example, indicate an NFP of a wire with an given chemical composition in an given test environment.

Bibliography

[1] IEA, “Net zero by 2050.” http://www.iea.org/reports/net-zero-by-2050, 2021. [Online; accessed 6-January-2023].

[2] R. Nickel and S. Valle, “This decade’s oil boom is moving offshore - way offshore.” https://www.reuters.com/business/energy/this-decades-oil-boom-is-moving-offshore-way-offshore-2022-08-31/. [Online; accessed 28 Feb 2023].

[3] 4Subsea AS, “Un-bonded flexible risers - recent field experience and actions for increased robustness.” https://www.ptil.no/contentassets/c2a5bd00e8214411ad5c4966009d6ade/un-bonded-flexible-risers–recent-field-experience-and-actions–for-increased-robustness.pdf, 2013. [Online; accessed 3-March-2023].

[4] B. Guo, S. Song, A. Ghalambor, and T. R. Lin, “Chapter 10 - introduction to flexible pipelines,” in *Offshore Pipelines (Second Edition)* (B. Guo, S. Song, A. Ghalambor, and T. R. Lin, eds.), pp. 125–132, Boston: Gulf Professional Publishing, second ed., 2014.

[5] API RP 17B Fourth Edition, *Recommended Practice for Flexible Pipe*, 2014.

[6] API 17J Fourth Edition, *Specification for Unbonded Flexible Pipe*, 2014.

[7] API 17L1 Second Edition , *Specification for Ancillary Equipment for Flexible Pipes and Subsea Umbilicals*, 2021.

[8] API RP 17L2 Second Edition, *Recommended Practice for Ancillary Equipment for Flexible Pipes and Subsea Umbilicals*, 2021.

[9] M. Tang, “Flexible pipes,” 2023. DOI: 10.5772/intechopen.109504.

[10] S. Gasc, A. Lambert, A. T. Do, and A. Félix-Henry, "High Strength Tapes Layer Design and Qualification, Reinforcement Solution Against Armor Buckling of Flexible Pipe," Day 4 OTC Offshore Technology Conference, 2016.

[11] L. Zhu, Z. Tan, V. P. P. Nogueira, J. Liu, and J. Clevelario, "Prediction and Qualification of Radial Birdcage and Lateral Buckling of Flexible Pipes in Deepwater Applications," vol. 5A: Pipeline and Riser Technology of *International Conference on Offshore Mechanics and Arctic Engineering*, 05 2015.

[12] C. Saunders and T. O'Sullivan, "Integrity management and life extension of flexible pipe," SPE Offshore Europe Conference and Exhibition, 09 2007. SPE-108982-MS.

[13] Y. Bai, *Deepwater Flexible Risers and Pipelines*. John Wiley & Sons, 2020.

[14] P. J. Simpson and A. J. Lima, "Deepwater Riser Systems - Historical Review and Future Projections," vol. Day 3 Thu of *Offshore Technology Conference Brasil*, 10 2019. D031S030R003.

[15] E. Collings, *Physics of solid solution strengthening*. Springer Science & Business Media, 2012.

[16] W. D. Callister Jr and D. G. Rethwisch, *Fundamentals of materials science and engineering: an integrated approach*. John Wiley & Sons, 2020.

[17] M. Blicharski, *Inżynieria materiałowa: stal*. Wydawnictwa Naukowo-Techniczne, 2014.

[18] H. Bhadeshia and A. Chintha, "Critical assessment 41: the strength of undeformed pearlite," *Materials Science and Technology*, vol. 38, no. 16, pp. 1291–1299, 2022.

[19] F. B. Pickering, "High strength low alloy steels," *Materials Science and Technology*, 2006.

[20] H. K. D. H. Bhadeshia, "Cementite," *International Materials Reviews*, vol. 65, no. 1, pp. 1–27, 2020.

[21] B. J. Duckfield, "The Cold Drawing of Carbon Steel Wire," *Wire Industry*, vol. 38, 1971.

[22] M. Umemoto, Y. Todaka, and K. Tsuchiya, "Mechanical properties of cementite and fabrication of artificial pearlite," *Materials Science Forum*, vol. 426-432, pp. 859–864, 08 2003.

[23] E. Lokere and S. Vanneste, "Flat high-tensile wire for hose reinforcement," 2004. European patent EP1596114A1.

[24] J. A. Pero-Sanz Elorz, D. Fernández González, L. F. Verdeja, J. A. Pero-Sanz Elorz, D. Fernández González, and L. F. Verdeja, "Fe–C system. stable and metastable equilibrium diagrams," *Physical Metallurgy of Cast Irons*, pp. 1–18, 2018.

[25] T. Tran, B. Brown, and S. Nešic, "Corrosion of mild steel in an aqueous CO_2 environment–basic electrochemical mechanisms revisited," in *CORROSION 2015*, OnePetro, 2015.

[26] A. Kahyarian, B. Brown, and S. Nešic, "Mechanism of CO_2 corrosion of mild steel: A new narrative," in *CORROSION 2018*, OnePetro, 2018.

[27] A. Kahyarian and S. Nešic, "A new narrative for CO_2 corrosion of mild steel," *Journal of the Electrochemical Society*, vol. 166, no. 11, p. C3048, 2019.

[28] D. M. Kern, "The hydration of carbon dioxide," *Journal of Chemical Education*, vol. 37, no. 1, p. 14, 1960.

[29] R. Nyborg, "Overview of $\mathrm{CO_2}$ Corrosion Models for Wells and Pipelines," NACE Corrosion Conference, 04 2002. NACE-02233.

[30] A. Kahyarian, M. Singer, and S. Nešic, "Modeling of uniform $\mathrm{CO_2}$ corrosion of mild steel in gas transportation systems: A review," *Journal of Natural Gas Science and Engineering*, vol. 29, pp. 530–549, 2016.

[31] S. Nešic, J. Postlethwaite, and M. Vrhovac, "$\mathrm{CO_2}$ corrosion of carbon steel - from mechanistic to empirical modelling," *Corrosion Reviews*, vol. 15, no. 1-2, pp. 211–240, 1997.

[32] NACE SP0110, *Wet Gas Internal Corrosion Direct Assessment Methodology for Pipelines*, 2018. NACE International.

[33] Kun-Lin J. Lee, *A Mechanistic Moceling of CO_2 Corrosion of Mild Steel in the Presence of H_2S.* PhD thesis, Ohio University, 2004.

[34] R. Feng, J. Beck, D. Hall, A. Buyuksagis, M. Ziomek-Moroz, and S. Lvov, "Effects of CO_2 and H_2S on corrosion of martensitic steels in brines at low temperature," *CORROSION*, vol. 74, 10 2017.

[35] W. Sun and S. Nešic, "A mechanistic model of uniform hydrogen sulfide/carbon dioxide corrosion of mild steel," *Corrosion*, vol. 65, no. 5, pp. 291–307, 2009.

[36] R. Oriani, "The diffusion and trapping of hydrogen in steel," *Acta Metallurgica*, pp. 18(1):147–157, 1970.

[37] G. Pressouyre, "Trap theory of hydrogen embrittlement," *Acta Metallurgica*, vol. 28, no. 7, pp. 895–911, 1980.

[38] O. Barrera, D. Bombac, Y. Chen, T. Daff, E. Galindo-Nava, P. Gong, D. Haley, R. Horton, I. Katzarov, J. Kermode, *et al.*, "Understanding and mitigating hydrogen embrittlement of steels: a review of experimental, modelling and design progress from atomistic to continuum," *Journal of materials science*, vol. 53, no. 9, pp. 6251–6290, 2018.

[39] I. M. Robertson, P. Sofronis, A. Nagao, M. Martin, S. Wang, D. Gross, and K. Nygren, "Hydrogen embrittlement understood," *Metallurgical and Materials Transactions A*, vol. 46, pp. 2323–2341, 2015.

[40] M. Iannuzzi, "Is sulfide stress cracking an anodic or a cathodic process?," 05 2017. doi 10.31224/osf.io/329du.

[41] Y. Yamane, "Effect of Ni on sulfide stress corrosion cracking in low alloy steels," *Corrosion 86/167, NACE, Houston, TX*, 1987.

[42] ASTM A203, *Standard Specification for Pressure Vessel Plates, Alloy Steel, Nickel*, 2017.

[43] T. Herrmann, C. Bosch, and J. Martin, "HIC assessment of low alloy steel line pipe for sour service application-literature survey," *3R International. Rohre. Rohrleitungsbau. Rohrleitungssysteme*, vol. 44, 2005.

[44] NACE SP0110, *Laboratory Testing of Metals for Resistance to Sulfide Stress Cracking and Stress Corrosion Cracking in H_2S Environments*, 2016.

[45] W. Dietzel, P. B. Srinivasan, and A. Atrens, "Chapter: Testing and evaluation methods for stress corrosion cracking (SCC) in metals," in *Stress Corrosion Cracking*, pp. 133–166, Elsevier, 2011.

[46] P. L. Andresen, "IGSCC crack propagation rate measurement in BWR environments. executive summary of a round robin study," 1998.

[47] V. Raja and T. Shoji, *Stress corrosion cracking: theory and practice*. Elsevier, 2011.

[48] S. Eliassen and L. Smith, *Guidelines on Materials Requirements for Carbon and Low Alloy Steels For H_2S-Containing Environments in Oil and Gas Production*, July 2009.

[49] NACE TM0316, *Four-Point Bend Testing of Materials for Oil and Gas Applications*, 2016.

[50] M. D. Deffo Ayagou, G. R. Joshi, B. Tribollet, T. T. Mai Tran, C. Mendibide, and J. Kittel, "Corrosion and hydrogen permeation of low alloy steel in H_2S-containing environments : the effect of test buffer solution chemistry," in *Eurocorr 2019 Conference*, (Seville, Spain), Sept. 2019.

[51] C. Pressouyre, "Current solutions to hydrogen problems in steel," *Proceedings of the First International Conference on Current Solutions to Hydrogen Problems in Steels, Washington DC, November 1-5, 1982*, pp. 18–34.

[52] E. Ura-Bińczyk, A. Dobkowska, M. Płocińska, T. Płociński, B. Adamczyk-Cieślak, B. Mazurkiewicz, W. Solarski, J. Banaś, and J. Mizera, "The influence of grain refinement on the corrosion rate of carbon steels in fracturing fluids used in shale gas production," *Materials and Corrosion*, vol. 68, no. 11, pp. 1190–1199, 2017.

[53] H. Jeng, L. Chiu, D. Johnson, and J. Wu, "Effect of pearlite morphology on hydrogen permeation, diffusion, and solubility in carbon steels," *Metallurgical Transactions A*, vol. 21, pp. 3257–3259, 1990.

[54] E. S. Skilbred, M. Kappes, M. Iannuzzi, and R. Johnsen, "Hydrogen uptake and diffusivity in steel armor wires with different chemical composition, carbide dis-

tribution, grain size, and degree of deformation," *Materials and Corrosion*, vol. 73, no. 3, pp. 326–345, 2022.

[55] R. Ueji, Y. Kimura, and T. Inoue, "Preferable resistance against hydrogen embrittlement of pearlitic steel deformed by caliber rolling," *ISIJ International*, vol. 62, no. 2, pp. 368–376, 2022.

[56] D. Langstaff, G. Meyrick, and J. Hirth, "Hydrogen induced delayed failure of high strength alloy steel wires," *Corrosion*, vol. 37, no. 8, pp. 429–437, 1981.

[57] J. Toribio and E. Ovejero, "Effect of cold drawing on microstructure and corrosion performance of high-strength steel," *Mechanics of Time-Dependent Materials*, vol. 1, pp. 307–319, 1997.

[58] NACE MR0175/ISO 15156, *Petroleum and natural gas industries – Materials for use in* H_2S*-containing environments in oil and gas production – Fourth Edition*, 2021.

[59] R. J. Pargeter, "A review of the concept of mildly sour environments," in *International Pipeline Conference*, vol. 40221, pp. 447–457, American Society of Mechanical Engineers, 1998.

[60] J. Koo, M. Luton, N. Bangaru, R. Petkovic, D. Fairchild, C. Petersen, H. Asahi, T. Hara, Y. Terada, M. Sugiyama, *et al.*, "Metallurgical design of ultra high-strength steels for gas pipelines," *International Journal of Offshore and Polar Engineering*, vol. 14, no. 01, 2004.

[61] D. Sponseller, R. Garber, and T. Cox, "Design of H_2S-resistant steels for the tubular products used in oil nad gas wells." Proceedings of the First International Conference on Current Solutions to Hydrogen Problems in Steels, Washington DC, November 1-5, 1982.

[62] C. Mendibide and T. Sourmail, "Composition optimization of high-strength steels for sulfide stress cracking resistance improvement," *Corrosion Science*, vol. 51, no. 12, pp. 2878–2884, 2009.

[63] C. D. Kantner, *Designing strength, toughness, and hydrogen resistance: quantum steel*. PhD thesis, Northwestern University, 2002.

[64] J. Herng-Jeng, "Lower-cost, ultra-high-strength, high-toughness steel," 2010. US Patent US20100230015.

[65] F. Dong, J. Venezuela, H. Li, Z. Shi, Q. Zhou, L. Chen, J. Chen, L. Du, and A. Atrens, "The influence of phosphorus on the temper embrittlement and hydrogen embrittlement of some dual-phase steels," *Materials Science and Engineering: A*, vol. 854, p. 143379, 2022.

[66] K. Yoshino and C. McMahon, "The cooperative relation between temper embrittlement and hydrogen embrittlement in a high strength steel," *Metallurgical and Materials Transactions B*, vol. 5, pp. 363–370, 1974.

[67] M. Nagumo *et al.*, *Fundamentals of hydrogen embrittlement*, vol. 921. Springer, 2016.

[68] S. Bechtle, M. Kumar, B. Somerday, M. Launey, and R. Ritchie, "Grain-boundary engineering markedly reduces susceptibility to intergranular hydrogen embrittlement in metallic materials," *Acta Materialia*, vol. 57, no. 14, pp. 4148–4157, 2009.

[69] M. A. Gibson and C. A. Schuh, "Segregation-induced changes in grain boundary cohesion and embrittlement in binary alloys," *Acta Materialia*, vol. 95, pp. 145–155, 2015.

[70] S. Kulkov, A. Bakulin, and S. Kulkova, "Effect of boron on the hydrogen-induced grain boundary embrittlement in α-fe," *International Journal of Hydrogen Energy*, vol. 43, 12 2017.

[71] H. L. Mai, X.-Y. Cui, D. Scheiber, L. Romaner, and S. P. Ringer, "The segregation of transition metals to iron grain boundaries and their effects on cohesion," *Acta Materialia*, vol. 231, p. 117902, 2022.

[72] A. S. Kholtobina, W. Ecker, R. Pippan, and V. I. Razumovskiy, "Effect of alloying elements on hydrogen enhanced decohesion in bcc iron," *Computational Materials Science*, vol. 188, p. 110215, 2021.

[73] D. Zipperian, "PACE technologies metallographic handbook," *PACE Technologies, US*, p. 180, 2011.

[74] J. Stewart, J. Charles, and E. Wallach, "Iron-phosphorus-carbon system: Part 2 - metallographic behaviour of Oberhoffer′s reagent," *Materials Science and Technology*, vol. 16, pp. 283–290, 03 2000.

[75] ASTM E45, *Standard Test Methods for Determining the Inclusion Content of Steel*, 2018.

[76] ISO 4967, *Steel - Determination of content of nonmetallic inclusions - Micrographic method using standard diagrams - Third Edition*, 2013.

[77] L. Kukołowicz and D. Oleszak, "Influence of anisotropy of mechanical properties on hydrogen induced cracking," Ochrona Przed Korozją, February 2023. doi 10.15199/40.2023.2.1.

[78] A. Vancostenoble, C. Duret-Thual, C. Bosch, and D. Delafosse, "Stress corrosion cracking of ferrito-pearlitic steel in aqueous environment containing dissolved $CO_2$2," in *CORROSION 2014*, OnePetro, 2014.

[79] D. Enos and J. Scully, "A critical-strain criterion for hydrogen embrittlement of cold-drawn, ultrafine pearlitic steel," *Metallurgical and Materials Transactions A*, vol. 33, pp. 1151–1166, 2002.

[80] Y. Ogawa, H. Nishida, M. Nakamura, V. Olden, A. Vinogradov, and H. Matsunaga, "Dual roles of pearlite microstructure to interfere/facilitate gaseous hydrogen-assisted fatigue crack growth in plain carbon steels," *International Journal of Fatigue*, vol. 154, p. 106561, 2022.

[81] A. Duval and M. Robinson, "Measurement and prediction of hydrogen embrittlement in high strength carbon steel," *Corrosion engineering, science and technology*, vol. 44, no. 5, pp. 340–346, 2009.

[82] EN, BS 843-5, "Advanced technical ceramics–mechanical properties of monolithic ceramics at room temperature. part 5: Statistical analysis.,"

[83] H. Kihira, S. Ito, and T. Murata, "The behavior of phosphorous during passivation of weathering steel by protective patina formation," *Corrosion Science*, vol. 31, pp. 383–388, 1990.

[84] T. R. Bement, "Taguchi techniques for quality engineering," 1989.

[85] D. Shainin and P. Shainin, “Better than taguchi orthogonal tables,” *Quality and Reliability Engineering International*, vol. 4, no. 2, pp. 143–149, 1988.

[86] M. Kubat and J. Kubat, *An introduction to machine learning*, vol. 2. Springer, 2017.

[87] N. Desamais and C. Taravel-Condat, “On the beneficial influence of a very low supply of H_2S on the hydrogen embrittlement resistance of carbon steel wires in flexible pipe annulus,” in *Offshore Technology Conference*, OnePetro, 2009.

[88] L. Kukolowicz, *Steel Wire*. Patent, published under EP3674425B1 and US 2022/0074033 A1, 2022.

Appendix A

ŁUKASZ KUKOŁOWICZ[1, 2, *]
ORCID: 0000-0002-9984-8700

DARIUSZ OLESZAK[2]
ORCID: 0000-0002-7563-007X

[1] Baker Hughes, al. Krakowska 110/114, 02-256 Warsaw, Poland

[2] Warsaw University of Technology, Faculty of Materials Science and Engineering, Wołoska 141, 02-507 Warsaw, Poland

* Corresponding author

DOI: 10.15199/40.2023.2.1

Influence of anisotropy of mechanical properties on hydrogen induced cracking

Wpływ anizotropii właściwości mechanicznych na podatność na pękanie wodorowe

Hydrogen induced cracking is a form of wet H_2S cracking. Blistering or crack propagation is a result of the mechanical tearing of material by high-pressure hydrogen gas forming on internal material discontinuities, like non-metallic inclusions. This failure mechanism is typically associated with low and medium-strength pipeline steels, however, it does also occur in high-strength rolled wire. This evaluation aims to elucidate the mechanism of this susceptibility. The characteristic failure pattern where cracking occurs near the wire centreline and propagates perpendicular to the rolling direction leads to believe that the wire anisotropy, developed during cold rolling, plays a critical role. A mechanical property – flow resistance in principal directions – was measured using the Wheeler and Ireland technique. It was found that the "weak" direction is perpendicular to the crack propagation direction. The failure rate does not correspond to the flow resistance, but rather to the flow resistance ratios. It is proposed that those ratios are not only a measure of anisotropy but also a measure of microstructural damage inflicted by the cold rolling process. This microstructural damage is partially reversible by heat treatment processes.

Keywords: hydrogen induced cracking, flow resistance, anisotropy, cold rolled wire

Pękanie wodorowe jest mechanizmem degradacji często zachodzącym w środowiskach korozyjnych, w których występuje siarkowodór. Propagacja pęknięć postępuje na skutek fizycznego rozrywania materiału przez cząsteczkowy wodór pod wysokim ciśnieniem, tworzący się na nieciągłościach wewnętrznych, takich jak na przykład wtrącenia niemetaliczne. Praca badawcza dotyczy mechanizmu pękania wysoko wytrzymałego kształtowego drutu stalowego. Drut pęka w charakterystyczny sposób: pęknięcie tworzy się w pobliżu środka drutu i propaguje równolegle do płaskich powierzchni. Obserwacja ta każe przypuszczać, że propagacja związana jest z anizotropią właściwości mechanicznych drutu. Anizotropię zbadano jako opór płynięcia plastycznego materiału pod wgłębnikiem twardościomierza metodą Wheelera i Irelanda. Zaobserwowano, że pęknięcia propagują prostopadle do kierunku, w którym występuje najmniejszy opór płynięcia. Pękanie podczas testów w środowisku korozyjnym z siarkowodorem nie jest skorelowane bezpośrednio z oporem płynięcia, a ze stosunkiem oporów płynięcia w dwu kierunkach, a więc miarą anizotropii. Z badań wynika, że proces walcowania na zimno powoduje uszkodzenia mikrostruktury, które można szacować miarą anizotropii właściwości mechanicznych drutu i które są częściowo odwracalne w procesie obróbki cieplnej.

Słowa kluczowe: kolumna destylacji atmosferycznej ropy naftowej, korozja górnej części kolumny atmosferycznej, hydroliza chlorków organicznych i nieorganicznych

1. Introduction

Rolled wire is used, among others, in the construction of unbonded flexible pipe to API 17J [1] standard used for subsea and offshore developments. The flattened shape allows for tighter packing of steel layers. In this application corrosive gasses, including H_2S, can diffuse through a polymer barrier. As such, the standard requires a wire resistant to degradation mechanisms caused by this environment, in particular, to Hydrogen Induced Cracking (HIC) and Sulphide Stress Cracking (SSC). This investigation focuses on Cold Rolled (CR) wires which failed sour

Łukasz Kukołowicz, MSc Eng. Graduate from the Faculty of Materials Science and Engineering of the Warsaw University of Technology. Since 2011 employee of GE O&G, now after the merger Baker Hughes. Main areas of interest are corrosion and hydrogen embrittlement of metallic materials, large forgings, failure analysis with over 90 analyses carried out to date. The topic of the PhD work is an analysis of the sour service test failures of the cold rolled wires.
E-mail: lukasz.kukolowicz.dokt@pw.edu.pl, lukasz.kukolowicz@bakerhughes.com

Dariusz Oleszak, DSc, PhD, Eng., Professor at the Faculty of Materials Science and Engineering, WUT. Research area includes manufacturing, microstructure and properties of metallic materials.
E-mail: dariusz.oleszak@pw.edu.pl

■ Otrzymano / Received: 28.11.2022. Przyjęto / Accepted: 23.01.2023

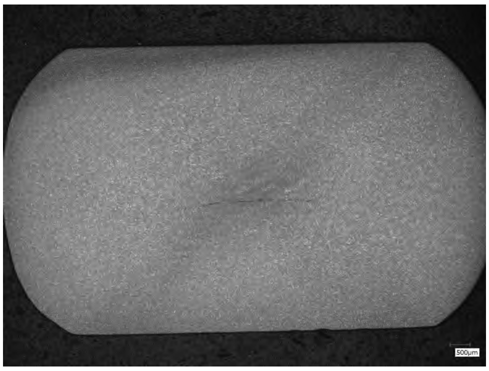

Fig. 1. An example of wire cross-section etched with Nital with a HIC near the centreline. Etching reveals a "X" pattern near diagonals related to plastic deformation during the cold rolling process

Rys. 1. Przykładowy zgład ujawniający pęknięcie wodorowe w pobliżu osi drutu, trawiony Nitalem. Trawienie ujawnia wzór „X" między przekątnymi profilu, związany z procesem walcowania na zimno

testing by HIC. HIC is typically associated with low-strength pipeline steels and it seldomly occurs for X80 and higher-strength pipeline steels with UTS above 700 MPa. ASM Handbook [2] defines it as "the cracking in low-to medium-strength steels in the absence of applied stress where the driving force for crack propagation is molecular hydrogen pressure build-up within the crack". High strength steels are naturally more resistant to this degradation mechanism. In rolled wires, HIC occurs near the centreline and propagates perpendicular to the wire width as shown in Fig. 1. This pattern indicates the existence of an easy crack propagation path.

Majority of the publications on the flexible pipe wires focus on a corrosion behaviour primarily iron supersaturation and H_2S consumption [3]. When testing is performed in conditions replicating the annulus, there is a beneficial effect of very low H_2S additions reducing the corrosion rate [4, 5], as compared to pure CO_2. However, the acetic ions present in NACE TM0177 solution B prevent formation of the protective scale thus the acceptance testing is much more aggressive than the field conditions.

The flow surface was determined by the technique by Lee and Backofen [6], based on Wheeler and Ireland approach [7, 8]. The technique analyses the stress state under the indent as a sum of hydrostatic pressure and shear stress. The deviatoric stresses are defined as:

$$s_1 = \sigma_1 - \sigma,$$
$$s_2 = \sigma_2 - \sigma,$$
$$s_3 = \sigma_3 - \sigma, \tag{1}$$

where σ_1, σ_2, σ_3 are the principal stress and σ is the hydrostatic stress given as (2):

$$\sigma = \frac{1}{3}(\sigma_1 + \sigma_2 + \sigma_3). \tag{2}$$

For plane strain conditions Huber-Mises-Hencky hypothesis correlates flow surface to the stress state as (3):

$$KHN \approx ({\sigma_1}^2 - \sigma_1\sigma_2 + {\sigma_2}^2)^{\frac{1}{2}}. \tag{3}$$

This can be transposed to (4):

$$\sigma_i \approx KHN \cdot (1 - \alpha_i + {\alpha_i}^2)^{-\frac{1}{2}}. \tag{4}$$

The material flow surface is constructed from the six KHN values obtained from the indentations made along two directions of each of the three orthogonal planes of material's principal axes. The weights α, depend on the indentation diagonals ratio δ. For the Knoop indent it is approximately 7 : 1. The values of α for each indent orientation a–f and are given as (5):

$$\alpha_a = \frac{\sigma_2}{\sigma_1} = (2+\delta)/(2\delta+1),$$
$$\alpha_b = \frac{1}{\alpha_a},$$
$$\alpha_c = (1-\delta)(2+\delta),$$
$$\alpha_d = (\delta-1)(1+2\delta),$$
$$\alpha_e = \frac{1}{\alpha_d},$$
$$\alpha_f = \frac{1}{\alpha_c}. \tag{5}$$

Each indent on the flow surface has two coordinates $[[KHN \cdot (1-\alpha_i+{\alpha_i}^2)^{-\frac{1}{2}};\ \alpha_i \cdot KHN \cdot (1-\alpha_i+{\alpha_i}^2)^{-\frac{1}{2}}]$. Determination of the plastic flow properties in Z-Y plane was achieved by rotation. In practical terms the new order of indents is d, c, b, a, f, e.

2. Experimental procedures

2.1. Material

The wires for this evaluation were high-carbon steels. Among the 16 samples tested (A–P) there were three wire grades:

– SR: 861–1034 MPa UTS cold rolled and stress relieved 0.60–0.65% C (3 samples),
– TE: 1310–1482 MPa UTS cold rolled and tempered 0.65–0.75% C (1 sample),
– CR: 1310–1482 MPa UTS cold rolled 0.60–0.70% C (12 samples).

Cold rolling of hot rolled wire with ultrafine pearlitic microstructure was carried out in a way that the total reduction of wire cross-section was about 50% for all wire grades. The wire profile final dimensions varied from 9 × 3 to 12 × 7 mm. The stress-relieving process was carried out in a hydrogen protective atmosphere at about 400°C for a few hours. The wire grade TE was subject to a rapid recovery heat treatment [9]. The recovery heat treatment consisted of rapid heating to above 600°C, hold time was below 5 seconds, and was followed by rapid cooling.

2.2. General microstructure evaluation

The general microstructure of tensile wire was revealed by etching with 5% ammonium persulfate $(NH_4)_2S_2O_8$ with addition of 0.05% EDTA in water. Etching time 5–20 seconds. Observations were carried out using Leica DM4000 M LED at 500× optical magnification.

2.3. Experimental procedure

Samples were prepared by cutting each wire sample in three perpendicular planes intersecting the wire centreline, mounting in resin, grounding, and polishing. Knoop hardness was measured using LECO LV 700AT at 10 kG load in 6 orientations marked 'a' to 'f'. The cutting plan, indentation orientations, and markings are shown in Fig. 2.

Two indentations were performed in each of the six orientations. The average of the two was subsequently used for the calculation of points along the KHN flow resistance surface. An example of the flow resistance surface representation of sample P is shown in Fig. 3.

2.4. Sour service testing

Tests consisted of 30-day immersion testing of five samples pre-stressed by four points bending to 0.5% total elongation in outer fibres. The testing solution was NACE TM0177 modified to contain 3.5% NaCl, saturated and continuously bubbled with a gas mixture of H_2S and CO_2 at atmospheric pressure. The partial pressure of H_2S within the gas mixture was up to 1 mbar. After the test samples were subject to a visual and magnetic particle inspection, followed by ultrasonic testing and microscopic inspection of sectioned wire.

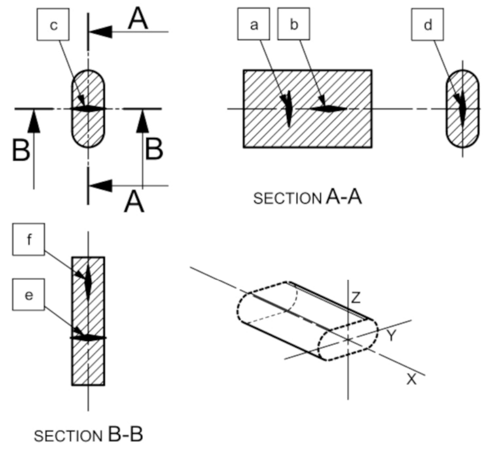

Fig. 2. Wire-cutting plans and Knoop indentation orientations (letters in boxes indicate the indent identification letter); principal axis naming is shown in the isometric view

Rys. 2. Plan cięcia i orientacje wgłębnika (oznaczone literami w prostokątach); główne kierunki zaznaczono w rzucie izometrycznym

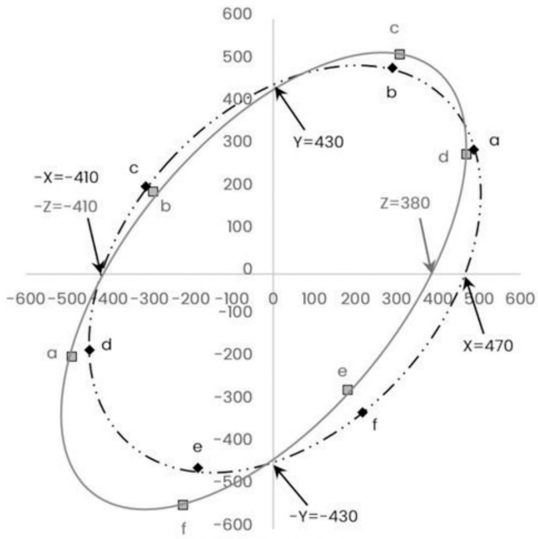

Fig. 3. Plane intersections of the flow resistance surface of sample P: black – intersection with the X-Y plane, grey – intersection with the Z-Y plane; the values of the flow resistance in the principal directions are the intersection points with the coordinate system axis

Rys. 3. Przecięcie powierzchni oporu plastycznego płynięcia z płaszczyznami dla próbki P: czarna przerywana linia – przecięcie z płaszczyzną X-Y, szara ciągła linia – przecięcie z płaszczyzną Z-Y; wartości oporu plastycznego płynięcia w głównych kierunkach oznaczono jako punkty przecięcia z osiami układu współrzędnych

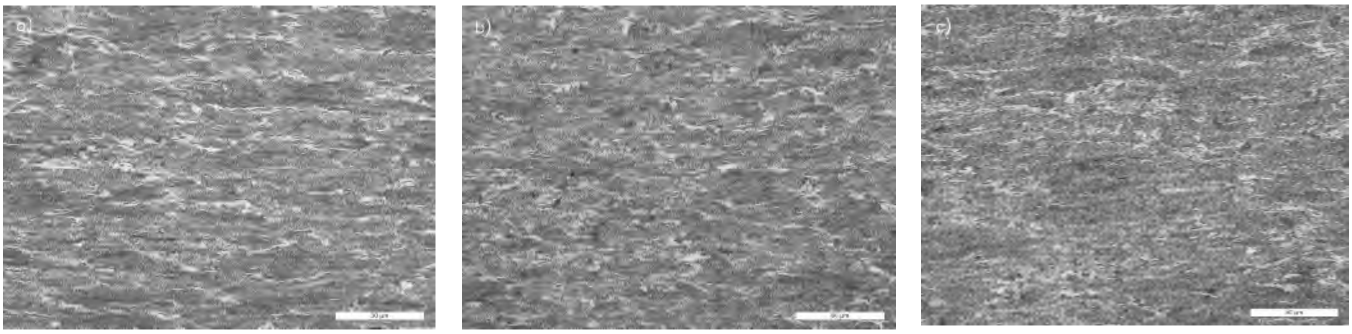

Fig. 4. General microstructure of wire grade SR: a) microstructure in Z-X plane, ¼ wire thickness above the centreline; b) microstructure in Y-Z plane, ¼ wire thickness above the centreline; c) microstructure in Z-X plane, near the centreline

Rys. 4. Mikrostruktura drutu SR: a) mikrostruktura w płaszczyźnie Z-X, ¼ grubości drutu nad osią drutu; b) mikrostruktura w płaszczyźnie Y-Z, ¼ grubości drutu nad osią drutu; c) mikrostruktura w płaszczyźnie Y-Z, w osi drutu

2.5. Microstructure evaluation of centreline segregation

A retrospective microstructure analysis was carried out to determine the source of the measurement error inconsistency. The following etching procedure was used to reveal centreline segregation in CR wire grade:

1. Electrolytic etch in 20% KOH saturated with picric acid at 8V for 40 s.
2. 0.5% Nital 3–5 s.
3. 40 ml glycerin (waterless), 3 ml HNO_3, 6 ml HF 5–10 s.

For SR and TE wire grades using the third step of the procedure was sufficient. Additional microhardness tests at 300 gf load were carried out using a Zwick ZHVμ hardness tester.

3. Results

3.1. General microstructure

The microstructure of sample A is representative for wire grade SR. The microstructure is pearlitic-ferritic with partial spheroidization of pearlite. The grains are axially elongated as shown in Fig. 4a. The microstructure is deformed also in the width direction. The deformation in the centreline is greater that in ¼ thickness location as shown in Fig. 4c and 4b, respectively.

The microstructure of sample D, wire grade TE consists of fine partially spheroidized pearlite. The elongation along the wire axis is evidenced in Fig. 5a. Width wise deformation of grains is relatively small in ¼ thickness location but becomes evident near the centreline as shown in Fig. 5b and 5c, respectively.

The microstructure of sample L, representative of wire grade CR consists of fine pearlite and allotriomorphic ferrite. The elongation along the wire axis is evidenced in Fig. 6a. Width wise deformation of grains is negligible in ¼ thickness location but becomes evident near the centreline as shown in Fig. 6b and 6c, respectively. A part of the centreline segregation region with lower deformation and with reduced ferrite content is visible at the top of the later picture.

3.2. Hardness measurement error

The measurement error was normalized by expressing each measurement error as a percentage deviation from the average KHN hardness measured for each wire sample and each orientation. The standard deviation of normalized measurements was calculated for each indent orientation. The standard deviation was multiplied by the *t*-Student value for 95% confidence and presented in Table 1 as the measurement error.

It was found that a significant measurement error was observed for indent orientation d. The etching of samples after indentation revealed a dark etching region interpreted as a centreline segregation from the continuous casting process. In some samples,

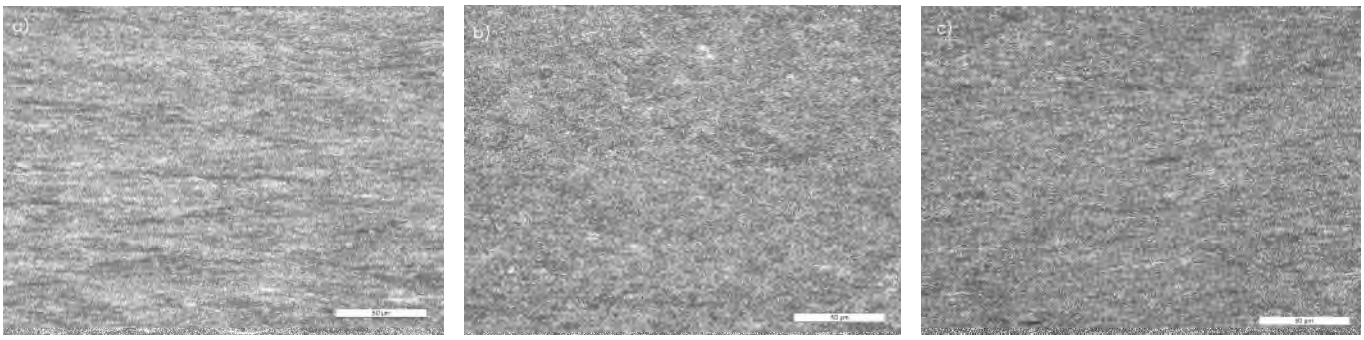

Fig. 5. General microstructure of wire grade TE: a) microstructure in Z-X plane, ¼ wire thickness above the centreline; b) microstructure in Y-Z plane, ¼ wire thickness above the centreline; c) microstructure in Z-X plane, near the centreline

Rys. 5. Mikrostruktura drutu TE: a) mikrostruktura w płaszczyźnie Z-X, ¼ grubości drutu nad osią drutu; b) mikrostruktura w płaszczyźnie Y-Z, ¼ grubości drutu nad osią drutu; c) mikrostruktura w płaszczyźnie Y-Z, w osi drutu

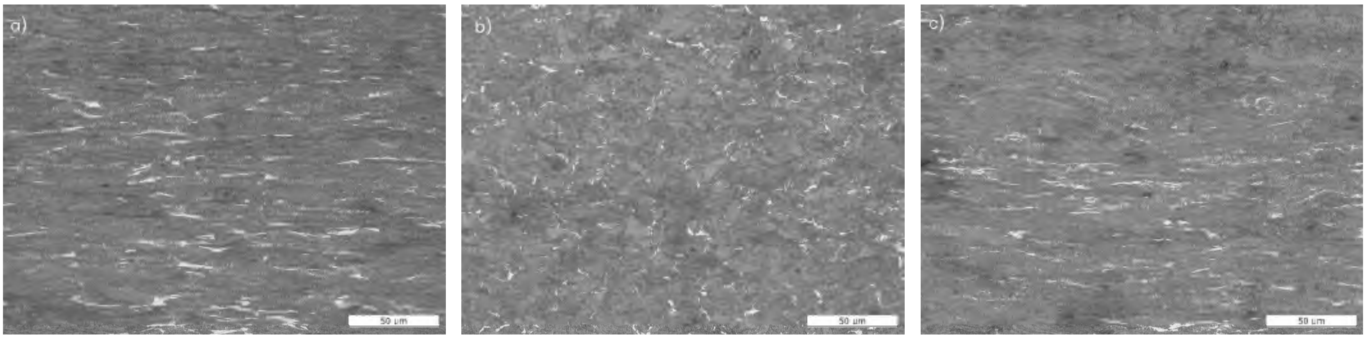

Fig. 6. General microstructure of wire grade CR: a) microstructure in Z-X plane, ¼ wire thickness above the centreline; b) microstructure in Y-Z plane, ¼ wire thickness above the centreline; c) microstructure in Z-X plane, near the centreline

Rys. 6. Mikrostruktura drutu CR: a) mikrostruktura w płaszczyźnie Z-X, ¼ grubości drutu nad osią drutu; b) mikrostruktura w płaszczyźnie Y-Z, ¼ grubości drutu nad osią drutu; c) mikrostruktura w płaszczyźnie Y-Z, w osi drutu

Table 1. Normalized measurement error for Knoop hardness in each orientation
Tabela 1. Znormalizowany błąd pomiaru twardości Knoopa dla każdej orientacji wgłębnika

Orientation	a	b	c	d	e	f
Measurement error [%]	±1.0	±1.3	±1.3	±4.3	±1.7	±0.8

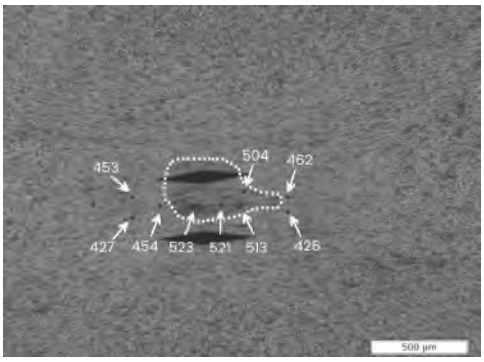

Fig. 7. Microstructure evaluation of sample P (the centreline segregation is outlined in white dotted line); Knoop indents are in orientation d; microhardness survey shows Vickers HV0.3 results

Rys. 7. Mikrostruktura próbki P trawiona w celu ujawnienia segregacji powstałej podczas odlewania (obszar segregacji zakreślono białą kropkowaną linią); odciski twardości Knoopa w orientacji d; na rysunek naniesiono wyniki pomiarów mikrotwardości HV0.3

Table 2. Summary of flow resistance in tension and compression in principal directions and failure rate in a sour test
Tabela 2. Zestawienie wyników oporu plastycznego płynięcia w głównych kierunkach rozciągania i ściskania

Sample ID	Grade	Size [mm]	X [KHN]	–X [KHN]	Y [KHN]	–Y [KHN]	Z [KHN]	–Z [KHN]	Failure rate
A	SR	9 × 3	320	–300	320	–320	290	–300	0
B	SR	12 × 4	320	–300	310	–310	290	–300	0
C	SR	12 × 4	310	–300	320	–320	280	–300	0
D	TE	12 × 7	400	–400	400	–400	380	–400	0
E	CR	9 × 3	440	–440	460	–430	340	–390	1.0
F	CR	10 × 5	460	–380	400	–450	360	–400	0.2
G	CR	10 × 5	480	–420	410	–410	370	–370	0.6
H	CR	10 × 5	430	–400	400	–400	340	–360	0.2
I	CR	12 × 4	420	–380	420	–370	330	–400	0.4
J	CR	12 × 6	460	–440	440	–440	360	–440	0.6
K	CR	12 × 6	480	–420	420	–420	380	–400	0.2
L	CR	12 × 6	460	–420	415	–460	415	–415	0.0
M	CR	12 × 7	420	–390	400	–390	380	–410	0.2
N	CR	12 × 7	480	–420	440	–420	370	–420	0.4
O	CR	12 × 7	500	–420	440	–440	360	–430	0.8
P	CR	12 × 7	470	–410	430	–430	380	–410	0.6

the segregation region was off-centre and did not interfere with Knoop hardness indents. An example of microstructure in sample P is shown in a photograph in Fig. 7. The centreline segregation was outlined in magenta for visibility and was about 500 µm wide and 300 µm high. Microhardness evaluation showed elevated hardness within this region, up to 523 HV10, compared to 426–462 HV10 in the microstructural region adjacent to it.

3.3. Flow resistance and sour service performance

The flow resistance in tension and compression in primary directions is summarized in Table 2 along with a normalized

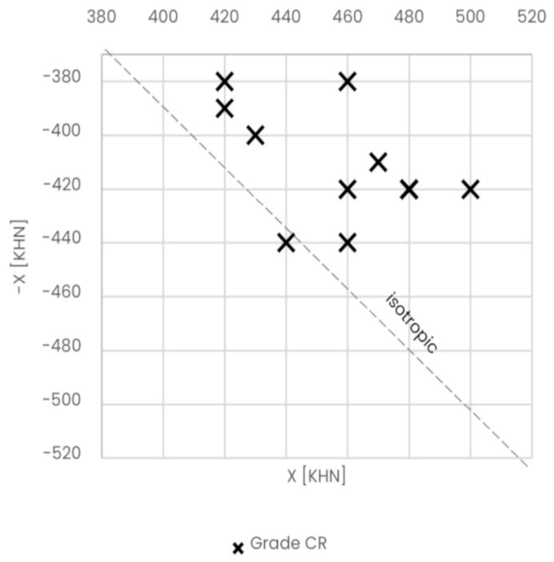

Fig. 8. Plot of the flow resistance X and –X for grade CR

Rys. 8. Wykres oporu plastycznego płynięcia w kierunku X: rozciągania (X) i ściskania (–X) dla drutu CR

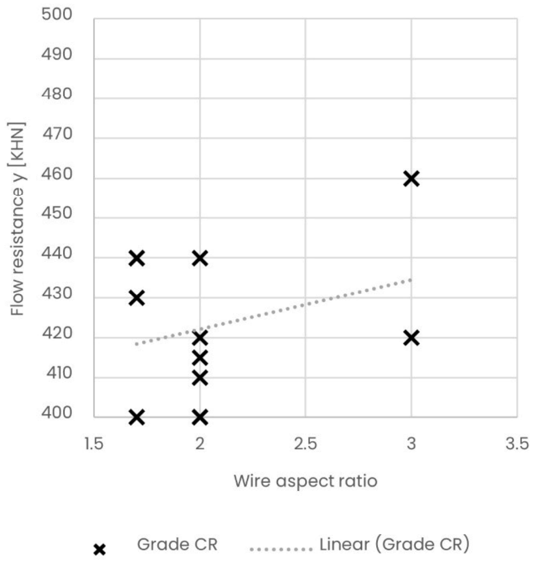

Fig. 10. Plot of the flow resistance Y and the wire aspect ratio – the flow resistance appears to increase with the increasing wire aspect ratio

Rys. 10. Opór plastycznego płynięcia i kierunku Y wykazuje korelację z proporcjami przekroju drutu

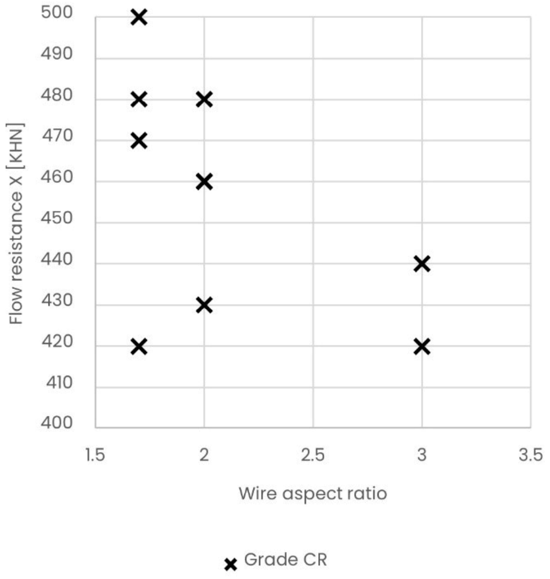

Fig. 9. Plot of the flow resistance X and the wire aspect ratio – no correlation between the two variables

Rys. 9. Opór plastycznego płynięcia i kierunku X nie wykazuje korelacji z proporcjami przekroju drutu

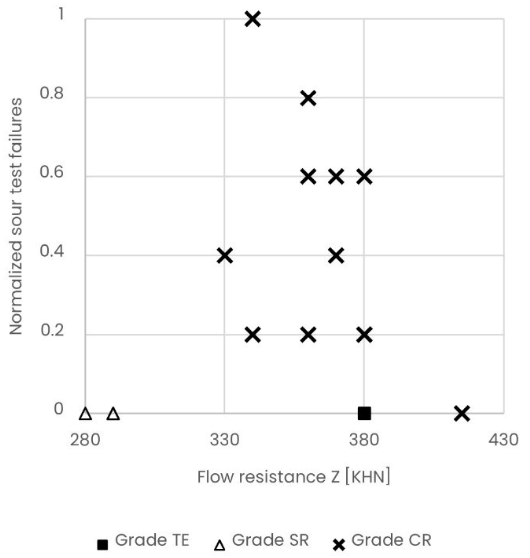

Fig. 11. Plot of the flow resistance Z and the normalized sour test result showing no correlation for the CR grade wire

Rys. 11. Opór plastycznego płynięcia i kierunku Z nie wykazuje korelacji ze znormalizowanym wynikiem testów korozyjnych drutu CR

sample failure rate. In the convention of this paper, compression is indicated by a minus sign. All sour test failures were caused by HIC.

All wire grades were shown to be anisotropic. It was found that flow resistance in the Z direction is the lowest for all wires. Wire grade TE was the least anisotropic showing 5% lower flow resistance in the Z direction than in the X direction, 380 and 400 KHN respectively. For wire SR the average flow resistance in the Z direction is 287 KHN, while the average flow resistance in the X direction is 317 KHN; a 10% reduction. For grade CR the average flow resistance in the Z direction was 366 KHN, while the average in the X direction was 460 KHN; a 20% reduction.

The flow resistance in the X direction should correspond to the tensile strength limits for the given wire grade:

$$UTS = \frac{1}{3} \cdot KHN \cdot 9.81. \tag{6}$$

For grade SR the measured flow resistances 310–320 KHN were within the expected 263–326 KHN range. For grade TE, the measured flow resistance of 400 KHN was within the expected 400–453 KHN range. For grade CR, the measured flow resistances 420 to 500 KHN were higher than the minimum expected 400 KHN, but 8 out of 12 samples exceeded the maximum expected value of 453 KHN.

For most samples of grade CR, the tensile flow resistance in the X direction was significantly higher than the compression flow resistance, as shown in Fig. 8. It seems that the wire aspect ratio, defined as the wire profile width to height, does not affect the centreline flow resistance in the X direction, as shown in Fig. 9.

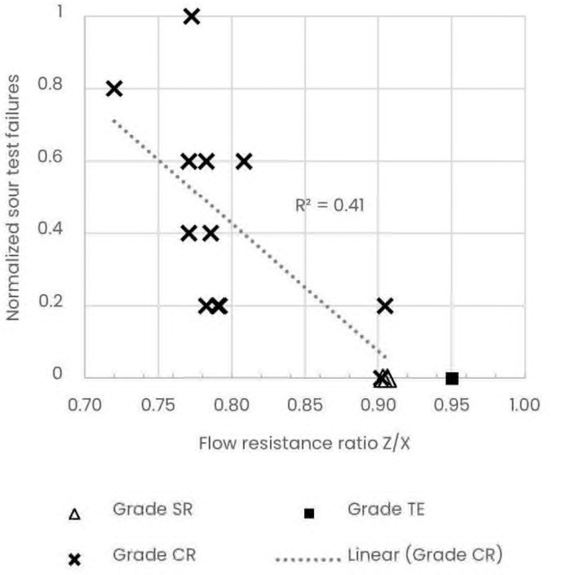

Fig. 12. Plot of the flow resistance ratio Z/X and the normalized sour test result showing an inverse correlation

Rys. 12. Korelacja wyników testów korozyjnych drutu CR ze stosunkiem oporów płynięcia w kierunkach Z i X

The flow resistance in the Y direction was higher than in the Z direction for all samples tested. In two cases the flow resistance in the Y direction was higher than in the X direction. On average for wire grade, CR flow resistance in the Y direction was 422 KHN; an 8% reduction from the average flow resistance in the X direction. The flow resistance in the Y direction appears to increase with the increasing aspect ratio, as shown in Fig. 10.

Statistical tests showed no correlation between the failure rate and the flow resistance in any principal direction for the wire grade CR. An example of the flow resistance in the Z direction plotted against the failure rate is shown in Fig. 11. A linear trend for improved sour resistance of grade CR was observed with the increasing flow resistance ratio Z/X, as shown in Fig. 12.

4. Discussion

Analysis of the measurement errors shows they are acceptable. The other successful use of Wheeler and Ireland technique reported in the literature by Ankamma [10] were applied to the materials with a uniform distribution of chemical composition and cold work. The authors carried out 15 measurements in each orientation using 100 gf load. The resulting measurement error up to 5% is comparable with the one obtained in this work. For the wire material the measurement error can be further reduced by etching samples to reveal the segregation and then placing indents outside of the centreline segregated region.

The measured flow resistance in the X direction corresponds well with the expected tensile strength of wire grades SR and TE. The performed evaluation was insufficient to perform validation of the Wheeler and Ireland technique for rolled wires. Especially after the flow resistance of grade CR turned out to be higher than expected. It may be of future interest to correlate the KHN flow resistance with the results of micro-tensile tests.

The measured flow resistance supports the hypothesis that the Z direction is a "weak" direction and thus an easy path for HIC propagation. The flow resistance in the Z direction does not statistically correlate with the failure rate. However, as a measure of anisotropy, the ratio of the flow resistances Z/X does show an inverse correlation with the failure rate.

The findings of this investigation point toward a hypothesis that Z/X anisotropy is a measure of damage accumulation within the wire centreline. It can be speculated that this damage is of the type that can be reversed by heat treatment. HIC propagation occurs not only by mechanical tearing of material in a weak direction but by more complex interaction which includes the factor of microstructural damage.

There seem to be other independent variables responsible for the wide spread of measured data points. It can be speculated that controlling those factors would allow CR wire grade to limit damage accumulation and decrease the failure rate.

5. Conclusions

The following can be concluded from this investigation:

- The microstructure of all wire grades is deformed axially and width wise, the highest deformation was observed near the centreline.
- The Wheeler and Ireland technique proved useful in evaluating the anisotropy of rolled wires.
- Measured flow resistance in the X direction corresponds well with wire UTS for grades SR and TE.
- Majority of measurement errors came from indents in orientation d. There is a potential to improve the technique described therein by avoiding placing indents in the centreline segregation region.
- All wires are anisotropic, showing the lowest flow resistance in the Z direction. HIC propagates in a plane perpendicular to that direction. Anisotropy was shown to be reduced by heat treatment processes.
- Flow resistance in the Z direction, nor any other, corresponds with the failure rate.
- For the flow resistance ratio, the Z/X correlation with the failure rate was found. It is interpreted that those ratios are a measure of microstructural damage caused by the cold rolling process.

BIBLIOGRAPHY

[1] American Petroleum Institute. May 2014. "Specification 17J Specification for Unbonded Flexible Pipe".

[2] P.F. Timmins. 1996. *Failure Control in Process Operations*. In: *ASM Handbook. Volume 19: Fatigue and Fracture*. Materials Park, Ohio: ASM International.

[3] M.C.E. Bandeira, R.M. Moreira, B. de Barros, R.C. Ribeiro, P. Silva, O.R. Mattos, F.P. dos Santos. 2019. "The Effect of H_2S Consumption on SSC Susceptibility of High Strength Wire Grades for Flexible Pipes". Corrosion 2019: NACE-2019-13483. Nashville, Tennessee.

[4] N. Desamais, C. Taravel-Condat. 2009. "On the Beneficial Influence of a Very Low Supply of H_2S on the Hydrogen Embrittlement Resistance of Carbon Steel Wires in Flexible Pipe Annulus". Offshore Technology Conference: OTC-19950-MS. Houston, Texas. DOI: 10.4043/19950-MS.

[5] A. Dugstad, S. Palencsár, L. Børvik, T. Berntsen. 2020. "Corrosion of Steel Armor Wires in Flexible Pipes – Effect of Small Amount of H_2S". Corrosion 2020: NACE-2020-14876.

[6] D. Lee, W.A. Backofen. 1966. "An Experimental Determination of the Yield Locus for Titanium and Titanium-Alloy Sheet (Yield Locus of Titanium and Titanium-Alloy Sheet under Combined-Stress Loading)". *Transactions of the Metallurgical Society of AIME* 236(7): 1077–1084.

[7] R.G. Wheeler, D.R. Ireland. 1966. "Multiaxial Plastic Flow of Zircaloy-2 Determined from Hardness Data". *Electrochemical Technology* 4: 313–317.

[8] D.R. Ireland. 1967. *Practical Technique for Obtaining and Using Plastic Anisotropy Information*. Technical report from 96th Annual Meeting of the American Institute of Mining, Metallurgical, and Petroleum Engineers. Los Angeles, California.

[9] S. Foissey, Ch. Bertout, X. Perroud. 2017. *Process for Manufacturing a Profiled Steel Wire*. Patent No. US 9,617,625 B2.

[10] K. Ankamma, D.V.V. Satyanarayana, G. Chandramohan Reddy, M. Komaraiah, N. Eswara Prasad. 2011. "In-Plane Anisotropy in Tensile Deformation and Its Influence on the Drawability of Nimonic c-263 Alloy Sheets". *Sadhana* 36: 223–249. DOI: 10.1007/s12046-011-0016-6.